International Journal of Modern Physics E

Predictions for p+Pb Collisions at $\sqrt{s_{NN}} = 5$ TeV

JAVIER L. ALBACETE

IPNO, Université Paris-Sud 11, CNRS/IN2P3, 91406 Orsay, France

NESTOR ARMESTO

Departamento de Física de Partículas and IGFAE, Universidade de Santiago de Compostela, 15706 Santiago de Compostela, Galicia, Spain

RUDOLF BAIER

Fakultät für Physik, Universität Bielefeld, D-33501, Bielefeld, Germany

GERGELY G. BARNAFÖLDI

Institute for Particle and Nuclear Physics, Wigner Research Centre for Physics, Hungarian Academy of Sciences, P.O.Box 49, Budapest, 1525, Hungary

JEAN BARRETTE

McGill University, Montreal, H3A 2T8, Canada

SOMNATH DE

Variable Energy Cyclotron Centre, 1/AF, Bidhan Nagar, Kolkata, 700064, India

WEI-TIAN DENG

Theory Center, IPNS, KEK, 1-1 Oho, Tsukuba, Ibaraki 305-0801, Japan

ADRIAN DUMITRU

Department of Natural Sciences, Baruch College, CUNY, 17 Lexington Avenue, New York, NY 10010, USA

RIKEN BNL Research Center, Brookhaven National Laboratory, Upton, NY 11973, USA

KEVIN DUSLING

Physics Department, North Carolina State University, Raleigh, NC 2 7695, USA

KARI J. ESKOLA

Department of Physics, P.O. Box 35, FI-40014 University of Jyväskylä, Finland

Helsinki Institute of Physics, P.O. Box 64, FIN-00014 University of Helsinki, Finland

RAINER FRIES

Cyclotron Institute and Department of Physics and Astronomy, Texas A&M University, College

Station, TX 77843, USA

HIROTSUGU FUJII

Institute of Physics, University of Tokyo, Komaba, Tokyo 153-8902, Japan

FRANCOIS GELIS

Institut de Physique Théorique, CEA, 91191 Gif-sur-Yvette Cedex, France

MIKLOS GYULASSY

Department of Physics, Columbia University, New York, NY 10027, USA

WIGNER RCP, Institute for Particle and Nuclear Physics P.O.Box 49, Budapest, 1525, Hungary

YUNCUN HE

Key Laboratory of Quark & Lepton Physics (MOE) and Institute of Particle Physics, Central China Normal University, Wuhan 430079, China

ILKKA HELENIUS

Department of Physics, P.O. Box 35, FI-40014 University of Jyväskylä, Finland

Helsinki Institute of Physics, P.O. Box 64, FIN-00014 University of Helsinki, Finland

ZHONG-BO KANG

Theoretical Division, MS B283, Los Alamos National Laboratory, Los Alamos, NM 87545, USA

BORIS Z. KOPELIOVICH

Departamento de Física, Universidad Técnica Federico Santa María, Avda. España 1680, Casilla 110-V, Valparaíso, Chile

KRZYSZTOF KUTAK

Instytut Fizyki Jadrowej im. Henryka Niewodniczańskiego, Radzikowskiego 152, 31-342 Kraków, Poland

PETER LEVAI

Institute for Particle and Nuclear Physics, Wigner Research Centre for Physics, Hungarian Academy of Sciences, P.O.Box 49, Budapest, 1525, Hungary

ZI-WEI LIN

C-209 Howell Science Complex, Department of Physics, East Carolina University, Greenville,

NC 27858, USA

ALFRED H. MUELLER

Department of Physics, Columbia University, New York, NY 10027, USA

YASUSHI NARA

Akita International University, Yuwa, Akita-city 010-1292, Japan

JAN NEMCHIK

Czech Technical University in Prague, FNSPE, Břehová 7, 11519 Prague, Czech Republic

GÁBOR PAPP

Eötvös Loránd University, Pázmány Péter sétány 1/A, H-1117, Budapest, Hungary

MIHAI PETROVICI

National Institute for Physics and Nuclear Engineering, Horia Hulubei, R-077125, Bucharest, Romania

JIAN-WEI QIU

Physics Department, Brookhaven National Laboratory, Upton, NY 11973, USA

C.N. Yang Institute for Theoretical Physics, Stony Brook University, Stony Brook, NY 11794, USA

AMIR H. REZAEIAN

Departamento de Física, Universidad Técnica Federico Santa María, Avda. España 1680, Casilla 110-V, Valparaíso, Chile

PENG RU

School of Physics & Optoelectronic Technology, Dalian University of Technology, Dalian, 116024 China

Institute of Particle Physics, Central China Normal University, Wuhan, 430079 China

DOMINIQUE SCHIFF

LPT, Université Paris-Sud, Bâtiment 210, F-91405 Orsay, France

SEBASTIAN SAPETA

Institute for Particle Physics Phenomenology, Durham University, South Rd, Durham DH1

3LE, UK

VASILE TOPOR POP

McGill University, Montreal, H3A 2T8, Canada

PRITHWISH TRIBEDY

Variable Energy Cyclotron Centre, 1/AF Bidhan Nagar, Kolkata-70006 4, India

RAJU VENUGOPALAN

Physics Department, Brookhaven National Laboratory, Upton, NY 11973, USA

IVAN VITEV

Theoretical Division, MS B283, Los Alamos National Laboratory, Los Alamos, NM 87545, USA

RAMONA VOGT

Physics Division, Lawrence Livermore National Laboratory, Livermore, CA 94551, USA

Physics Department, University of California at Davis, Davis, CA 95616, USA
vogt@physics.ucdavis.edu

ENKE WANG

Key Laboratory of Quark & Lepton Physics (MOE) and Institute of Particle Physics, Central China Normal University, Wuhan 430079, China

XIN-NIAN WANG

Key Laboratory of Quark and Lepton Physics (MOE) and Institute of Particle Physics, Central China Normal University, Wuhan 430079, China

Nuclear Science Division, MS 70R0319, Lawrence Berkeley National Laboratory, Berkeley, CA 94720, USA

HONGXI XING

Institute of Particle Physics, Central China Normal University, Wuhan 430079, China

RONG XU

Key Laboratory of Quark and Lepton Physics (MOE) and Institute of Particle Physics, Central China Normal University, Wuhan 430079, China

BEN-WEI ZHANG

Key Laboratory of Quark & Lepton Physics (MOE) and Institute of Particle Physics, Central China Normal University, Wuhan 430079, China

Nuclear Science Division, MS 70R0319, Lawrence Berkeley National Laboratory, Berkeley, CA 94720, USA

WEI-NING ZHANG

School of Physics & Optoelectronic Technology, Dalian University of Technology, Dalian,

116024 China

Physics Department, Harbin Institute of Technology, Harbin 150006, China

Predictions for charged hadron, identified light hadron, quarkonium, photon, jet and gauge bosons in p+Pb collisions at $\sqrt{s_{NN}} = 5$ TeV are compiled and compared. When test run data are available, they are compared to the model predictions.

Keywords: perturbative QCD, hard probes of heavy-ion collisions

12.38.Bx, 25.75.Bh, 25.75.Cj, 13.87.-a

1. Introduction

Here predictions for the upcoming p+Pb LHC run at $\sqrt{s_{NN}} = 5$ TeV compiled by members and friends of the JET Collaboration[1] are presented. The test run data published by the ALICE Collaboration[2,3] are compared to model calculations available before the test run. Most calculations are for midrapidity and minimum bias collisions. Other results at different rapidities and centralities are presented when available.

The predictions presented here, as well as the corresponding discussion, were made assuming that the proton circulated toward positive rapidity and the nucleus toward negative rapidity, p+Pb collisions, similar to fixed-target configurations. In the fixed-target configuration, the low x nuclear parton distributions are probed at positive rapidity. Throughout this paper, many of the results shown have been adjusted to the Pb+p convention of the ALICE data, as described in Ref.,[2] with the nuclear parton density probed at high x at forward (positive) rapidity and low x at backward (negative) rapidity. The cases where the results still appear with the assumption that the proton circulates in the direction of positive rapidity are explicitly noted.

This paper is organized in the following fashion. Section 2 describes the models that specifically address charged particle production. These include saturation approaches, event generators, and perturbative QCD-based calculations. Section 3 compares results obtained from models described in Sec. 2 with each other and with the available data. The next several sections present predictions for specific observables including identified light hadrons (Sec. 4), quarkonium (Sec. 5), direct photons (Sec. 6), jets (Sec. 7), and gauge bosons (Sec. 8).

2. Model descriptions

In this section, the models used to obtain the results for charged particle distributions, $dN_{\rm ch}/d\eta$, $dN_{\rm ch}/dp_T$ and the nuclear suppression factor $R_{p\rm Pb}$ as a function of p_T and η. The first calculations described Sec. 2.1 are saturation or Color Glass Condensate (CGC) based. The next set of calculations are event-generator based with results from `HIJING` in Sec. 2.3, `HIJINGB`$\overline{\texttt{B}}$`2.0` in Sec. 2.4, and `AMPT` in Sec. 2.5.

Finally, calculations based on collinear factorization in perturbative QCD are described in Secs. 2.6 and 2.7.

In the following Section, Sec. 3, the predictions will be compared to the ALICE Pb+p test run data[2,3] in September 2012.

2.1. *Inclusive hadron production in the rcBK-CGC approach (A. Rezaeian)*

In the Color Glass Condensate (CGC) approach, gluon jet production in $p + A$ collisions can be described by k_T-factorization,[4]

$$\frac{d\sigma}{dy\, d^2p_T} = \frac{2\alpha_s}{C_F}\frac{1}{p_T^2}\int d^2\vec{k}_T \phi_p^G\left(x_1;\vec{k}_T\right)\phi_A^G\left(x_2;\vec{p}_T-\vec{k}_T\right), \tag{1}$$

where $C_F = (N_c^2-1)/2N_c$, N_c is the number of colors, $x_{1,2} = (p_T/\sqrt{s})e^{\pm y}$, p_T and y are the transverse momentum and rapidity of the produced gluon jet, and $\sqrt{s}$ is the nucleon-nucleon center-of-mass energy. The unintegrated gluon density, $\phi_A^G(x_i;\vec{k}_T)$, denotes the probability to find a gluon that carries fractional energy x_i and transverse momentum k_T in the projectile (or target) A. The unintegrated gluon density is related to the color dipole forward scattering amplitude,

$$\phi_A^G\left(x_i;\vec{k}_T\right) = \frac{1}{\alpha_s}\frac{C_F}{(2\pi)^3}\int d^2\vec{b}_T\, d^2\vec{r}_T\, e^{i\vec{k}_T\cdot\vec{r}_T}\,\nabla_T^2\mathcal{N}_A\left(x_i;r_T;b_T\right), \tag{2}$$

with

$$\mathcal{N}_A\left(x_i;r_T;b_T\right) = 2\mathcal{N}_F\left(x_i;r_T;b_T\right) - \mathcal{N}_F^2\left(x_i;r_T;b_T\right), \tag{3}$$

where r_T is the transverse size of the dipole and b_T is the impact parameter of the collision. The subscript T stands for the transverse component. The dipole scattering amplitude $\mathcal{N}_F$ satisfies the nonlinear small-x JIMWLK evolution equations,[5–8] see below.

In the k_T-factorized approach, partons in both the projectile and target are assumed to be at very small x so that the CGC formalism and small-x resummation is applicable to both the projectile and the target, assuming the projectile proton moves in the direction of forward rapidity. This approach is valid away from the projectile fragmentation region. However, to treat the projectile fragmentation region in the forward region, an alternative approach developed in Refs.,[9,10] the so-called hybrid approach, is better suited. In this approach, the projectile is treated perturbatively within the standard collinear factorization scheme using the standard DGLAP picture while the target is treated employing CGC methods. The cross section for single inclusive hadron production at leading twist in asymmetric

collisions such as $p + A$ in the CGC approach is given by,[9,10]

$$\frac{dN^{pA\to hX}}{d\eta d^2p_T} = \frac{K}{(2\pi)^2}\Bigg[\int_{x_F}^1 \frac{dz}{z^2}\Big[x_1 f_g(x_1,\mu_F^2)N_A(x_2,\frac{p_T}{z})D_{h/g}(z,\mu_{\rm Fr}) + \Sigma_q x_1 f_q(x_1,\mu_F^2)N_F(x_2,\frac{p_T}{z})D_{h/q}(z,\mu_{\rm Fr})\Big] + \frac{\alpha_s^{\rm in}}{2\pi^2}\int_{x_F}^1\frac{dz}{z^2}\frac{z^4}{p_T^4}\int_{k_T^2<\mu_F^2} d^2k_T k_T^2 N_F(k_T,x_2)\int_{x_1}^1\frac{d\xi}{\xi} \times \Sigma_{i,j=q,\bar{q},g} w_{i/j}(\xi)P_{i/j}(\xi)x_1 f_j(\frac{x_1}{\xi},\mu_F)D_{h/i}(z,\mu_{\rm Fr})\Bigg]\,. \quad (4)$$

A K-factor has been introduced to effectively incorporate higher-order corrections. The parton distribution function of the proton, $f_j(x,\mu_F^2)$, depends on the light-cone momentum fractions x and the hard factorization scale μ_F. The function $D_{h/i}(z,\mu_{\rm Fr})$ is the fragmentation function (FF) of parton i to become final-state hadron h carrying a fraction z of the parent parton momentum at fragmentation scale $\mu_{\rm Fr}$. The inelastic weight functions, $w_{i/j}$, and the DGLAP splitting functions, $P_{i/j}$, are given in Ref.[10] The longitudinal momentum fractions x_1 and x_2 are

$$x_F \approx \frac{p_T}{\sqrt{s}}e^{\eta}; \quad x_1 = \frac{x_F}{z}; \quad x_2 = x_1 e^{-2\eta}. \quad (5)$$

The strong coupling multiplying the inelastic term in Eq. (4), is denoted $\alpha_s^{\rm in}$. The superscript "in" is employed to differentiate it from the running value of α_s in the rcBK equation. In the hybrid formulation, the strong coupling in the dilute regime of the projectile can differ from that in the rcBK description of the dense target (or dipole scattering amplitude). The scale at which $\alpha_s^{\rm in}$ should be evaluated cannot be determined in the current approximation, a full NNLO calculation is required. The effects of different choices of $\alpha_s^{\rm in}$ will be considered later.

In Eq. (4), the factorization scale μ_F is assumed to be the same in the fragmentation functions ($\mu_{\rm Fr} = \mu_F$) and the parton densities. In order to investigate the uncertainties associated with choice of μ_F, several values of μ_F are considered: $\mu_F = 2p_T$; p_T; and $p_T/2$.

In Eq. (4), the amplitude N_F (N_A) is the two-dimensional Fourier transform of the imaginary part of the forward (proton direction) dipole-target scattering amplitude, $\mathcal{N}_{A(F)}$, in the fundamental (F) or adjoint (A) representations,

$$N_{A(F)}(x,k_T) = \int d^2\vec{r}e^{-i\vec{k}_T.\vec{r}}\left[1-\mathcal{N}_{A(F)}(r,Y=\ln\left(\frac{x_0}{x}\right))\right], \quad (6)$$

where $r = |\vec{r}|$ is the dipole transverse size. The dipole scattering amplitude $\mathcal{N}_{A(F)}$ incorporates small-x dynamics and can be calculated using the JIMWLK evolution equation.[5–8] In the large N_c limit, the coupled JIMWLK equations are simplified to the Balitsky-Kovchegov (BK) equation,[11–14] a closed-form equation for the rapidity evolution of the dipole amplitude. While a numerical solution of the full next-to-leading logarithmic expressions is not yet available, the running coupling corrections

to the leading log kernel, the so-called running-coupling BK (rcBK) equation has been very successful in phenomenological applications.[15] The rcBK equation has the following simple form:[11–14,16]

$$\frac{\partial \mathcal{N}_{A(F)}(r,x)}{\partial \ln(x_0/x)} = \int d^2\vec{r}_1 \; K^{\rm run}(\vec{r},\vec{r}_1,\vec{r}_2) \left[\mathcal{N}_{A(F)}(r_1,x) + \mathcal{N}_{A(F)}(r_2,x) - \mathcal{N}_{A(F)}(r,x) - \mathcal{N}_{A(F)}(r_1,x)\,\mathcal{N}_{A(F)}(r_2,x)\right], \tag{7}$$

where $\vec{r}_2 \equiv \vec{r} - \vec{r}_1$. The rcBK equation only describes the rapidity/energy evolution of the dipole, the initial profile and parameters of the dipole still need to be modeled and constrained by experimental data. The initial condition for the evolution generally takes a form motivated by the McLerran-Venugopalan model,[17–19]

$$\mathcal{N}(r, Y=0) = 1 - \exp\left[-\frac{\left(r^2\, Q_{0s}^2\right)^\gamma}{4}\, \ln\left(\frac{1}{\Lambda\, r} + e\right)\right], \tag{8}$$

where the onset of small-x evolution is assumed to be at $x_0 = 0.01$, and the infrared scale is $\Lambda = 0.241$ GeV.[15] The only free parameters are γ and the initial saturation scale Q_{0s}, with $s = p$ and A for proton and nuclear targets, respectively. Unfortunately, the current global set of small-x data are very limited and thus cannot uniquely fix the initial dipole parameters.[15] This problem is more severe for determining the dipole scattering amplitude on nuclear targets, leading to rather large unavoidable theoretical uncertainties on CGC predictions for $p+A$ collisions at the LHC. In Ref.,[20] a simple scheme to test the CGC dynamics at the LHC was proposed. This scheme will be used to calculate the results shown later on.

2.2. *IP-Sat (P. Tribedy and R. Venugopalan)*

The impact parameter dependent dipole saturation model (IP-Sat)[21] is a refinement of the Golec-Biernat–Wusthoff dipole model[22,23] to give the right perturbative limit when the dipole radius $r_T \to 0$.[24] It is equivalent to the expression derived in the classical effective theory of the CGC, to leading logarithmic accuracy.[25,26] The proton dipole cross section in this model is expressed as

$$\frac{d\sigma^p_{\rm dip}}{d^2b_T}(r_T,x,b_T) = 2\left[1 - \exp\left(-\frac{\pi^2}{2N_c} r_T^2 \alpha_s(\mu^2) x g(x,\mu^2) T_p(b_T)\right)\right]. \tag{9}$$

Here the scale μ^2 is related to dipole radius r_T as

$$\mu^2 = \frac{4}{r_T^2} + \mu_0^2\,, \tag{10}$$

where the leading order expression for the running coupling is

$$\alpha_s(\mu^2) = \frac{12\pi}{(33-2n_f)\log(\mu^2/\Lambda^2_{\rm QCD})} \tag{11}$$

with $n_f = 3$ and $\Lambda_{\rm QCD} = 0.2$ GeV. The model includes saturation as eikonalized power corrections to the DGLAP leading-twist expression and may be valid in the

Table 1. Parameters of the IP-Sat model obtained from fits to HERA data.[32]

B_G (GeV^{-2})	μ_0 (GeV^2)	A_g	λ_g
4.0	1.17	2.55	0.020

regime where logs in Q^2 dominate logs in x. For each value of the dipole radius, the gluon density $xg(x,\mu^2)$ is evolved from μ_0^2 to μ^2 using the LO DGLAP evolution equation without quarks,

$$\frac{\partial xg(x,\mu^2)}{\partial \log \mu^2} = \frac{\alpha_s(\mu^2)}{2\pi} \int_x^1 dz P_{gg}(z) \frac{x}{z} g\left(\frac{x}{z}, \mu^2\right) \ . \tag{12}$$

Here the gluon splitting function is

$$P_{gg}(z) = 6\left[\frac{z}{(1-z)+} + \frac{1-z}{z} + z(1-z)\right] + \left(\frac{11}{2} - \frac{n_f}{3}\right)\delta(1-z) \ . \tag{13}$$

The initial gluon density at the scale μ_0^2 is taken to be of the form

$$xg(x,\mu_0^2) = A_g x^{-\lambda_g}(1-x)^{5.6} \ . \tag{14}$$

An important feature of the IP-Sat model is the b-dependence of the dipole cross section, introduced through the gluon density profile function $T_p(b_T)$. This profile function, normalized to unity, is chosen to have the Gaussian form

$$T_p(b_T) = \frac{1}{2\pi B_G} \exp\left(\frac{-b_T^2}{2B_G}\right) \ , \tag{15}$$

where B_G is a parameter fit to the HERA diffractive data. It corresponds to $\langle b^2 \rangle = 2B_G$, the average squared *gluonic* radius of the proton.

The IP-Sat model parameters are obtained from optimal fits to HERA data.[32] The parameters used in this work are listed in Table 2.2. The parameters of the initial gluon distribution are determined from fits to the HERA F_2 data[28,29] with $\chi^2 \sim 1$. The value of B_G is determined primarily from the J/ψ t-distributions measured by ZEUS[30] and H1.[31] With these parameters, excellent agreement with the HERA exclusive vector meson and DVCS data is obtained. For a detailed comparison of this model to the HERA data, see Ref.[32] A more recent fit to the combined ZEUS and H1 data has been performed in Ref.[33]

The IP-Sat model successfully describes the bulk features of the $p+p$ and $A+A$ data over a wide range of center-of-mass energies from RHIC to LHC as well as the features of the RHIC d+Au data.[34,35] It also provides the basis for the IP-Glasma model[36,37] of initial conditions in heavy-ion collisions.

In the IP-Sat model, the dipole-nucleus cross section in a large nucleus can be approximated as

$$\frac{d\sigma^A_{\rm dip}}{d^2 s_T} \approx 2\left[1 - \exp\left\{-\frac{AT_A(s_T)}{2}\sigma^p_{\rm dip}(r_T, x)\right\}\right] \tag{16}$$

where $AT_A(s_T)$ is the transverse density of nucleons inside a nucleus and $\sigma^p_{\rm dip}(r_T, x)$ is obtained by integrating the dipole-proton cross section in Eq. (9) over the impact parameter distribution in the proton. This form of the dipole-nucleus cross section was previously shown to give reasonable fits to the limited available inclusive fixed-target $e + A$ data.[38]

In $p + A$ collisions, the LO inclusive gluon distribution can be expressed as[39]

$$\frac{dN_g^{pA}(b_T)}{dy\ d^2p_T} = \frac{4\alpha_s}{\pi C_F}\frac{1}{p_T^2}\int\frac{d^2k_T}{(2\pi)^5}\int d^2s_T\frac{d\phi_p(x_1,k_T|s_T)}{d^2s_T}\frac{d\phi_A(x_2,p_T-k_T|s_T-b_T)}{d^2s_T}\ . \quad (17)$$

This equation is a generalization of the well known k_T-factorized expression for inclusive gluon production[40] to include the impact parameter dependence of the unintegrated gluon distributions. Here $C_F = (N_c^2 - 1)/2N_c$ is the Casimir for the fundamental representation. Using a relation between quark and gluon dipole amplitudes strictly valid in the large N_c limit, the unintegrated gluon distribution in protons and nuclei can be expressed in terms of the corresponding dipole cross section measured in DIS as[41]

$$\frac{d\phi^{p,A}(x,k_T|s_T)}{d^2s_T} = \frac{k_T^2N_c}{4\alpha_s}\int_0^\infty d^2r_T e^{i\vec{k_T}\cdot\vec{r_T}}\left[1-\frac{1}{2}\frac{d\sigma^{p,A}_{\rm dip}}{d^2s_T}(r_T,x,s_T)\right]^2\ . \quad (18)$$

2.3. HIJING2.1 *(R. Xu, W.-T. Deng and X.-N. Wang)*

The HIJING[43,44] Monte Carlo is based on a two-component model of hadron production in high-energy $p + p$, $p + A$, and $A + A$ collisions. The soft and hard components are separated by a cutoff momentum p_0 in the transverse momentum exchange. Hard parton scatterings with $p_T > p_0$ are assumed to be described by perturbative QCD (pQCD), while soft interactions are approximated by string excitations with an effective cross section $\sigma_{\rm soft}$. In $p+A$ collisions, the single jet inclusive cross section is proportional to the nuclear parton densities $f_{a/A}(x_2, p_T^2, b)$,

$$\frac{d\sigma^{\rm jet}_{pA}}{dy_1 d^2p_T} = K\int dy_2\, d^2b\, T_A(b)\sum_{a,b,c}x_1 f_{a/p}(x_1,p_T^2)x_2 f_{a/A}(x_2,p_T^2,b)\frac{d\sigma_{ab\to cd}}{dt}\ .$$

Here, $x_{1,2} = p_T(e^{\pm y_1} + e^{\pm y_2})/\sqrt{s}$ are the fractional momenta of the initial partons while $y_{1,2}$ are the rapidities of the final parton jets. Higher order corrections are absorbed into the K factor. The nuclear thickness function is normalized to A, $\int d^2b\, T_A(b) = A$.

There are several cold nuclear matter effects that are considered in HIJING. The first is the shadowing effect. HIJING2.0[45,46] employs a factorized form of the parton densities in nuclei,[47]

$$f_{a/A}(x,\mu_F^2,b) = S_{a/A}(x,\mu_F^2,b)f_{a/A}(x,\mu_F^2) \quad (19)$$

where $S_{a/A}(x,\mu_F^2,b)$ is the impact-parameter dependent nuclear modification factor. However, the shadowing employed in HIJING2.0 does not include any μ_F^2 de-

pendence as in e.g. Ref.[48] Therefore, shadowing effects in HIJING should only be valid at low p_T and disappear at larger p_T.

The second cold matter effect included is the Cronin effect,[49] the enhancement of intermediate p_T hadron spectra in $p + A$ collisions. Multiple scattering inside a nucleus can lead to the transverse momentum (k_T) broadening of both the initial- and final-state partons. A k_T-kick is imparted to both the initial and final-state hard scattered partons in each binary nucleon-nucleon scattering. The k_T-kick of each scattering follows a Gaussian distribution. Fits to the fixed-target $p + A$ data lead to an energy dependence of the Gaussian width,

$$\langle k_T^2 \rangle = [0.14 \log(\sqrt{s}/\mathrm{GeV}) - 0.43]\,\mathrm{GeV}^2/c^2 \ . \tag{20}$$

This k_T-kick influences the final-state hadron rapidity distribution. After tuning the gluon shadowing parameter s_g[47] in HIJING2.1, the charged particle rapidity distribution, $dN_{\mathrm{ch}}/d\eta$, in d+Au collisions at $\sqrt{s_{NN}} = 200$ GeV can be described. The prediction for LHC energies can be obtained by extrapolation.[50]

In the default HIJING setting, $p + A$ and $A + A$ collision are decomposed into independent and sequential nucleon-nucleon collisions. Within each nucleon-nucleon collision, hard collisions are simulated first, followed by soft collisions. However, since the time scale for hard scattering is much shorter than soft interactions, such a sequence of hard and soft interactions within each binary collision might not be physical. In a revised scheme denoted by DHC (decoherent hard scattering), all the hard interactions in a $p + A$ event are simulated first. They are subsequently followed by the soft interactions. As a consequence, the energy available in each hard scattering is no longer restricted by soft interactions.

An additional cold matter effect arises from valence quark number conservation in the proton. In $p+A$ collisions, the projectile proton will suffer multiple scatterings within the target nucleus. For each binary nucleon-nucleon collision, there is a finite probability for independent hard parton scattering involving initial partons from the projectile and target nucleons. Flavor conservation limits the availability of valence quarks from the projectile for each of these hard interactions. This effect can change the relative flavor composition of produced partons per average binary nucleon-nucleon collision. Since the gluon fragmentation functions are softer than those of the quarks, the increased fraction of produced gluon jets in $p+A$ collisions can lead to suppression of the final-state high-p_T hadron spectra.

Finally, jet fragmentation can also modify the final hadron spectra in $p + A$ collisions. In the default HIJING setup, jet shower partons from initial- and final-state radiation are ordered in rapidity. Gluons are connected to the valence quark and diquark of the projectile or target nucleons as kinks to form systems of strings. These strings fragment into final-state hadrons using the Lund string fragmentation model.[51] In $p + A$ collisions, the projectile can undergo multiple scatterings since its string systems have many more gluons attached to them than in $p+p$ collisions. Hadrons produced by the fragmentation of such string systems are softer than those resulting from independent fragmentation of individual gluons.

2.4. HIJINGBB̄2.0 *(G. G. Barnaföldi, J. Barette, M. Gyulassy, P. Levai, M. Petrovici, and V. Topor Pop)*

Monte Carlo models such as HIJING1.0,[43,52] HIJING2.0[45,46] and HIJINGBB̄2.0[53–56] have been developed to study hadron production in $p+p$, $p+A$ and $A+A$ collisions. They are essentially two-component models which describe the production of hard parton jets and the soft interaction between nucleon remnants. Hard jet production is calculated employing collinearly-factorized multiple minijet production within pQCD. A transverse momentum cut-off, p_0, on the final-state jet production is introduced so that for $p_T < p_0$ the interaction is nonperturbative and is characterized by a finite soft parton cross section $\sigma_{\rm soft}$. The jet cross sections depend on the parton distribution functions parameterized from global fits to data.[45,46]

Nucleon remnants interact via soft gluon exchanges described by the string models[57–59] and constrained from lower energy $e^+ + e^-$, $e^\pm + p$, and $p+p$ data. The hard jet pairs and the two excited nucleon remnants are connected by independent strings which fragment to resonances that decay to the final-state hadrons. Longitudinal beam-jet string fragmentation depends strongly on the values of the string tensions that control the quark-antiquark ($q\bar{q}$) and diquark-antidiquark ($qq\overline{qq}$) creation rates and strangeness suppression factors (γ_s).

In HIJING1.0 and HIJING2.0, a constant (vacuum value) for the effective value of string tension, $\kappa_0 = 1.0$ GeV/fm, is used. At high initial energy density, the novel nuclear physics is due to the possibility of overlapping multiple longitudinal flux tubes leading to strong longitudinal color field (SCF) effects. These effects are modeled in HIJINGBB̄2.0 by varying the effective string tension. SCFs also modify the fragmentation processes, resulting in an increase of (strange)baryons which play an important role in the description of the baryon to meson anomaly. In order to describe the $p+p$ and central Pb+Pb data at the LHC, we have shown that the energy and mass dependence of the mean value of the string tension should be taken into account.[53,54] Moreover, to better describe the baryon to meson anomaly seen in the data, a specific implementation of JJ̄ loops, has to be introduced. For a detailed discussion, see Refs.[53,54,56] Similar results can be obtained by including extra diquark-antidiquark production channels from the strong coherent fields formed in heavy-ion collisions.[60]

All HIJING-type models implement nuclear effects such as modification of the parton distribution functions, *shadowing*, and *jet quenching* via medium-induced parton splitting. (Collisional energy loss is neglected.[43,52]) In HIJING1.0 and HIJINGBB̄2.0, the Duke-Owen (DO) parameterizations of the proton parton densities[61] is used to calculate the jet production cross section with $p_T > p_0$. In both codes, a constant cutoff, $p_0 = 2$ GeV/c, and a soft parton cross section, $\sigma_{\rm soft} = 54$ mb, fit the experimental $p+p$ data. However, for $A+A$ collisions in HIJINGBB̄2.0, an energy and mass dependence of the cut-off parameter, $p_0(s,A) = 0.416\sqrt{(}s)^{0.191}A^{0.128}$ GeV/c, was introduced[53,54,56] at RHIC and LHC energies in order not to violate the geometrical limit for minijets production per

unit transverse area. The $p + p$ cutoff was kept constant at $p_0 = 2$ GeV/c. In HIJING2.0,[45,46] a subsequent version of HIJING1.0[43,52] the GRV parameterization of the proton parton densities[62] is implemented. The GRV small x gluon density is much higher than that of the DO parameterization. Here also an energy-dependent cutoff $p_0(s)$ and soft cross section $\sigma_{\rm soft}(s)$ are also assumed in order to better describe the Pb+Pb data at the LHC. The cutoff used in HIJINGB$\overline{\rm B}$2.0 varies from $p_0 = 1.5$ GeV/c at the CERN SPS, $\sqrt{s} = 20$ GeV, to 4.2 GeV/c at $\sqrt{s} = 5.5$ TeV while that in HIJING2.0, with a more complex energy dependence, varies from 1.7 to 3.5 GeV/c in the same energy range.

One of the main uncertainties in the calculation of the charged particle multiplicity density in Pb+Pb collisions is the nuclear modification of parton distribution functions, especially gluon distributions at small x. In HIJING-type models, the parton distributions per nucleon in a nucleus, $f_{a/A}(x, \mu_F^2)$, are factorizable into parton distributions in a nucleon, $f_{a/N}$, and the shadowing function for parton a, $S_{a/A}$, as in Eq. (19). The shadowing parameterization in HIJING1.0[43,52] is employed,

$$\begin{aligned} S_{a/A}(x) &\equiv \frac{f_{a/A}(x)}{A f_{a/N}(x)} \\ &= 1 + 1.19 \log^{1/6} A \left[x^3 - 1.2x^2 + 0.21x\right] \\ &\quad - s_a (A^{1/3} - 1) \left[1 - \frac{10.8}{\log(A+1)} \sqrt{x}\right] e^{-x^2/0.01} \ , \end{aligned} \tag{21}$$

assuming the same dependence for quarks and gluons. The μ_F^2 evolution of $S_{a/A}(x, \mu_F)$ is neglected. The parameter, s_a, which determines the shadowing for $x < 0.1$, the region with the strongest nuclear dependence, is $s_a = 0.1$. For $x > 0.1$, the A dependence is rather weak. The parameterization in Eq. (21) agrees with the x dependence of the quark structure function at small and medium x.[43,52] Because the first part of Eq. (21) has a weak A dependence, impact parameter dependence is only included on part proportional to s_a. The impact parameter dependence is given as

$$s_a(b) = s_a \frac{5}{3} \left(1 - \frac{b^2}{R_A^2}\right) \ , \tag{22}$$

where R_A is the radius of the nucleus and $s_a = s_q = s_g = 0.1$.

The LHC Pb+Pb data at $\sqrt{s_{NN}} = 2.76$ TeV[53,54] indicate that impact-parameter dependent shadowing is required to understand the centrality dependence of the charged particle multiplicity density at midrapidity. These data place an indirect and model-dependent constraint on quark and gluon shadowing. Therefore, it is important to directly study quark and gluon shadowing in $p + A$ collisions at the LHC.

In contrast, in HIJING2.0,[45,46] the factor $(A^{1/3} - 1)$ is raised to the power 0.6 and a stronger impact-parameter dependence, different for quarks and gluons, $s_q = 0.1$ and $s_g = 0.22 - 0.23$ respectively, is used to fit the LHC data. This stronger gluon shadowing requires jet quenching to be neglected.[45,46]

All HIJING-type models assume scale-independent shadowing (independent of Q^2). This approximation could break down at sufficiently large scales due to the dominance of gluon emission in the DGLAP[63] evolution equation. At $Q = 2.0$ and 4.3 GeV/c, typical scales for minijet production at RHIC and LHC respectively, low x gluon shadowing varies by $\approx 13\%$ in the EPS09 LO parameterization.[48]

2.5. AMPT *(Z. Lin)*

The multiphase transport model AMPT[64] was also used to calculate the yields and p_T spectra of particles produced in $p+p$ and p+Pb collisions, as well as the nuclear modification factors $R_{\rm pPb}$ in p+Pb collisions. The flow coefficients have also been calculated. Both the default, AMPT − def and the string melting, AMPT − SM, versions of AMPT[65] have been employed.

In the default version of AMPT, AMPT − def, only minijet partons rescatter in the parton stage. After that, Lund string fragmentation is used for hadronization with the hadron cascade setting in at relatively high energy density. The cutoff time for the hadron cascade in these simulations is 30 fm/c (NTMAX = 150[65]). On the other hand, the string-melting version of AMPT, AMPT − SM, converts the usual initial-state hadronic strings to partonic matter when the energy density in the collision overlap volume is expected to be higher than that of the QCD phase transition. AMPT − SM also uses a simple quark coalescence model to describe bulk hadronization of the resultant partonic matter. Thus, secondary interactions are typically dominated by hadron interactions in AMPT − def while dominated by parton interactions in AMPT − SM.

Using the default HIJING parameters for the Lund symmetric splitting function gives reasonable charged particle pseudorapidity distributions, $dN_{\rm ch}/d\eta$ at central values of pseudorapidity for Pb+Pb collisions at LHC energies.[66] Therefore the same values ($a = 0.5$ and $b = 0.9$ GeV^{-2}) are used for both $p + p$ and p+Pb collisions, along with the same values of the strong coupling constant and parton cross section as in Ref.[66]

In these calculations, $p+p$ events are minimum-bias, including diffractive events. The MB p+Pb events include no restrictions on impact parameter. The nuclear modification factor, $R_{p\rm Pb}$, as a function of p_T is obtained by dividing the p+Pb distribution by the $p + p$ distribution, both calculated with the same version of AMPT, normalized by the number of binary $N + N$ collisions, $N_{\rm coll}$. The number of collisions is assumed to be equal to the number of participant nucleons in the Pb nucleus ($N_{\rm coll} = N^{\rm Pb}_{\rm part}$). The collision centrality is defined according to the number of charged hadrons within $|\eta| < 1$.

2.6. *Leading-order pQCD calculations (Z.-B. Kang, I. Vitev, H. Xing)*

The details of the calculations described here can be found in Ref.[67] A summary is given here. To leading order in the framework of factorized perturbative QCD,

single inclusive hadron production in $p + p$ collisions, $p(p_1) + p(p_2) \to h(p_h) + X$, can be written as[68]

$$\frac{d\sigma}{dyd^2p_T} = K\frac{\alpha_s^2}{s}\sum_{a,b,c}\int\frac{dx_1}{x_1}d^2k_{T_1}\, f_{a/N}(x_1,k_{T_1}^2)\int\frac{dx_2}{x_2}d^2k_{T_2}\, f_{b/N}(x_2,k_{T_2}^2) \times\int\frac{dz_c}{z_c^2}\, D_{h/c}(z_c)H_{ab\to c}(\hat{s},\hat{t},\hat{u})\delta(\hat{s}+\hat{t}+\hat{u}), \tag{23}$$

where y and p_T are the rapidity and transverse momentum of the produced hadron and $\sum_{a,b,c}$ runs over all parton flavors. In Eq. (23), $s = (p_1 + p_2)^2$; $D_{h/c}(z_c)$ is the fragmentation function (FF) of parton c into hadron h; $H_{ab\to c}(\hat{s},\hat{t},\hat{u})$ are hard-scattering coefficient functions dependent on the partonic Mandelstam invariants $\hat{s},\hat{t},\hat{u}$.[68] A phenomenological K factor is included to account for higher-order QCD contributions. The parton distribution functions, $f_{a,b/N}(x,k_T^2)$, are dependent on the longitudinal momentum fraction x and the partonic transverse momentum k_T. The k_T-dependence is included in order to incorporate the Cronin effect in $p + A$ collisions. A Gaussian form is assumed,[68]

$$f_{a/N}(x_1,k_{T_1}^2) = f_{a/N}(x_1)\frac{1}{\pi\langle k_T^2\rangle}e^{-k_{T_1}^2/\langle k_T^2\rangle}, \tag{24}$$

where $f_{a/N}(x_1)$ are the usual collinear PDFs in a nucleon. The factorization scale dependence has been suppressed in the arguments of $f_{a/N}$.

In $p+p$ collisions, $\langle k_T^2\rangle_{pp} = 1.8$ GeV$^2/c^2$. The CTEQ6L1 PDFs[69] are used with the fDSS parameterization of the parton-to-hadron fragmentation functions.[70] The factorization and renormalization scales are fixed to the transverse momentum of the produced particle, $\mu_F = \mu_R = p_T$, and are suppressed in Eqs. (23) and (24). An $\mathcal{O}(1)$ K-factor is found to give a good description of hadron production at both RHIC and LHC energies.

2.6.1. *Cold nuclear matter effects*

The $p+A$ (*e.g.* d+Au or p+Pb) nuclear modification factor, R_{pA}, is typically defined as:

$$R_{pA} = \left[\frac{d\sigma_{pA}}{dyd^2p_T}\right]\left[\frac{d\sigma_{pp}}{\langle N_{\rm coll}\rangle dyd^2p_T}\right]^{-1}, \tag{25}$$

where $\langle N_{\rm coll}\rangle$ is the average number of binary nucleon-nucleon collisions. The deviation of R_{pA} from unity reveals the presence of cold nuclear matter (CNM) effects in $p + A$ collisions.

A variety of CNM effects can affect particle production. This section describes those that arise from the elastic, inelastic and coherent scattering of partons in large nuclei.[71] The proton and neutron composition of the interacting nuclei are also accounted for. In particular, these effects include isospin, the Cronin effect, cold nuclear matter energy loss and dynamical shadowing. These effects have been well documented in the literature. Their implementation is briefly described here.

Isospin The isospin effect can be easily accounted for on average in the nuclear PDFs for a nucleus with mass number A and charge Z by:[72]

$$f_{a/A}(x) = \frac{Z}{A} f_{a/p}(x) + \left(1 - \frac{Z}{A}\right) f_{a/n}(x) \ , \tag{26}$$

assuming no modifications of the parton densities. In Eq. (26), $f_{a/p}(x)$ and $f_{a/n}(x)$ are the PDFs in a proton and a neutron, respectively. The neutron PDFs are related to those in the proton by isospin symmetry.

Cronin effect The Cronin effect has been well documented.[73] It can be modeled by initial-state multiple parton scatterings in cold nuclei and the corresponding induced parton transverse momentum broadening.[74,75] In particular, if the PDFs, $f_{b/A}(x_2, k_{T_2}^2)$, have a normalized Gaussian form, the random elastic scattering induces further k_T-broadening in the nucleus:

$$\langle k_{T_2}^2 \rangle_{pA} = \langle k_{T_2}^2 \rangle_{pp} + \left\langle \frac{2\mu^2 L}{\lambda_{q,g}} \right\rangle \zeta \ . \tag{27}$$

Here k_{T_2} is the transverse momentum component of the parton prior to the hard scattering, $\zeta = \ln(1 + \delta p_T^2)$, $\delta = 0.14$ $(\mathrm{GeV}/c)^{-2}$, $\mu^2 = 0.12$ $(\mathrm{GeV}/c)^2$, and $\lambda_g = (C_F/C_A)\lambda_q = 1$ fm. These parameters describe the RHIC data reasonably well.

Cold nuclear matter energy loss As the parton from the proton undergoes multiple scattering in the nucleus before the hard collision, it can lose energy due to medium-induced gluon bremsstrahlung. This effect can be easily implemented as a shift in the momentum fraction in the PDFs

$$f_{q/p}(x_1) \to f_{q/p}\left(\frac{x_1}{1 - \epsilon_{q,\,\mathrm{eff}}}\right) \ , \quad f_{g/p}(x_1) \to f_{g/p}\left(\frac{x_1}{1 - \epsilon_{g,\,\mathrm{eff}}}\right) \ . \tag{28}$$

Ideally, Eq. (28) should include a convolution over the probability of cold nuclear matter energy loss.[76] However, concurrent implementation of this distribution together with the Cronin effect and coherent power corrections is computationally very demanding. The main effect of fluctuations due to multiple gluon emission is an effective reduction in the fractional energy loss $\epsilon_{q,g\,\mathrm{eff}}$ relative to the mean value $\langle \epsilon_{q,g} \rangle = \langle \sum_i (\Delta E_i/E) \rangle$ where the sum runs over all medium-induced gluons. Here $\epsilon_{q,g\mathrm{eff}} = 0.7 \langle \epsilon_{q,g} \rangle$. The average cold nuclear matter energy loss is obtained by integrating the initial-state medium-induced bremsstrahlung spectrum first derived in Ref.[77] It also depends on the typical transverse momentum transfer squared per interaction between the parton and the medium and the gluon mean-free path λ_g. Therefore, the parameters are constrained to be the same as in the implementation of the Cronin effect, $\mu^2 = 0.12$ $(\mathrm{GeV}/c)^2$ and $\lambda_g = 1$ fm. This calculation of initial-state cold nuclear matter energy loss has been shown to give a good description of the nuclear modification of Drell-Yan production in fixed-target experiments.[76]

Dynamical shadowing Power-suppressed resummed coherent final-state scattering of the struck partons leads to shadowing effects (suppression of the cross section

in the small-x region).[78] The effect can be interpreted as the dynamical generation of parton mass in the background gluon field of the nucleus.[79] Thus

$$x \to x\left(1 + C_d \frac{\xi^2 (A^{1/3} - 1)}{-\hat{t}}\right) , \tag{29}$$

where x is the parton momentum fraction in the lead ion, $C_d = C_F(C_A)$ if the parton $d = q(g)$ in the $2 \to 2$ parton scattering $ab \to cd$, and ξ^2 represents the characteristic scale of the multiple scattering per nucleon. At RHIC energies, $\sqrt{s_{NN}} = 200$ GeV, $\xi_q^2 = C_F/C_A \xi_g^2 = 0.12$ GeV^2[78] gives a good description of the nuclear modification in d+Au collisions for both single hadron and dihadron production.[80]

2.7. *Initial-state Shadowing (G. G. Barnaföldi, J. Barette, M. Gyulassy, P. Levai, G. Papp and V. Topor Pop)*

The calculations in this section use the `kTpQCD_v2.0` code, based on a phenomenologically-enhanced, perturbative QCD improved parton model described in detail in Refs.[81,82] The main feature of this model is the phenomenologically-generalized parton distribution function employed to handle nonperturbative effects at relatively low-x and small p_T. The model includes intrinsic k_T broadening with the average k_T left as a free parameter to correct for nonperturbative effects. The k_T value is determined from $p + p$ data over a wide range of energies. Within the framework of this model, the k_T-broadening in $p + A$ and $A + A$ collisions is related to nuclear multiple scattering and can generate the Cronin enhancement[49,83] that appears within $3 \le p_T \le 9$ GeV/c from SPS to RHIC energies.

2.7.1. *Theoretical Background*

The `kTpQCD_v2.0` code calculates the invariant cross section for hadron production in $p + p$, $p + A$ and $A + A$ collisions at LO or NLO in the k_T-enhanced pQCD-improved parton model assuming collinear factorization. The code provides a Monte Carlo-based integration of the convolution,[82] written here for $p + p$ collisions,

$$\begin{aligned} E_h \frac{d\sigma_h^{pp}}{d^3 p_T} = \frac{1}{s} \sum_{abc} \int_{VW/z_c}^{1-(1-V)/z_c} \frac{dv}{v(1-v)} \int_{VW/vz_c}^{1} \frac{dw}{w} \int^{1} dz_c \\ \times \int d^2\vec{k}_{T_1} \int d^2\vec{k}_{T_2}\; f_{a/p}(x_1, \vec{k}_{T_1}, \mu_F^2)\, f_{b/p}(x_2, \vec{k}_{T_2}, \mu_F^2) \\ \times \left[\frac{d\widetilde{\sigma}}{dv}\delta(1-w) + \frac{\alpha_s(\mu_R)}{\pi} K_{ab,c}(\hat{s}, v, w, \mu_F, \mu_R, \mu_{\rm Fr})\right] \frac{D_c^h(z_c, \mu_{\rm Fr}^2)}{\pi z_c^2} . \end{aligned} \tag{30}$$

Here $d\widetilde{\sigma}/dv$ represents the Born cross section of the partonic subprocess $ab \to cd$ while $K_{ab,c}(\hat{s}, v, w, \mu_F, \mu_R, \mu_{\rm Fr})$ is the next order correction term. The proton and parton level NLO kinematic variables are (s, V, and W) and ($\hat{s}$, v, and w) respectively.[82,84–86] The various scales are μ_F, the factorization scale; μ_R, the renormalization scale; and $\mu_{\rm Fr}$ the fragmentation scale. The factorization and the renormalization scales are related to the momentum of the intermediate jet, $\mu_F = \mu_R = \kappa p_q$

where $\kappa = 2/3$, $p_q = p_T/z_c$ and z_c is the fraction of parton c momenta transferred to the final hadron h. The fragmentation scale is related to the final hadron momentum by $\mu_{\rm Fr} = \kappa p_T$.

The x-dependent proton parton distribution functions, $f_{a/p}(x, \mu_F^2)$, defined in the infinite momentum frame, are generalized to three dimensions by incorporating an initial k_T dependence,

$$f_{a/p}(x, \vec{k}_T, \mu_F^2) = g(\vec{k}_T) f_{a/A}(x, \mu_F^2) \ . \tag{31}$$

The two-dimensional initial transverse momentum distribution, $g(\vec{k}_T)$, with intrinsic parton k_T employed in these calculations is described in Refs.[81,82,87,88] The k_T distribution is described by a Gaussian,

$$g(\vec{k}_T) \ = \frac{1}{\pi \langle k_T^2 \rangle} e^{-k_T^2/\langle k_T^2 \rangle} \ . \tag{32}$$

Here $\langle k_T^2 \rangle$ is the width of the k_T distribution, related to the magnitude of the average parton transverse momentum by $\langle k_T^2 \rangle = 4 \langle k_T \rangle^2 / \pi$. This treatment was successfully applied at LO in Ref.,[81] along with a $K_{\rm jet}$-based NLO calculation.[89,90] In order to reproduce results for NN collisions at relatively low x, $\langle k_T^2 \rangle = 2.5$ GeV$^2/c^2$ was required.

The LO or NLO fragmentation functions, $D_c^h(z_c, \mu_{\rm Fr}^2)$, are the probability for parton c to fragment into hadron h with momentum fraction z_c at fragmentation scale $\mu_{\rm Fr}$. The MRST(cg)[91] parton densities are used in Eq. (31), along with the KKP parameterization[42] of the fragmentation functions. Both these sets can be applied at relatively small scales, $\mu_F^2 = \mu_{\rm Fr}^2 \approx 1.25$ GeV^2. Thus the results obtained in these calculations are applicable for $p_T \geq 2$ GeV/c.

2.7.2. *Incorporating Initial-State Nuclear Effects in $p + A$ and $A + A$ Collisions*

Proton-nucleus and nucleus-nucleus collisions can be described by incorporating the appropriate collision geometry and and nuclear shadowing. In the Glauber framework, the cross section for hadron production in an $A + A'$ collision can be written as an integral over impact parameter b:

$$E_h \frac{d\sigma_h^{AA'}}{d^3 p_T} = \int d^2b \, d^2r \ T_A(r) \ T_{A'}(|\vec{b} - \vec{r}|) \, E_\pi \, \frac{d\sigma_\pi^{pp}(\langle k_T^2 \rangle_{pA}, \langle k_T^2 \rangle_{pA'})}{d^3 p} \ . \tag{33}$$

Here the nuclear thickness function, $T_A(b) = \int dz \, \rho_A(b, z)$, employing the Woods-Saxon density distribution, is normalized so that $\int d^2b \, T_A(b) = A$.

The $p + p$ cross section from Eq. (30) includes increased k_T widths relative to $p + p$ collisions, Eq. (32), as a consequence of multiple scattering in nuclei, see Eq. (34). The increased width of the k_T distribution is taken into account by adding a function, $h_{pA}(b)$, that describes the number of effective $N+N$ collisions at impact

parameter b, weighted by the average transverse momentum squared imparted by each collision, to the width in $p + p$ collisions, $\langle k_T^2 \rangle_{pp}$,

$$\langle k_T^2 \rangle_{pA} = \langle k_T^2 \rangle_{pp} + C h_{pA}(b) \ . \tag{34}$$

The function $h_{pA}(b)$ is expressed in terms of the number of collisions suffered by the incoming proton in the target nucleus, $\nu_A(b) = \sigma_{NN} T_A(b)$, where σ_{NN} is the inelastic $N + N$ cross section:

$$h_{pA}(b) = \begin{cases} \nu_A(b) - 1 & \nu_A(b) < \nu_m \\ \nu_m - 1 & \text{otherwise} \end{cases} \ . \tag{35}$$

For heavy nuclei, the maximum number of collisions is $3 \leq \nu_m \leq 4$ with $C = 0.4$ GeV$^2/c^2$.

Finally, the nuclear PDFs are modified by shadowing.[47,92–94] This effect, as well as the isospin asymmetry, are taken into account on average using the scale independent parameterization of $S_{a/A}(x)$ adopted from Ref.,[87]

$$f_{a/A}(x, \mu_F^2) = S_{a/A}(x) \left[\frac{Z}{A} f_{a/p}(x, \mu_F^2) + \left(1 - \frac{Z}{A} \right) f_{a/n}(x, \mu_F^2) \right] \ , \tag{36}$$

where the neutron parton density, $f_{a/n}(x, \mu_F^2)$, is related to that of the proton. Results are shown with the EKS98,[92] EPS08[93] and HKN[94] parameterizations, as well as with the updated `HIJING` parameterization.[47] The EKS98, EPS08 and HKN parameterizations differ for quarks, antiquarks and gluons but are independent of impact parameter. The new `HIJING` parameterization differentiates between quarks and gluons but can include impact parameter dependence, as in Eq. (22).

3. Charged particles

In this section, results on the charged particle multiplicity and p_T distributions and the suppression factor $R_{p\mathrm{Pb}}$ as a function of p_T are compiled. These results are compared with the ALICE test beam data where available. Other, related, predictions for charged particle observables are also shown. The upcoming p+Pb run at the LHC can place important constraints on models of the initial state.

Note that the LHC magnet design requires the magnetic rigidity of the beams in the two rings to be the same. The proton beam, at 4 TeV, circulated in negative z-direction (toward negative rapidity) in the ALICE laboratory frame while a beam of fully-stripped Pb ions of (82/208) $\times$ 4 TeV/nucleon circulated in the positive z-direction (toward positive rapidity), implying Pb+p collisions if the first-named collision partner travels in the direction of positive rapidity, rather than p+Pb collisions, as the collisions are referred to throughout this text. This configuration resulted in a center of mass energy of $\sqrt{s_{NN}} = 5.02$ TeV, moving with a rapidity difference, $\Delta y_{NN} = 0.465$, in the direction of the proton beam.

It is important to note that the most of the predictions shown here were orginally made assuming that the proton circulated toward positive rapidity and the nucleus

toward negative rapidity, similar to the fixed-target configuration and also the convention for d+Au collisions at RHIC. In such cases, the low x nuclear parton distributions are probed at positive rapidity. Here and throughout the remainder of this paper, the results shown have been adjusted to the Pb+p convention of the ALICE data[2] unless otherwise explicitly noted.

ALICE reported the primary charged particle pseudorapidity density in the laboratory frame, $dN_{\rm ch}/d\eta_{\rm lab}$ in non single-diffractive (NSD) p+Pb collisions. The lab frame pseudorapidity is defined as $\eta_{\rm lab} = -\ln\tan(\theta/2)$ where θ is the polar angle between the direction of the produced charged particle and the beam axis. The primary particles are due to both prompt production in the collision and strong decays.

Calculations are typically performed in the center of mass frame but the pseudorapidity densities shown here have been also calculated in the lab frame. In the ALICE paper,[2] calculations in the center of mass frame were shifted by $\Delta y_{_{NN}}$ in the lab frame. This is only approximately correct since, at low p_T, the rapidity and pseudorapidity are not identical. The uncertainty on $dN_{\rm ch}/d\eta_{\rm lab}$ due to the choice of frame was estimated to be less than 6%.[2] It is worth noting that there is no ambiguity due to the calculational frame for identified particles thus the frame dependence is not discussed in later sections.

3.1. *Multiplicity distribution*

The calculations of the charged particle multiplicity distributions are described here. Saturation model predictions are discussed first, followed by event generator predictions and pQCD calculations with cold matter effects.

3.1.1. *Saturation Approaches (J. Albacete, A. Dumitru, H. Fujii, Y. Nara, A. Rezaeian, and R. Vogt)*

In the rcBK approach, used by Albacete and collaborators[95] and Rezaeian for $R_{p\rm Pb}$,[20,96] the initial condition for the evolution of the dipole scattering amplitude can be written as (see also Eq. (8)),

$$\mathcal{N}(r,x_0) = 1 - \exp\left[-\frac{1}{4}\left(r^2Q_s^2(x_0)\right)^\gamma \log\left(e+\frac{1}{r\Lambda}\right)\right] \ . \tag{37}$$

There are three sets of unintegrated gluon distributions that are solutions of the rcBK small-x evolution equations with the AAMQS initial condition in Eq. (37). The values of γ and $Q_{s0}^2(x_0=0.01)$ for protons that provide good fits to the e^-+p data are given in Table 3.1.1. Albacete *et al.* use all three initial conditions.[95] Rezaeian uses g1.119[96,97] in the calculations of $R_{p\rm Pb}$ in Sec. 3.3 but employs the b-CGC approach[20,27] to calculate $dN_{\rm ch}/d\eta$ here.

rcBK (J. Albacete, A. Dumitru, H. Fujii and Y. Nara) The calculation of $dN_{\rm ch}/d\eta$ by Albacete *et al.*,[95] employing $\gamma = 1.119$, in both the center of mass and

Table 2. The AAMQS initial conditions used in the dipole evolution of the rcBK approach for protons.[95,96]

Set	$Q_{s0}^2(x_0 = 0.01)$ (GeV$^2/c^2$)	γ
MV	0.200	1
g1.101	0.157	1.101
g1.119	0.168	1.119

lab frames, is shown in the dashed cyan curves in Fig. 1.

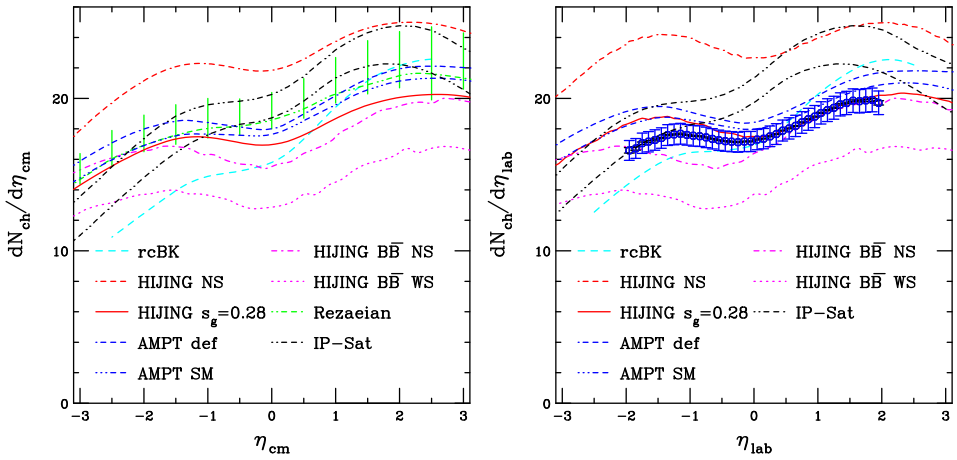

Fig. 1. Charged particle pseudorapidity distributions at $\sqrt{s_{NN}} = 5.02$ TeV in the CM (left) and lab (right) frames. The rcBK (dashed cyan) result is from Ref.[95] The band labeled Rezaeian (dot-dot-dash-dashed green with vertical bars outlining the uncertainty), described in Sec. 2.1, is only shown in the center-of-mass frame. The band showing the IP-Sat result described in Sec. 2.2 is outlined by the dot-dot-dash-dashed black curves. The `HIJING2.1` result without (NS, dot-dash-dash-dashed red) and with shadowing ($s_g = 0.28$, solid red) and the `HIJINGBB̄2.0` result without (dot dashed magenta) and with shadowing (dotted magenta) are also shown. Finally, the `AMPT − def` (dot-dash-dash-dashed blue) and `AMPT − SM` (dot-dot-dot-dash-dash-dashed blue) are given. The ALICE results from Ref.[2] are given on the right-hand side. The systematic uncertainties are shown in blue, the statistical uncertainties are too small to be visible on the scale of the plot.

b-CGC (A. Rezaeian) The results of calculations by Rezaeian[20,96] in the center of mass frame are shown by the green curves in Fig. 1. The vertical lines indicate the uncertainty in the predictions. The dipole forward (proton direction) amplitude is calculated in the b-CGC saturation model.[27] which has an explicit impact parameter dependence as well as approximately incorporates all known features of small-x physics. It describes the small-x HERA data, including diffractive data,[27] and also the RHIC and LHC data at small-x.[96,98–102] This framework also provides

an excellent description of the charged hadron multiplicity in d+Au collisions at RHIC in addition to $p+p$ and $A+A$ collisions over a range of energies.[96] For other saturation model predictions in minimum bias $p+A$ collisions at $\sqrt{s_{NN}} = 4.4$ TeV, see Ref.[103]

IP-Sat (P. Tribedy and R. Venugopalan) The calculation of the minimum-bias charged particle pseudorapidity distribution was performed in the k_T-factorization approach using the IP-Sat model[21] in Eq. (17). For the calculation of $dN_{\rm ch}/d\eta$ in the lab frame, a constant rapidity shift of 0.46 has been applied. The bands shown in Fig. 1 arises due to uncertainties in the parameters.

The charged particle multiplicity distributions obtained by the event generators HIJING, HIJINGB$\overline{\rm B}$2.0 and AMPT are now discussed.

3.1.2. HIJING2.1 *(R. Xu, W.-T. Deng and X.-N. Wang)*

The HIJING2.1 predictions in Fig. 1 are indicated by the dot-dash-dash-dashed curves without shadowing and the solid curves with $s_g = 0.28$. The difference between results with and without shadowing are largest for this calculation.

3.1.3. HIJINGB$\overline{\rm B}$2.0 *(G. G. Barnaföldi, J. Barette, M. Gyulassy, P. Levai, M.Petrovici and V. Topor Pop)*

The HIJINGB$\overline{\rm B}$2.0 predictions of $dN_{\rm ch}/d\eta$ in minimum bias collisions employ the values for the minijet cutoff and string-tension parameters of $p_0 = 3.1$ GeV/c and $\kappa = 2.0$ GeV/fm. These values are determined from fits to $p+p$ and $A+A$ systematics from RHIC to the LHC, see Ref.[53,54,56] for details. Note that these calculations assume no jet quenching.

The absolute normalization of $dN_{\rm ch}/d\eta$ is sensitive to the low p_T, $p_T < 2$ GeV/c, nonperturbative hadronization dynamics encapsulated in the Lund[57,58] JETSET[59] string fragmentation constrained by lower energy $e^+ + e^-$, $e^\pm + p$, and $p+p$ data. The default HIJING1.0 shadowing parametrization leads to substantial reduction of the global multiplicity at the LHC. The HIJINGB$\overline{\rm B}$2.0 results without shadowing are substantially reduced relative to the same predictions with HIJING1.0[43,52] because both the default minijet cutoff $p_0 = 2$ GeV/c and vacuum string tension $\kappa_0 = 1$ GeV/fm used in HIJING1.0 are generalized to vary monotonically with $\sqrt{s_{NN}}$ and A. As discussed in Ref.,[53,54,56] systematics of multi-particle production in $A+A$ collisions from RHIC to the LHC are used to fix the $\sqrt{s_{NN}}$ and A dependence of p_0 and κ. The resulting dependencies, $p_0(s,A) = 0.416\sqrt{s}^{0.191}A^{0.128}$ GeV/c and $\kappa(s,A) = \kappa_0(s/s0)^{0.04}A^{0.167}$ GeV/fm[56] lead to $p_0 = 3.1$ GeV/c and $\kappa = 2.1$ GeV/fm in p+Pb collisions at 5.02 TeV.

Constant values of the cutoff are employed in $p+p$ collisions, independent of the incident energy, $p_0^{pp} = 2$ GeV/c, and string tension, $\kappa_{pp} = 1.9$ GeV/fm. Note that, even without shadowing, the increase of p_0 from 2 GeV/c in $p+p$ collisions to 3.1

GeV/c in p+Pb collisions causes a reduction in the minijet cross section and hence the final pion (charged particle) multiplicity. Such a reduction is also required to fit the slow growth (by a factor of 2.2) in the $A + A$ charged particle multiplicity from RHIC to LHC.[104] This reduction could be interpreted as phenomenological evidence for gluon saturation beyond leading twist shadowing.

3.1.4. AMPT *(Z.-W. Lin)*

The AMPT default and string melting calculations are shown in the blue curves in Fig. 1. The differences in the two scenarios is not large. Indeed it is much smaller than models with and without shadowing. These differences can arise from several sources: the relative rescattering strengths in the parton and hadron stages; the hadronization models; or a combination of rescattering and hadronization.

3.1.5. *Forward/Backward difference (R. Vogt)*

The event generator calculations produce distributions that do not show a strong forward/backward difference between the lead and proton peaks. The CGC-based calculations, however, show a much stronger dependence of the results on pseudorapidity, in both frames.

The charged particle multiplicity results can be further quantified by comparing the measured to predicted particle density at midrapidity, near the proton peak, $\eta_{\rm lab} = -2$, and the lead peak, $\eta_{\rm lab} = 2$. The absolute values of $dN_{\rm ch}/d\eta_{\rm lab}$ at $\eta_{\rm lab} = -2$, 0 and 2, along with the ratio R of the multiplicities at $\eta_{\rm lab} = 2$ to $\eta_{\rm lab} = -2$) are given in Table 3.1.5. The ALICE results as well as the model results included both here and in the ALICE paper[2] are given. There are two tabulated values for both HIJINGB$\overline{\rm B}$2.0 NS (no shadowing) and WS (with shadowing). The first were shifted from the center-of-mass to the lab frame by the ALICE collaboration and the second were direct lab frame calculations.

3.1.6. *Centrality Dependence of* $dN_{\rm ch}/d\eta$

Here we present two calculations of the centrality dependence of the charged particle multiplicity distributions.

AMPT **(Z. Lin)** Figure 2 shows the pseudorapidity rapidity distributions calculated in the center-of-mass frame by AMPT − def. Results are shown for p+p and minimum bias p+Pb collisions as well as for six different centrality classes. In AMPT, the $p + p$ events are minimum bias events, including diffractive events.

Since the ratio $R_{p\rm Pb}$ is normalized by a factor proportional to the number of binary nucleon-nucleon collisions, $N_{\rm coll}$, the number of collisions in the same centrality classes as included in Fig. 2 is shown in Table 3.1.6. In AMPT, $N_{\rm coll}$ is assumed to be equivalent to the total number of participant nucleons in the Pb nucleus, $N_{\rm part}^{\rm Pb}$. Because there is some model dependence in the definition of centrality bins, it is

Table 3. Comparison of values of $dN_{\rm ch}/d\eta_{\rm lab}$ at $\eta_{\rm lab} = -2$, 0, 2 and the ratio $dN_{\rm ch}/d\eta_{\rm lab}|_{\eta_{\rm lab}=2}/dN_{\rm ch}/d\eta_{\rm lab}|_{\eta_{\rm lab}=-2}$, denoted by R below. The tabulated IP-Sat result is the average of the upper and lower limits depicted on the right-hand side of Fig. 1. The $*$ on HIJINGBB̄2.0 indicates that the calculations have been shifted to the lab frame by the ALICE Collaboration while the † are results provided by V. Topor Pop *et al.*. Adapted from Ref.[2]

	$dN_{\rm ch}/d\eta_{\rm lab}$			R
	-2	0	2	
ALICE	16.65 ± 0.65	17.24 ± 0.66	19.81 ± 0.78	1.19 ± 0.05
Saturation Models				
IP-Sat	17.55	20.55	23.11	1.32
KLN	15.96	17.51	22.02	1.38
rcBK	14.27	16.94	22.51	1.58
HIJING-based				
HIJING2.1 NS (no shad)	23.58	22.67	24.96	1.06
HIJING2.1 WS ($s_g = 0.28$)	18.30	17.49	20.21	1.10
HIJINGBB̄2.0 NS*	20.03	19.68	23.24	1.16
HIJINGBB̄2.0 NS†	16.84	16.39	19.68	1.16
HIJINGBB̄2.0 WS*	12.97	12.09	15.16	1.17
HIJINGBB̄2.0 WS†	13.98	13.71	16.73	1.20
AMPT				
AMPT − Def	19.07	18.56	21.65	1.14
AMPT − SM	18.14	18.10	20.84	1.15
DPMJET	17.50	17.61	20.67	1.18

Table 4. Centrality classes of p+Pb events from AMPT − SM The centrality is determined from the number of charged hadrons within $|\eta| < 1$ in the center-of-mass frame.

Bin	$\langle b \rangle$ (fm)	$b_{\rm min}$ (fm)	$b_{\rm max}$ (fm)	$N^{\rm Pb}_{\rm part}$	$N^{\rm Pb}_{\rm part,\,in}$	$\langle N_{\rm ch}(\lvert\eta\rvert < 1)\rangle$
MB	5.84	0.0	13.2	7.51	5.37	36.1
0-5%	3.51	0.0	8.8	15.70	12.12	99.9
5-10%	3.76	0.0	9.4	14.19	10.71	79.6
10-20%	4.00	0.0	9.9	12.93	9.59	66.5
20-40%	4.56	0.0	12.0	10.70	7.69	49.6
40-60%	5.65	0.1	13.2	7.30	5.03	31.4
60-80%	7.08	0.1	13.2	3.77	2.50	15.9
80-100%	8.08	0.2	13.2	1.85	1.11	5.5

worthwhile noting that other calculations of this same quantity may give somewhat different results. Here, the centrality of p+Pb collisions is defined according to the number of charged hadrons within $|\eta| < 1$. Table 3.1.6 shows various information for each centrality class in the center-of-mass frame, including the average, minimum and maximum impact parameters, $N^{\rm Pb}_{\rm part}$, the number of participant Pb nucleons involved in inelastic collisions, $N^{\rm Pb}_{\rm part,\,in}$, and the average number of charged particles within $|\eta| < 1$ from AMPT − SM. Note that the AMPT − SM values in Table 3.1.6 are essentially the same as those for AMPT − def except for the average number of charged particles (last column).

In Fig. 2, the $40 - 60\%$ centrality bin gives a distribution that is very close to

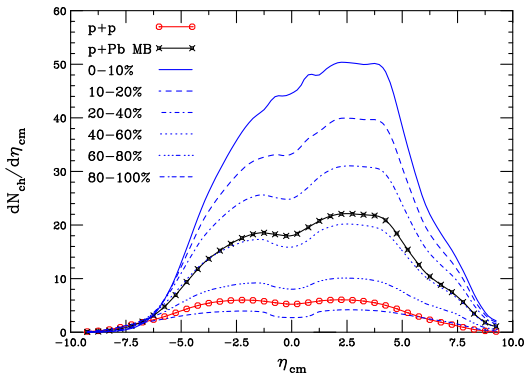

Fig. 2. Charged particle pseudorapidity distributions in the center of mass frame for $p+p$, p+Pb minimum bias and six of the centrality bins defined in Table 3.1.6 as calculated in `AMPT`.

the min-bias result, in particular on the proton side. The most central bin is the most asymmetric distribution, as well as the largest in magnitude. On the other hand, the distribution for the $80-100\%$ centrality bin is symmetric around $\eta_{\rm cm} = 0$ and lower in magnitude than the $p+p$ distribution.

b-CGC (A. Rezaeian) In Fig. 3, the charged hadron multiplicity obtained from k_T factorization in the b-CGC approach is shown the $0-20\%$, $20-40\%$, $40-60\%$, $60-80\%$ centrality bins as well as minimum-bias collisions.[20] The impact parameter dependence of the saturation model is crucial for defining the collision centrality. The largest asymmetry in the multiplicity distribution is observed in more central collisions while, for peripheral collisions such as the $60-80\%$ most central, the system becomes more similar to that produced in $p+p$ collisions. This is reflected in the total charged hadron multiplicity distribution.

Note that for all results shown in Fig. 3, a fixed minijet mass equal to current-quark mass is assumed for all energies/rapidities and centralities. Since the minijet mass is related to pre-hadronization/hadronization stage and cannot be obtained from saturation physics, it was fixed by fitting lower energy minimum-bias data. In very peripheral collisions where the system becomes more similar to symmetric $p+p$ collisions, this assumption is less reliable. More importantly, one should also note that the k_T factorization employed here is only proven in asymmetric $p+A$ collisions at small x. Therefore, for more peripheral collisions, the current CGC prescription may be less reliable.

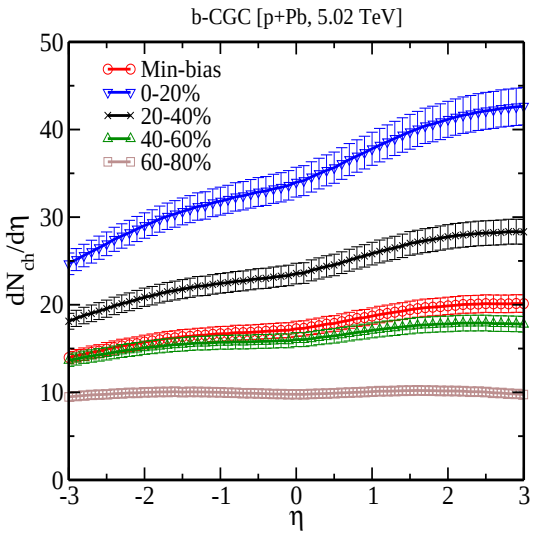

Fig. 3. Charged particle pseudorapidity distributions in the center of mass frame of p+Pb collisions at various centralities within the b-CGC saturation model. The $\sim 5\%$ theoretical uncertainties arising from fixing the overall normalization at RHIC are also shown. From Ref.[20]

3.2. *Transverse Momentum distribution*

3.2.1. *Compilation of midrapidity results (J. Albacete, A. Dumitru, H. Fujii, Y. Nara, R. Xu, W.-T. Deng, X.-N. Wang, G. G. Barnaföldi, J. Barette, M. Gyulassy, P. Levai, M. Petrovici, V. Topor Pop, Z. Lin and R. Vogt)*

The midrapidity, $|\eta| < 0.8$, charged hadron p_T distributions are shown on the left-hand side of Fig. 4 for rcBK,[95] `HIJINGBB̄2.0`, and `AMPT`. The `HIJINGBB̄2.0` distributions are similar to the rcBK results, albeit somewhat higher for $p_T > 10$ GeV/c. The `AMPT` distributions, on the other hand, drop faster at low p_T than the other results but then become harder at high p_T. The `AMPT` results are essentially independent of whether string melting is included or not while the `HIJINGBB̄2.0` results without shadowing lie above those with shadowing.

The right-hand side of Fig. 4 shows several options for cold matter effects in `HIJING2.1` relative to $p + p$ collisions. The $p + p$ result is unscaled while the p+Pb curves with decoherent hard scatterings (DHC) without shadowing, DHC with shadowing, and shadowing only are separated from each other, starting from the $p + p$ result, by a factor of 100.

3.2.2. *reBK at $y = 0$, 2 (J. Albacete, A. Dumitru, H. Fujii and Y. Nara)*

Fig. 5 shows the p_T spectrum in $p + p$ (left) and p+Pb (right) collisions at different rapidities for the AAMQS initial conditions, see Table 3.1.1. Near central rapidity,

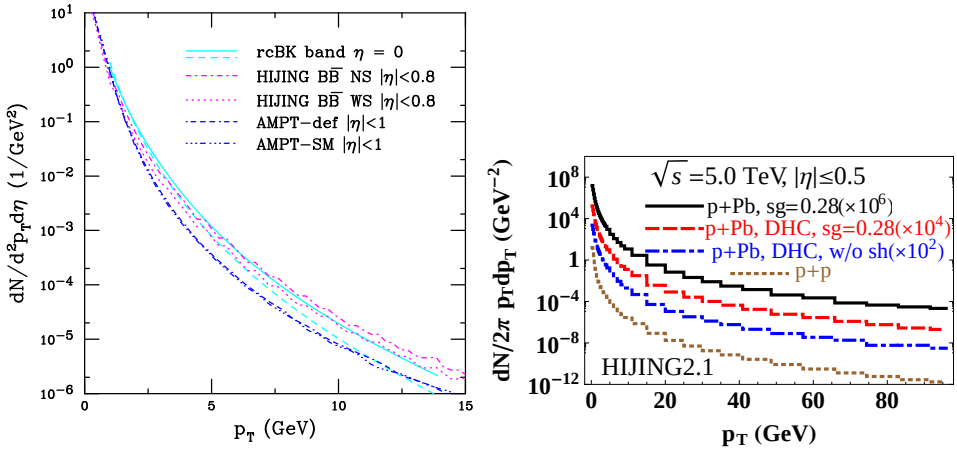

Fig. 4. (Left) Charged particle p_T distributions at $\sqrt{s_{NN}} = 5.02$ TeV. The solid and dashed cyan curves outline the rcBK band calculated by Albacete *et al.*[95] The magenta curves, calculated with `HIJINGBB̄2.0` as described in Sec. 2.4 are presented without (dot-dashed) and with (dotted) shadowing. The `AMPT` results, given by the dot-dash-dash-dashed (default) and dot-dot-dot-dashed (SM) blue curves, are described in Sec. 2.5. (Right) The charged hadron p_T distribution in p+Pb collisions with different `HIJING2.1` options, scaled by the indicated factors to separate the curves. The $p + p$ distribution is shown for comparison.

k_T-factorization is employed while at forward rapidities (in the proton direction) the hybrid formalism is applied. The bands correspond to uncertainty estimates due to small variations in the scale entering the coupling and fragmentation functions.

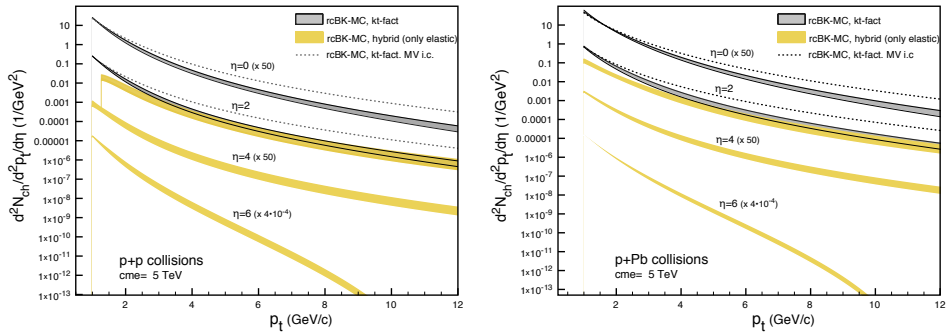

Fig. 5. The predicted transverse momentum spectrum in $p + p$ (left) and minimum-bias p+Pb (right) collisions at $\sqrt{s} = 5$ TeV at different rapidities (with the convention that the proton beam moves toward forward rapidity). From Ref.[95]

3.2.3. *Flow Coefficients obtained with* AMPT *(Z. Lin)*

The flow coefficients $v_n\{2\}$ ($n = 2, 3, 4$) in this study are calculated employing the two-particle cumulant method with $v_n = \sqrt{\langle \cos[n(\phi_i - \phi_j)]\rangle}$, where $\cos[n(\phi_i - \phi_j)]$ is averaged over all particle pairs in the specified phase space with both particles of each pair coming from the same event.

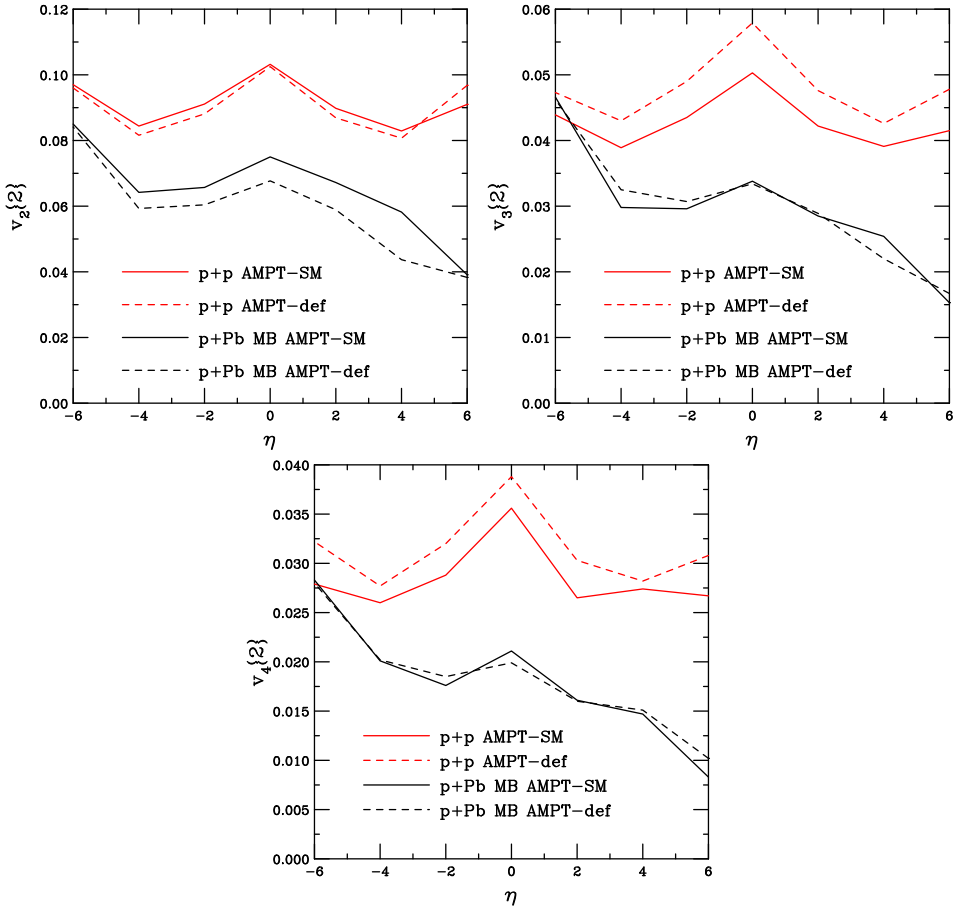

Fig. 6. The flow coefficients $v_2\{2\}$ (top left), $v_3\{2\}$ (top right), and $v_4\{2\}$ (bottom) of charged particles as a function of η in $p+p$ and minimum-bias p+Pb collisions. The results are shown for both AMPT − def and AMPT − SM.

Figure 6 shows $v_2\{2\}$, $v_3\{2\}$ and $v_4\{2\}$ for unidentified charged particles as a function of η in $p + p$ and minimum-bias p+Pb collisions from AMPT − def and AMPT − SM. The magnitude of the flow coefficients generally decreases with increasing n. There is a local maximum at $\eta \sim 0$. While the $p+p$ results are approximately

symmetric, as expected, the p+Pb results exhibit a strong asymmetry. In the direction of the proton beam, the p+Pb coefficients increase to approach the magnitudes of the $p + p$ coefficients.

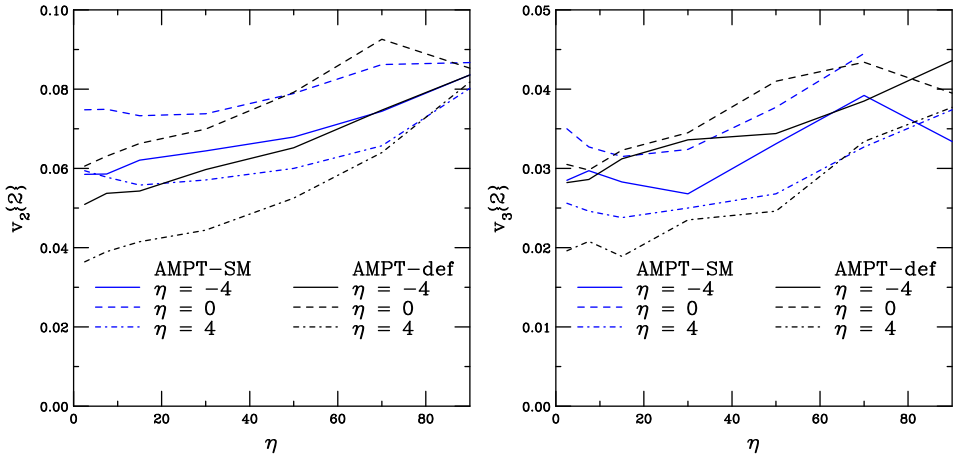

Fig. 7. The flow coefficients $v_2\{2\}$ (left) and $v_3\{2\}$ (right) as a function of centrality in p+Pb collisions at $\langle\eta\rangle = 4$, 0, and -4. The results are shown for both AMPT − def and AMPT − SM.

Figure 7 shows the centrality dependence of $v_2\{2\}$ and $v_3\{2\}$ in p+Pb collisions. Three different η ranges are shown: $-5 \le \eta \le -3$, $|\eta| \le 1$, and $3 \le \eta \le 5$ ($\langle\eta\rangle = -4$, 0 and 4 respectively. The coefficients increase from central to peripheral events for both AMPT − SM and AMPT − def. The coefficients are largest at $\langle\eta\rangle = 0$ while those at $\langle\eta\rangle = 4$, in the direction of the Pb beam, are smallest, consistent with the results in Fig. 6.

3.3. *Medium Modification Factor* $R_{p\mathrm{Pb}}$

3.3.1. $R_{p\mathrm{Pb}}(p_T)$ *at* $\eta \sim 0$

We now turn to the medium modification or suppression factors, defined as the ratio of the $p + A$ to $p + p$ cross section,

$$R_{p\mathrm{Pb}}(p_T, \eta; b) = \frac{1}{N_{\mathrm{coll}}(b)} \frac{d\sigma_{p\mathrm{Pb}}/d\eta dp_T}{d\sigma_{pp}/d\eta dp_T} \ . \tag{38}$$

Results are shown first for $R_{p\mathrm{Pb}}(p_T)$ for charged hadrons (pions) in Fig. 8. Standard shadowing calculation are shown on the left-hand side, results with event generators in the center, while CGC calculations and results with energy loss in cold matter are shown on the right-hand side.

Cronin effect expected at the LHC: dipole formulation (B. Z. Kopeliovich and J. Nemchik) At LHC energies, hadron production is dominated by

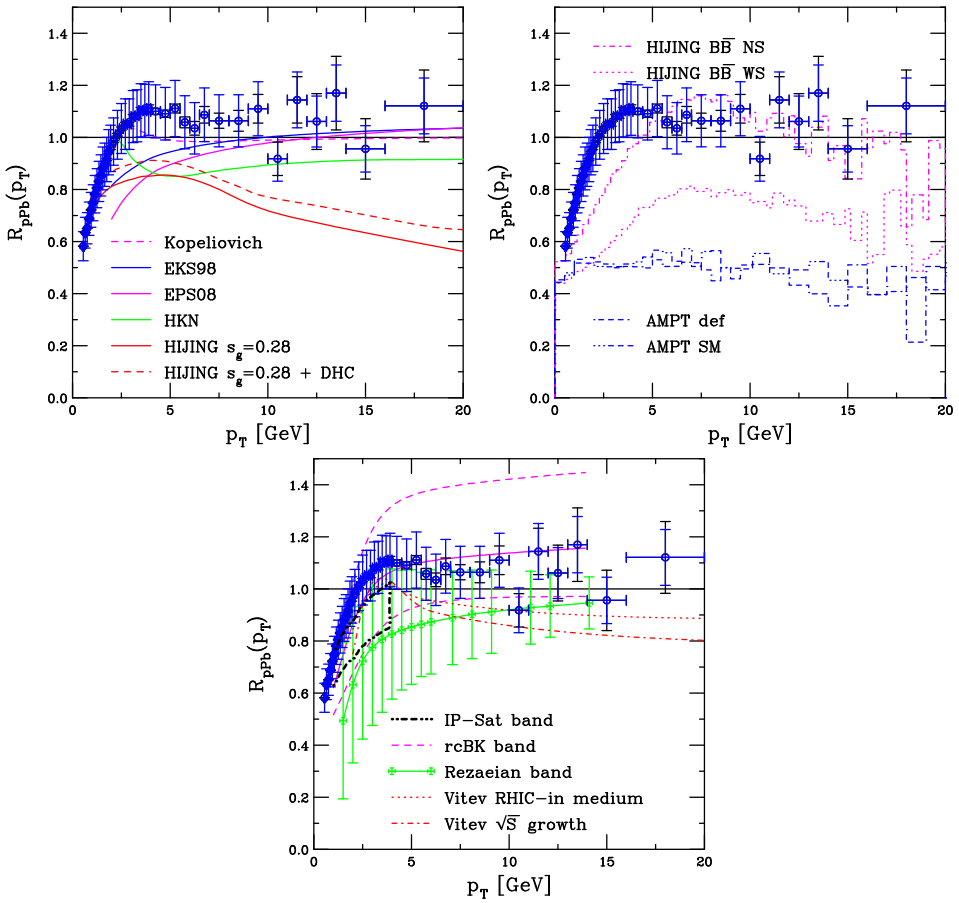

Fig. 8. Charged particle $R_{p\mathrm{Pb}}p_T$ at $\sqrt{s_{NN}} = 5.02$ TeV at $\eta \sim 0$. (Top left) Results with more 'standard' shadowing (labeled EKS98, EPS08 and HKN) described in Sec. 2.7, Refs.[105,106] (labeled Kopeliovich) and the `HIJING2.1` shadowing parameterization in Eq. (21) are compared. The difference in the `HIJING2.1` curves depends on whether the hard scatterings are coherent or not, see Sec. 2.3. (Top Right) `HIJINGBB̄2.0` with and without shadowing (Sec. 2.4) compared to `AMPT` default and with string melting (Sec. 2.5). (Bottom) The band from rcBK saturation model calculations by Albacete *et al.* and Rezaeian with $N = 5$ and varying α_s^{in} described in Sec. 2.1 are compared to IP-Sat calculations by Tribedy and Venugopalan in Sec. 2.2 and calculations by Vitev *et al.* discussed in Sec. 2.6. (More detailed results for the uncertainties in Rezaeian's calculation at other rapidities can be found in Fig. 10.) The ALICE results from Ref.[3] are also shown. The systematic uncertainties are shown in blue, the statistical uncertainties are in black.

gluon fragmentation. The dipole formalism, on the light cone, is employed in the target rest frame, leading to the factorized expression for hadron production: a convolution of the projectile gluon PDF, the gluon fragmentation function, and the gluon splitting, $g \to gg$, cross section.[105] The gluon splitting cross section can be

written in the dipole representation as

$$\frac{d\sigma(gA \to g_1 gX)}{d^2p_T\, dy_1} = \int d^2b \int d^2r_1 d^2r_2\, e^{i\vec{p}_T\cdot(\vec{r}_1-\vec{r}_2)}\, \overline{\Psi^*_{gg}(\vec{r}_1,\alpha)\Psi_{gg}(\vec{r}_2,\alpha)}$$
$$\times \left[1 - e^{-\frac{1}{2}\sigma^N_{3g}(r_1,x)T_A(b)} - e^{-\frac{1}{2}\sigma^N_{3g}(r_2,x)T_A(b)} + e^{-\frac{1}{2}\sigma^N_{3g}(\vec{r}_1-\vec{r}_2,x)T_A(b)}\right] \quad ,$$

where the subscript 1 indicates the hadronizing gluon involved in inclusive high p_T hadron production by gluon fragmentation. The momentum fraction of radiation gluon g_1 is defined as $\alpha = p^+_{g_1}/p^+_g$, the transverse coordinates of the emitted gluons are r_1 and r_2, x is the momentum fraction of the gluon in the target nucleus and $T_A(b)$ is the nuclear thickness function. The distribution function, $\Psi_{gg}(\vec{r},\alpha)$, derived in,[106] describes the $|gg\rangle$ Fock component of the projectile gluon light-cone wavefunction, including the nonperturbative gluon interaction. It is characterized by the localization of gluons at a short relative transverse separation, $r_0 \approx 0.3$ fm. The $3g$ dipole cross section, σ^N_{3g}, is expressed as a combination of the $\bar{q}q$ dipole cross sections, extracted from phenomenology and DIS data, $\sigma^N_{3g}(r) = \frac{2}{9}\Big\{\sigma_{\bar{q}q}(r) + \sigma_{\bar{q}q}(\alpha r) + \sigma_{\bar{q}q}[(1-\alpha)r]\Big\}$[i].

Multiple interactions of higher Fock components (containing more than one gluon) of the incident proton in the nucleus leads to a suppression of the dipole cross section, known as gluon shadowing. The magnitude of the suppression factor R_g was evaluated in Ref.[106] and, as a consequence of the small gluon separation, r_0, the modification was found to be rather small. Thus, at first order, gluon shadowing can be implemented by the simple replacement $\sigma^N_{3g} \to R_g(x,Q^2,b)\sigma_{3g}$ in Eq. (39). The results Ref.[105] at $\sqrt{s} = 5$ TeV are given by the solid cyan curve on the left-hand side of Fig. 8.

The Cronin enhancement is rather weak with a maximum of $R_{pPb} \sim 1.05$ at $p_T \sim 3$ GeV/c. The height of the maximum is extremely sensitive to the strength of gluon shadowing. The enhancement could completely disappear, or even change sign, if the strength of gluon shadowing was underestimated in Ref.[106]

Results with standard shadowing parameterizations (G. G. Barnaföldi, J. Barette, M. Gyulassy, P. Levai, G. Papp and V. Topor Pop) The left-hand side of Fig. 8 also shows $R_{p\mathrm{Pb}}(p_T)$ for several standard shadowing functions: EKS98[92] (blue), EPS08[93] (magenta), and HKN[94] (green). All three were calculated in the rapidity interval $|\eta| < 0.3$, in the center of mass frame. Since none of these parameterizations include impact parameter dependence, the results are independent of collision centrality. For details, see Ref.[55] For other results employing `kTpQCD_v2.0`, see Refs.[81,90,107,108,111]

`HIJING2.1` **(R. Xu, W.-T. Deng and X.-N. Wang)** Two `HIJING2.1` calculations including shadowing with parameter $s_g = 0.28$ are shown with the standard

[i]The x dependence of σ^N_{3g} has been suppressed.

shadowing parameterizations on the left-hand side of Fig. 8. They are lower than the other calculations at high p_T. Including the decoherent hard scatterings moves $R_{p\mathrm{Pb}}$ closer to unity over all p_T.

HIJINGBB̄2.0 (G. G. Barnaföldi, J. Barette, M. Gyulassy, P. Levai, M. Petrovici and V. Topor Pop) The HIJINGBB̄2.0 results without (NS) and with (WS) shadowing in the central rapidity region, $|\eta| < 0.8$, are shown in the central panel of Fig. 8. Including shadowing and strong color field effects reduces $R_{p\mathrm{Pb}}$ from unity to ~ 0.7 for $5 < p_T < 10$ GeV/c. This is similar to CGC predictions in the KKT04 model.[109] Further, similar, results for $R_{p\mathrm{Pb}}(p_T)$ are found in Ref.[110,111] using LO pQCD collinear factorization with the HIJING2.0 shadowing parameterization,[47] the GRV proton PDFs,[62] and hadron fragmentation functions from Ref.[42]

AMPT (Z. Lin) The AMPT results, evaluated in the center of mass frame pseudorapidity interval $|\eta| < 1$ are also shown in the central panel of Fig. 8. In minimum bias collisions, $N_{\mathrm{coll}} = 7.51$ in AMPT. There is an $\approx 50\%$ suppression of charged hadron production for the entire p_T range shown, considerably lower than that obtained in the other calculations shown. The statistical uncertainty, not shown in Fig. 8, becomes large for $p_T > 10$ GeV/c. There is little difference in $R_{p\mathrm{Pb}}$ between the default and string melting options of AMPT.

The right-hand side of Fig. 8 compares rcBK results from Albacete *et al.* and Rezaeian to IP-Sat calculations by Tribedy and Venugopalan and pQCD calculations by Vitev *et al.* including energy loss in cold matter.

rcBK predictions (J. Albacete, A. Dumitru, H. Fujii, Y. Nara, A. Rezaeian and R. Vogt) Rezaeian's calculation assumes $N_{\mathrm{coll}} = 6.9$ in minimum bias p+Pb collisions.[112] To compare these calculations to data, it is necessary to rescale the results to match the normalization N_{coll} to the experimental value. The NLO MSTW proton PDFs[113,114] and the NLO KKP fragmentation functions[42] are employed. The rcBK equation, Eq. (7), accounts for the rapidity/energy evolution of the dipole but does not include impact parameter dependence explicitly. In the minimum-bias analysis here the initial saturation scale, $Q_{0s}(x_0 = 0.01)$, is considered as an impact-parameter averaged value and extracted from minimum-bias data. Thus, fluctuations in particle production and any other possible nonperturbative effects are incorporated into this average value of Q_{0s}. It was found that $Q_{0p}^2(x_0 = 0.01) \approx 0.168$ GeV$^2/c^2$ with $\gamma \approx 1.119$ provides a good description of small-x proton data from the LHC, HERA and RHIC,[15,115] see also Ref.[97] These values are employed in the rcBK description of the projectile proton.

Here the difference between protons and nuclei originates from the different initial saturation scales, Q_{0s}, in the rcBK equation, see Eq. (8). The initial nuclear saturation scale Q_{0A} at a given centrality is generally less constrained than that in the proton because the small-x data from d+Au collisions at RHIC and DIS data on heavy target are limited with rather large uncertainties, leading to correspondingly

larger uncertainties on Q_{0A},[20]

$$(3-4)\ Q_{0p}^2 \leq Q_{0A}^2(x_0 = 0.01) \leq (6-7)\, Q_{0p}^2\ . \tag{39}$$

The role of fluctuations on particle production and other nonperturbative effect, including the impact-parameter dependece of the initial nuclear saturation scale are effectively incorporated into the average value of Q_{0A}^2 assuming $Q_{0A}^2 = NQ_{0p}^2$ is constrained by experimental data. Figure 8 shows results at $\eta = 0$ with $N = 5$ and varying $\alpha_s^{\rm in}$. For results over the full range of N in Eq. (39), see Fig. 10.

On the other hand, Albacete *et al* let the initial nuclear saturation scale be proportional to the nuclear density at each point in the transverse plane. They compare two different methods,[95]

$$Q_{0A}^2(b, x_0) = N_{\rm part}(b) Q_{0p}^2(x_0) \ \text{ and} \tag{40}$$

$$= N_{\rm part}^{1/\gamma}(b) Q_{0p}^2(x_0)\ . \tag{41}$$

The second option is an ad hoc way of correcting for the violation in the additivity of the nucleon number in the dipole scattering amplitude at small dipole sizes resulting from the fact that $\gamma \neq 1$. The position of the nucleons in the transverse plane is simulated by Monte Carlo methods makes it possible to account for geometry fluctuations which can have large numerical impact.[95]

IP-Sat (P. Tribedy and R. Venugopalan) The nuclear modification factors for inclusive charged particles in minimum-bias collisions employing the IP-Sat approach is done using k_T-factorization approach at $y = 0$ in the center-of-mass frame. The LO KKP fragmentation functions[42] are used to compute the inclusive charged hadron spectrum from the gluon distribution. The details of the parameters used can be found in Refs.[34,35] The band shows the uncertainty in the calculation. Note that $R_{p\rm Pb}$ approachs unity with increasing p_T.

Cold matter energy loss (Z.-B. Kang, I. Vitev and H. Xing) The red curves on the right-hand side of Fig. 8 are results including cold matter energy loss at $y = 0$, see Sec. 2.6. The upper curve corresponds to parameters determined for RHIC while the lower curve includes a potential enhancement in these parameters for LHC energies. There is a very small "Cronin peak" in the low p_T region. The peak is very close to unity and not as pronounced as that seen in lower energy fixed-target experiments because dynamical shadowing strongly suppresses particle production in this region. Initial-state energy loss is also larger because diagrams with incident gluons make a bigger contribution to the cross section. At high p_T, a small, ~ 15 %, suppression remains, also due to cold nuclear matter energy loss.

The preliminary data are most compatible with the saturation model calculations, albeit the uncertainties of these calculations are still rather large. The calculation by Kopeliovich is also in relative agreement with the data. However, we note that none of the calculations available for both $dN_{\rm ch}/d\eta$ and $R_{p\rm Pb}$ at $\eta \sim 0$ agree with both observables simultaneously.

3.3.2. HIJING2.1 *parton vs. hadron* R_{pA} *(R. Xu, W.-T. Deng and X.-N. Wang)*

On the left-hand side of Fig. 9, the nuclear modification factor of the final-state parton p_T spectra, $R_{pA}(p_T)$, is shown for p+Pb collisions at the LHC. Here $\langle N_{\rm coll}\rangle$ is the average number of binary nucleon-nucleon interactions in $p+A$ collisions. It is clear that both nuclear shadowing and the hard-soft coupling can suppress the p_T spectra of the produced partons. These features will transferred to the final hadron spectra after hadronization, as shown on the right-hand side of the Figure.

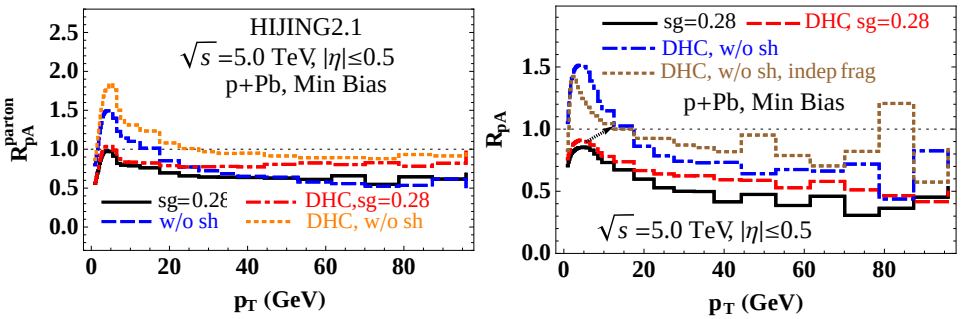

Fig. 9. (Left) The nuclear modification factor of the parton p_T spectra in p+Pb collisions. (Right) The charged hadron nuclear modification factor with different HIJING2.1 options. The arrow indicates the most probable trend of the nuclear modification factor to transition from the low to the high p_T regions.

The predicted charged hadron nuclear modification factors are shown on the right-hand side of Fig. 9. The enhancement at intermediate p_T is due to the k_T broadening arising from multiple scattering. Parton shadowing, the modified soft-hard coupling and enhanced density of gluon jets due to valence quark conservation all contribution to suppression of the charged hadron spectra. In addition, string fragmentation can further suppress the high p_T hadron spectra compared to independent fragmentation.

Since the effects of parton shadowing will disappear at large p_T[48] due to the QCD evolution not yet included here while hard and soft scatterings will decohere, the nuclear modification factor will likely follow the default result, including DHC, at low p_T. At large p_T, the result should approach that with DHC effects but no shadowing. There may be further possible modifications due to the hadronization of multiple jets. In Fig. 9, this probable trend is indicated by the arrow joining these two results at intermediate p_T.

3.3.3. $R_{p\rm Pb}(p_T)$ *at* $|\eta| \neq 0$

Here we show several results for the charged particle $R_{p\rm Pb}$ away from central rapidity. Two employ the rcBK approach but with different initial conditions. The last

is a pQCD calculation including cold matter energy loss.

Rezaeian rcBK (A. Rezaeian) In Fig. 10, $R_{pA}^{\rm ch}(p_T)$ is shown for minimum bias collisions at $\eta = 0$, 2, 4, and 6 (with the convention that the proton beam moves toward forward rapidity) obtained from the hybrid factorization Eq. (4) supplemented with rcBK evolution. The band labeled CGC-rcBK includes uncertainties associated with the variation of initial nuclear saturation scale, Q_{0A}^2, constrained in Eq. (39), as well as uncertainties due to the choice of factorization scale, $\mu_F = 2p_T$, p_T, and $p_T/2$, in Eq. (4). The values of N scale the nuclear saturation scale relative to that in the proton, $Q_{0A}^2 = NQ_{0p}^2$, with $3 < N < 7$. The variation of the results with N represents an effective variation with centrality and incorporating possible effects of fluctuations. Going forward in proton rapidity reduces the range of the results and lessens the dependence on N.

As shown in Ref.,[97] the RHIC data unfortunately cannot fix the value of $\alpha_s^{\rm in}$ in Eq. (4): with a reasonable K-factor, $0 \leq \alpha_s^{\rm in} \leq 0.3$ is consistent with hadron production at RHIC both in $p+p$ and d+A collisions. Figure 10 shows the effect of varying $\alpha_s^{\rm in}$ in Eq. (4). For each value of η, results are shown both for $\alpha_s^{\rm in} = 0$ and variation within the range $0.09 \geq \alpha_s^{\rm in} \geq 0.3$. For $\eta = 0$ and 2, both $\alpha_s^{\rm in} = 0.1$ and 0.2 are shown. There is only a small difference at $\eta = 0$ while a larger difference can be seen at forward proton rapidity, especially for $N > 5$. With $\eta = 4$ and 6, only $\alpha_s^{\rm in} = 0.1$ is shown. Note that taking $\alpha_s^{\rm in} > 0$ changes the p_T slope considerably, as may be expected.

In order to quantify the uncertainties due to different initial nuclear saturation scales, in Fig. 10 $R_{pA}^{\rm ch}$ is shown for different initial saturation scales $Q_{0A}^2 = NQ_{0p}^2$ for $3 < N < 7$ with factorization scale $Q = p_T$. Unfortunately, $R_{pA}^{\rm ch}$ is very sensitive to Q_{0A}^2. However, by comparing to measurements of $R_{pA}^{\rm ch}$ at one rapidity, the predictions in Fig. 10 can be used to determine Q_{0A}^2 at that rapidity. Then, if the measured $R_{pA}^{\rm ch}$ at one rapidity lies between two lines labeled N_1 and N_2, the results at other rapidities should correspond to the same values of N and thus the same Q_{0A}^2. Only these results should be considered to be true CGC predictions. In this way, knowing $R_{pA}^{\rm ch}$ at one rapidity significantly reduces theoretical uncertainties associated with Q_{0A}^2 at other rapidities. Therefore, despite rather large theoretical uncertainties, it is still possible to test the main CGC/saturation dynamics at the LHC.

It is clear that CGC approaches predict more suppression at forward proton rapidities compared to collinear factorization.[116,117] Moreover, the small-x evolution washes away the Cronin-type peak at low p_T at all rapidities. Therefore, observation of a Cronin peak in p+Pb collisions at the LHC, regardless of whether it is accompanied by overall enhancement or suppression, can potentially be a signal of non-CGC physics since it is difficult to accommodate this feature in the current accuracy of the CGC approach.[20]

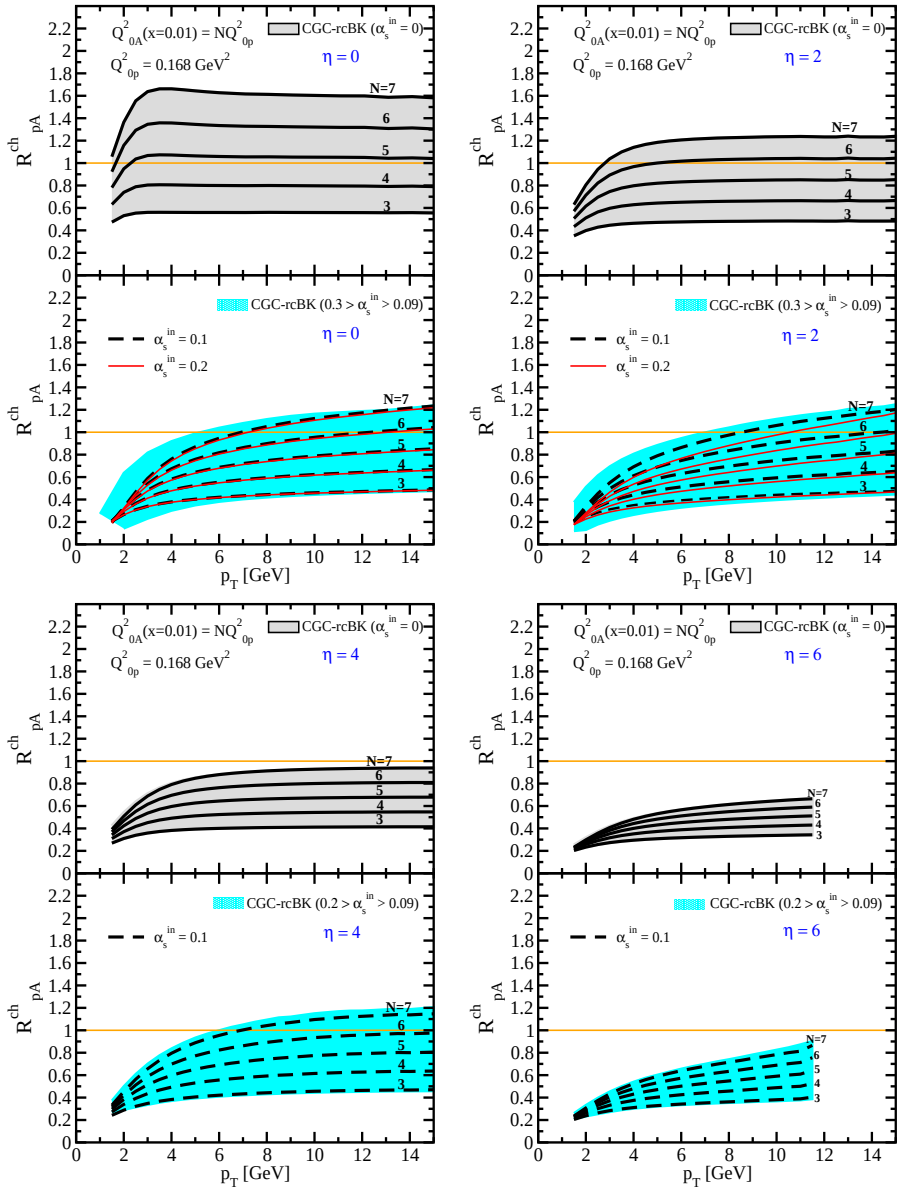

Fig. 10. The nuclear modification factor $R_{pA}^{\rm ch}$ for charged hadron production in minimum bias p+Pb collisions at $\eta = 0$, 2, 4, and 6 (with the convention that the proton beam moves toward forward rapidity) obtained from the hybrid factorization in Eq. (39) assuming different values of the saturation scale in the nucleus, Q_{0A}^2. The lines labeled by a given value of N, for $3 < N < 7$, are results with fixed factorization scale $\mu_F = p_T$ and fixed saturation scale $Q_{0A}^2 = NQ_{0p}^2$ and $Q_{0p}^2 = 0.168$ GeV$^2/c^2$. The bands shown the variation in the results with the choice of factorization scale. Two panels are shown for each rapidity. The upper panel shows results obtained by taking $\alpha_s^{in} = 0$ (assuming only elastic contribution) while the bottom panel shows the variation of $\alpha_s^{\rm in}$ in the range $0.09 \geq \alpha_s^{in} \geq 0.3$. In the bottom panels for $\eta = 0$ and 2, results with both $\alpha_s^{\rm in} = 0.1$ and 0.2 are shown, while for $\eta = 4$ and 6, only $\alpha_s^{\rm in} = 0.1$ is shown. The plots are taken from Ref.[20]

Albacete *et al* rcBK (J. Albacete, A. Dumitru, H. Fujii and Y. Nara) Figure 11 shows bands for $R_{pA}(p_T)$ at $\eta = 0$ and 2 with rcBK-MC. The upper edges of the bands are calculated with $\gamma = 1.119$ and KKP-LO fragmentation functions. the lower limit of the bands corresponds to the McLerran-Venugopalan initial condition ($\gamma = 1$) with DSS-NLO fragmentation functions, taken from Ref.[95]

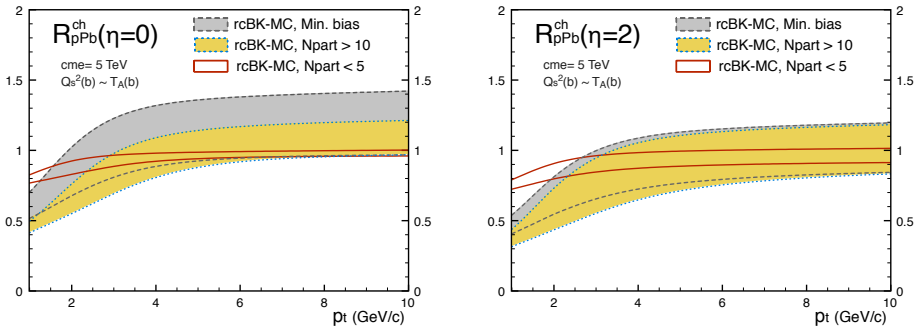

Fig. 11. The nuclear modification factor for three different centrality classes assuming k_T-factorization. The $\eta = 2$ result is obtained with the convention that the proton beam moves toward forward rapidity.

There is suppression of $R_{p\mathrm{Pb}}(p_T \sim 1\,\mathrm{GeV}/c) = 0.6 \pm 0.1$ at midrapidity. The ratio increases monotonically to $p_T \sim 3$ GeV/c where it flattens. There is no clear Cronin peak. For all unintegrated gluon densities, $R_{p\mathrm{Pb}}$ decreases with increasing rapidity. In addition to the minimum bias results, two separate centrality classes are also shown, a central bin, $N_{\mathrm{part}} > 10$, and the most peripheral bin, $N_{\mathrm{part}} < 5$. There is a stronger effect for the most central collisions, as expected, for low p_T at both $\eta = 0$ and 2. (Note that there is a smaller difference between minimum bias and the most central collisions at $\eta = 2$. The overall effect is very weak for the peripheral bin with suppression persisting only to $p_T \sim 2 - 3$ GeV/c. For more details, see Ref.[95]

Cold matter energy loss (Z.-B. Kang, I. Vitev and H. Xing) Figure 12 presents model predictions for $R_{p\mathrm{Pb}}(p_T)$ in minimum bias p+Pb collisions at $y = 0$ (top), $y = 2$ (middle), and $y = 4$ (bottom). The upper edge of the bands corresponds to the RHIC scattering parameters while The lower edge allows for a potential high-energy enhancement of the parameters.

The $y = 0$ results were already presented in Fig. 8. At large proton rapidity the CNM effects are all amplified due to the larger values of the proton momentum fraction x_2 (relevent for cold nuclear matter energy loss with the proton moving in the direction of forward rapidity), the smaller values of the nuclear momentum fraction x_1 (relevent for dynamical shadowing with the nucleus moving in the direction of backward rapidity) and more steeply-falling p_T spectra (relevent for the

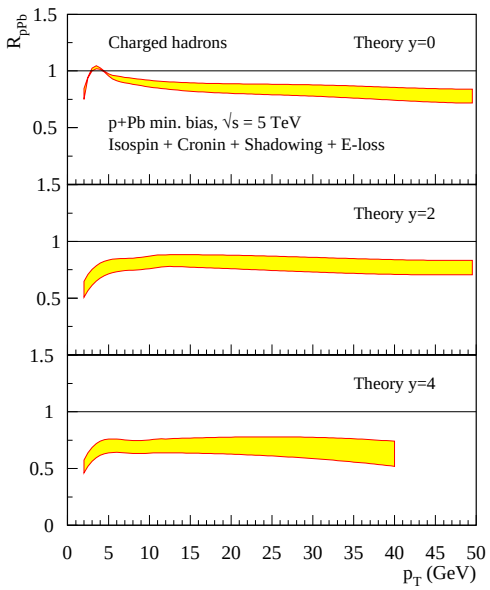

Fig. 12. Predictions for the nuclear modification factor R_{pPb} as a function of p_T for charged hadron production in minimum bias p+Pb collisions. Results are shown for three rapidities: $y = 0$ (top), $y = 2$ (center), and $y = 4$ (bottom) with the convention that the proton beam moves toward forward rapidity, see Ref.[67]

Cronin effect). As a result, at low p_T and large ion rapidity, dynamical shadowing can dominate and lead to stronger suppression of inclusive particle production (note the disappearance of the small Cronin enhancement at $y > 0$). At high p_T the suppression is a combined effect of cold nuclear matter energy loss and the Cronin effect. As will be seen later, the behavior of $R_{p\mathrm{Pb}}$ for π^0 and direct photon production is qualitatively similar to the $R_{p\mathrm{Pb}}$ dependence for charged hadrons shown here.

Away from midrapidity, these predictions suggest a stronger effect than that found with EPS09 parton shadowing alone. On the other hand, the effect shown here is weaker than the results using the rcBK-MC approach also shown in this section.

`AMPT` at $\eta \neq 0$ (Z. Lin) Figure 13 shows results with the `AMPT` − `def` calculation in minimum bias p+Pb collisions at five different η values. At $\eta = 4$, the ratio is larger than at lower rapidities. The ratios are very similar for $\eta = 0$ and 2. The backward rapidity results have lower values of $R_{p\mathrm{Pb}}$. While the ratios are indepedent of p_T within the uncertainties for $\eta = -2$, 0 and 2, the ratios increase with p_T for $\eta = 4$ and -4 with the largest increase for $\eta = -4$.

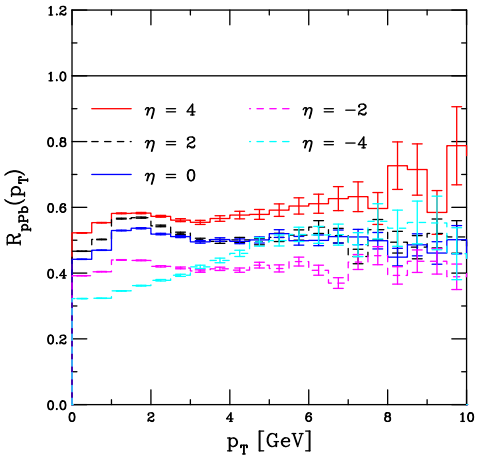

Fig. 13. Predictions for the nuclear modification factor R_{pPb} as a function of p_T for charged hadron production in minimum bias p+Pb collisions for $\eta = -4$, -2, 0, 2 and 4 calculated using `AMPT − def`.

3.3.4. *Forward-backward asymmetry(G. G. Barnaföldi, J.Barette, M. Gyulassy, P. Levai, G. Papp, M. Petrovici, V. Topor Pop, Z. Lin and R. Vogt)*

One method of determining the difference between the proton and lead rapidity regions is studying the forward-backward asymmetry in charged hadron production, given by

$$Y^h_{\rm asym}(p_T) = \frac{E_h d^3\sigma^h_{p\rm Pb}/d^2p_T d\eta|_{\eta>0}}{E_h d^3\sigma^h_{p\rm Pb}/d^2p_T d\eta|_{\eta<0}} , \\ = \frac{R^h_{p\rm Pb}(p_T, \eta > 0)}{R^h_{p\rm Pb}(p_T, \eta < 0)} . \quad (42)$$

where the 'forward' direction, $\eta > 0$, is that of the lead beam, toward positive rapidity while the 'backward' direction, $\eta < 0$ is that of the proton beam, toward negative rapidity.

The asymmetries, calculated in the center of mass frame in the range $0.3 < |\eta| < 0.8$,[108] both for standard shadowing and event generators, are shown in Fig. 14. Two calculations of the forward-backward asymmetry in p+Pb collisions are shown. The first result is in the `kTpQCD_v2.0` approach with several standard shadowing parameterizations. The second is obtained with `AMPT`.

Results with `kTpQCD_v2.0` including the `HIJING2.0`,[47] EKS98,[92] EPS08,[93] and HKN[94] shadowing parameterizations are presented. Since the EKS98, EPS08 and HKN parameterizations are independent of impact parameter, there is no difference between minimum bias results and results with a centrality cut. Thus, these are

all labeled MB for minimum bias. With the HKN parameterization, $Y_{\rm asym} \approx 1$ independent of p_T. The EKS98 and EPS08 parameterizations, producing identical ratios, predict a small enhancement, $Y_{\rm asym} > 1$.

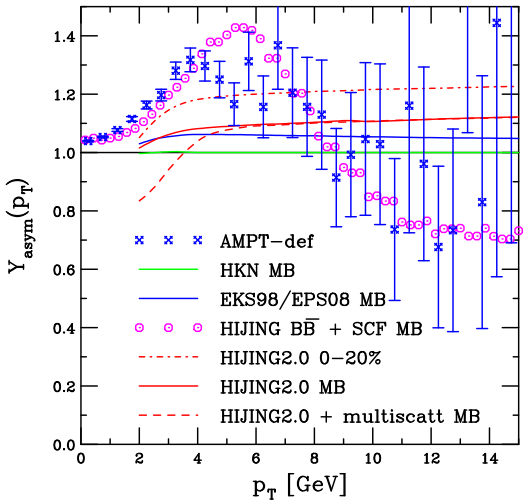

Fig. 14. Predictions for the forward-backward asymmetry, $Y^h_{\rm asym}(p_T)$, from Refs.[110,111] Centrality independent results are shown for the HKN, EKS98 and EPS08 parameterizations (labeled MB). Minimum bias results are also shown for `HIJINGBB̄2.0` and `HIJING2.0` with multiple scattering. In addition, `HIJING2.0` results in MB collisions and for the 20% most central collisions (using the parameter s_a in Eq. (22)) are also shown. The blue points are the `AMPT − def` results.

Results with the `HIJING2.0` shadowing parameterization with and without multiple scattering differ for $p_T < 5$ GeV/c but converge at higher p_T. When the collision centrality is taken into account, the forward-backward asymmetry is enhanced by the centrality cut alone. Chaning the strength of low x shadowing, as in Eq. (22), does not change the shape of $Y_{\rm asym}(p_T)$ for $p_T > 5$ GeV/c.

Finally, results for the minimum bias asymmetry is also shown for `HIJINGBB̄2.0`.[53] These calculations include both shadowing and strong color field effects (indicated "+ SCF"). Here the ratio rises from near unity at $p_T \sim 0$ to a peak at $p_T \sim 5.5$ GeV/c. It then decreases to $Y_{\rm asym} \sim 0.75$ for $p_T \geq 10$ GeV/c.

The forward-backward asymmetry of $R_{p\rm Pb}$, calculated in the center of mass frame with `AMPT − def` in the range $0.3 < |\eta| < 0.8$, is shown by the blue points in Fig. 14 for charged particles in minimum-bias events with simulations employing `AMPT − def`. The initial enhancement first increases with p_T and then decreases. Although the statistical errors become very large above $p_T \sim 10$ GeV/c, it is clear that the result is similar to the general behavior of the `HIJINGBB̄2.0` result.

The low p_T enhancement may arise because the asymmetry in $dN/d\eta$ in p+Pb relative to $p + p$ in the lead direction (positive rapidity) introduces a natural en-

hancement in $R_{p\mathrm{Pb}}$ in the forward direction. The enhanced particle production in p+Pb is most likely at low p_T, see e.g. Fig. 13.

The `AMPT − def` results include the impact-parameter dependent nuclear shadowing parameterization implemented in `HIJING1.0`. Therefore the asymmetry at other centralities would differ from that in minimum-bias events.

3.3.5. $R_{p\mathrm{Pb}}(\eta)$ *(G. G. Barnaföldi, J. Barette, M. Gyulassy, P. Levai, M. Petrovici and V. Topor Pop)*

Finally, we end this section with the predicted ratio $R_{p\mathrm{Pb}}$ as a function of pseudorapidity in `HIJINGBB̄2.0`. As discussed previously, increasing the minijet cutoff parameter p_0 from 2 GeV/c in $p+p$ collisions to 3.1 GeV/c in p+Pb causes a slow growth in the per nucleon multiplicity which could be interpreted as evidence for gluon saturation. It is difficult to directly relate p_0 to the saturation scale Q_s because in `HIJING` hadronization proceeds through longitudinal string fragmentation. The low p_T part of the minijet spectrum is particularly sensitive to the $\sqrt{s_{NN}}$ and A dependence of minijet suppression while the $p_T > 5$ GeV/c minijet tails are unaffected. The energy and A dependence of the string tension arises from strong color field (color rope) effects not included in CGC phenomenology that assumes hadronization by k_T-factorized gluon fusion.

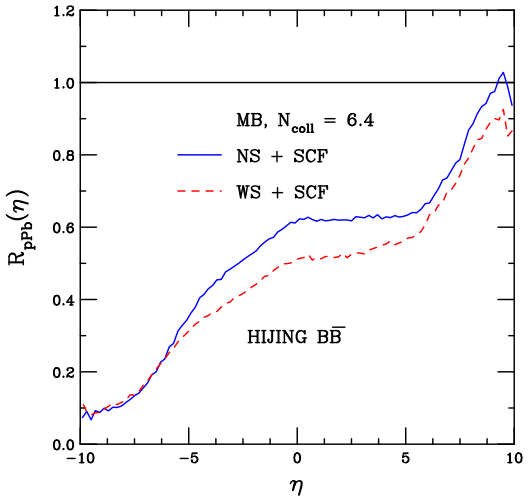

Fig. 15. The suppression factor $R_{p\mathrm{Pb}}$ as a function of pseudorapidity, η, for `HIJINGBB̄2.0` with strong color field effects, without (solid) and with (dashed) shadowing.

`HIJING` minijet hadronization does not proceed by independent fragmentation, as in `PYTHIA`,[59] but through string fragmentation with gluon minijets represented as kinks in the strings. The interplay between longitudinal string fragmentation

dynamics and minijets is a nonperturbative feature of HIJING-type models. The effect of string fragmentation on the multiplicity is manifested in the behavior of $R_{p\mathrm{Pb}}(\eta)$ in the fragmentation regions $|\eta| > 5$. In the nuclear beam fragmentation region, the ratio is approximately linearly increasing from $\eta = 5$ to the kinematic limit. There is an approximate plateau in the ratio over $0 < \eta < 5$, followed by a decrease toward the value $1/N_{\mathrm{coll}}$ in the proton fragmentation region, a Glauber geometric effect first explained in Refs.[118,119] and a feature of string fragmentation in HIJING.

4. Identified Particles

4.1. AMPT *(Z. Lin)*

Some representative AMPT results for identified particles are shown here. The rapidity distributions for K^+ and K^- production in the default and string melting versions are shown in Fig. 16. The default and string melting versions of the rapidity distributions of protons and antiprotons are shown in Fig. 17.

There are differences between the default and string melting versions, even in $p+p$ collisions. However, these differences are typically small. Note that the bump at midrapidity in the proton and antiproton rapidity distributions in the string-melting version is likely a result of the simple quark coalescence model implemented in AMPT (see e.g. Fig. 38 of Ref.[65]).

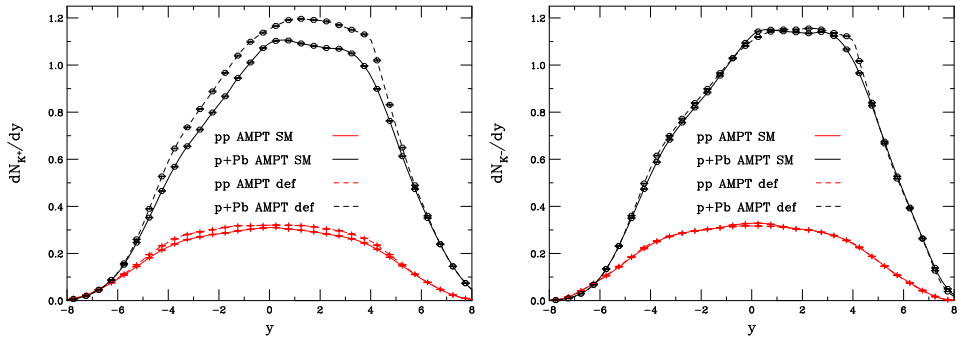

Fig. 16. Rapidity distribution, dN/dy, of K^+ (left) and K^- (right) mesons.

The left-hand side of Fig. 18 shows $R_{p\mathrm{Pb}}$ for protons, antiprotons, neutral pions and charged particles. The identified particles are shown for $y = 0$ while the charged particle ratio is for $\eta = 0$. The ratios are all very similar except for protons which grows almost linearly with p_T.

The right-hand side of Fig. 18 presents results for the suppression factor for charged particles within $|\eta| < 1$ in three centrality bins: minimum bias; the 10% most central collisions; and a peripheral bin, the $60 - 80\%$ most central collisions.

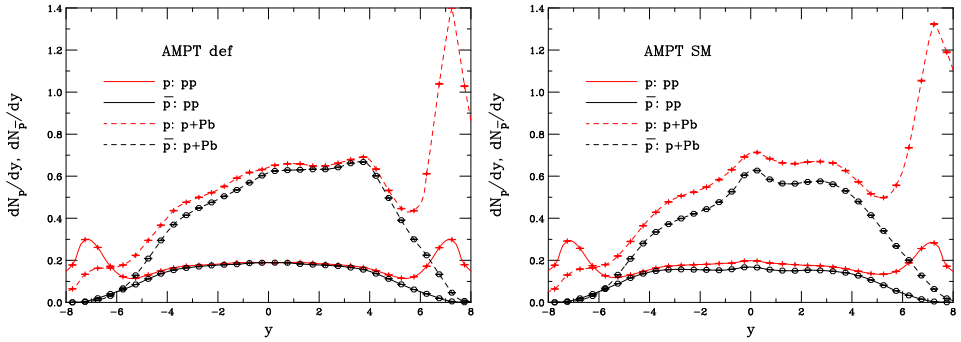

Fig. 17. Rapidity distribution, dN/dy, of and p and $\overline{p}$ in the default (left) and SM (right) scenarios.

Interestingly, the ratio is smallest and decreasing with p_T for the more peripheral bin while the largest value of $R_{p\mathrm{Pb}}$ is the most central bin.

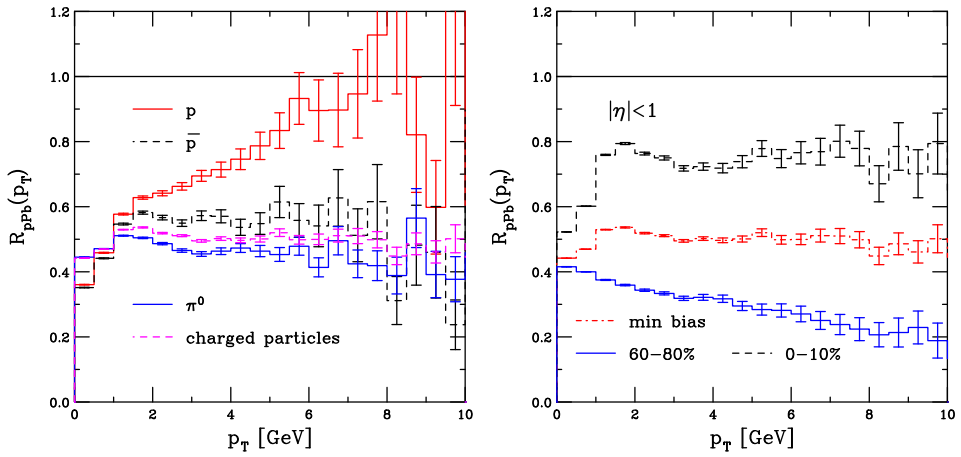

Fig. 18. (Left) The minimum bias results at $y = 0$ for π^0, p and $\overline{p}$ are shown with the charged hadron ratio for $\eta = 0$. All results are calculated with `AMPT − def`. (Right) The charged hadron results at midrapidity, $|\eta| < 1$, are shown for minimum bias collisions as well as in two centrality bins: the 10% most central and the 60-80% most central. All results are calculated employing `AMPT − def`.

4.2. *Centrality dependent* $R^{\pi^0}_{p\mathrm{Pb}}(p_T, y = 0)$ *with EPS09s nPDFs (I. Helenius and K. J. Eskola)*

Predictions of the centrality dependence of π^0 production at midrapidty are presented here. Two spatially-dependent nuclear PDF (nPDF) sets, EPS09s and

EKS98s were determined in Ref.[120] The key component is a power series ansatz of the nuclear thickness function ($T_A(\vec{s})$) for the spatial dependence of the nPDF modifications,

$$r_i^A(x,Q^2,\vec{s}) = 1 + \sum_{j=1}^{n} c_j^i(x,Q^2)\,[T_A(\vec{s})]^j \quad . \tag{43}$$

The A dependence of the earlier global nPDF fits EPS09[48] and EKS98[92] was exploited to obtain the values of the A-independent coefficients $c_j^i(x,Q^2)$. It was found that $n = 4$ is sufficient for reproducing the A systematics of the globally-fitted nPDFs.

Predictions are presented for the nuclear modification factor $R_{p\mathrm{Pb}}^{\pi^0}$ of inclusive neutral pion production at the LHC using the new EPS09s NLO nPDF set. As in Ref.,[120] the centrality classes are defined in terms of impact parameter intervals. For a given centrality class, $R_{p\mathrm{Pb}}^{\pi^0}$ is defined as

$$R_{p\mathrm{Pb}}^{\pi^0}(p_T,y;b_1,b_2) \equiv \frac{\left\langle \dfrac{d^2N_{p\mathrm{Pb}}^{\pi^0}}{dp_T dy} \right\rangle_{b_1,b_2}}{\dfrac{\langle N_{\mathrm{coll}}^{p\mathrm{Pb}}\rangle_{b_1,b_2}}{\sigma_{\mathrm{in}}^{NN}} \dfrac{d^2\sigma_{pp}^{\pi^0}}{dp_T dy}} = \frac{\int_{b_1}^{b_2} d^2\vec{b} \dfrac{d^2N_{p\mathrm{Pb}}^{\pi^0}(\vec{b})}{dp_T dy}}{\int_{b_1}^{b_2} d^2\vec{b}\, T_{p\mathrm{Pb}}(\vec{b}) \dfrac{d^2\sigma_{pp}^{\pi^0}}{dp_T dy}}, \tag{44}$$

where the impact parameter limits b_1 and b_2 are calculated from the optical Glauber model. The proton is assumed to be point-like, i.e. $T_{p\mathrm{Pb}}(\vec{b}) = T_{\mathrm{Pb}}(\vec{b})$. The minimum bias ratio $R_{p\mathrm{Pb}}^{\pi^0}$ is obtained with $b_1 = 0$ and $b_2 \to \infty$. The cross sections are calculated in NLO using the `INCNLO` package[ii][84] with the CTEQ6M proton PDFs[69] along with three different fragmentation functions: KKP;[42] AKK;[121] and fDSS.[70] The uncertainty band reflecting the nPDF uncertainties is calculated using the error sets of EPS09s with the fDSS fragmentation functions according to the prescription described in the original EPS09 paper.[48]

In Fig. 19 the minimum bias $R_{p\mathrm{Pb}}^{\pi^0}$ is shown as a function of p_T at midrapidity ($y = 0$) in the nucleon-nucleon center-of-mass frame. Both logarithmic and linear p_T scales are shown. In the region $p_T < 10$ GeV/c a suppression due to small-x shadowing in the nPDFs is observed while at $10 < p_T < 200$ GeV/c there is a small enchancement due to the antishadowing. Even though the different fragmentation functions may yield different absolute cross sections, these differences cancel in the ratio $R_{p\mathrm{Pb}}^{\pi^0}$.

In Fig. 20 $R_{p\mathrm{Pb}}^{\pi^0}$ is presented in four different centrality classes, $(0-20)$ %, $(20-40)$ %, $(40-60)$ % and $(60-80)$ %. The impact parameter limits for these centrality classes can be found in Ref.[120] For comparison, the minimum bias results are also shown. Slightly larger nuclear effects are observed in the most central collisions than in the minimum bias collisions. Nuclear effects in the most peripheral collisions are about a factor of two smaller than those in the most central collisions.

[ii] http://lapth.in2p3.fr/PHOX_FAMILY/readme_inc.html

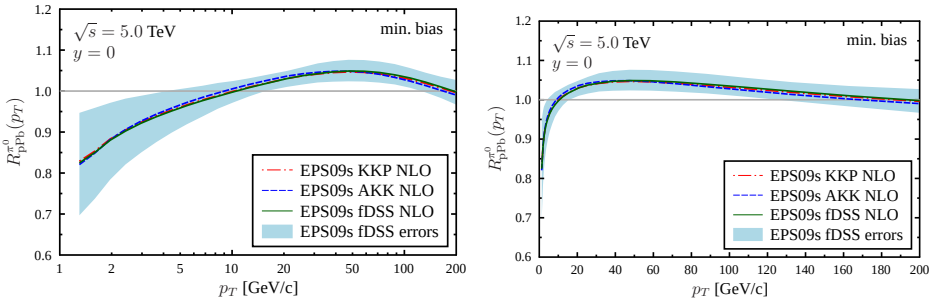

Fig. 19. The nuclear modification factor for inclusive π^0 production in p+Pb collisions at $y = 0$ for minimum bias collisions calculated with the EPS09s NLO nPDFs, plotted on logarithmic (left) and linear (right) p_T scales. The blue error band is calculated employing the EPS09s error sets. All scales are fixed to the pion p_T. Based on Ref.[120]

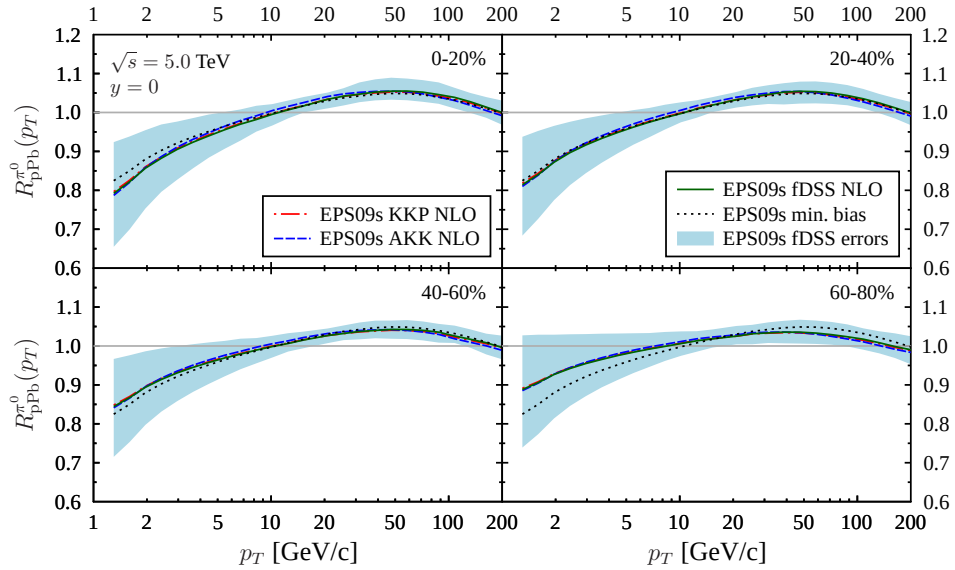

Fig. 20. The nuclear modification factor for inclusive π^0 production in p+Pb collisions at $y = 0$ in four centrality classes calculated with the EPS09s NLO nPDFs. The blue error band is calculated employing the EPS09s error sets. All scales are fixed to the pion p_T. For comparison, the minimum bias result is also shown. Based on Ref.[120]

4.3. *Cold matter effects with energy loss (Z.-B.Kang, I. Vitev and H. Xing)*

The predictions for $R^{\pi^0}_{p\rm Pb}$, like those for charged hadrons shown in Fig. 12 are based on perturbative QCD factorization. Cold nuclear matter effects are implemented separately. The advantage of this approach is that all CNM effects have a clear

physical origin, generally centered around multiple parton scattering. The implementation of these calculable CNM effects is well documented, see Sec. 2.6. Isospin effects, the Cronin effect, cold nuclear matter energy loss, and dynamical shadowing are all included.

The neutral pion results in Fig. 21 are rather similar to those shown in Fig. 12. The upper edges of the bands at $y = 0$ (top), $y = 2$ (middle), and $y = 4$ (bottom) correspond to the RHIC scattering parameters while the lower edges correspond to potential enhancement of these parameters.

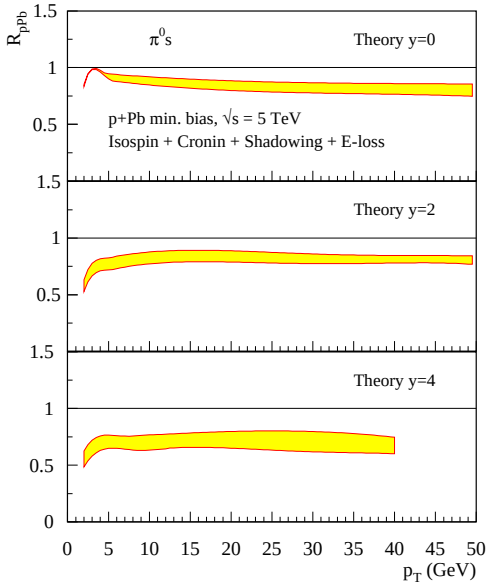

Fig. 21. Predictions for the nuclear modification factor $R^{\pi^0}_{p\mathrm{Pb}}(p_T)$ as a function in minimum bias collisions at $\sqrt{s_{NN}} = 5$ TeV. Results for three rapidities: $y = 0$ (top), $y = 2$ (middle), and $y = 4$ (bottom) are shown. The calculations have been made with the convention that the proton beam moves toward forward rapidity, see Ref.[67]

As seen by comparison with the EPS09 minimum bias results for $y = 0$ in Fig. 19, the combined effects included here are stronger than with shadowing alone. Antishadowing in EPS09 produces a ratio larger than unity for $10 < p_T < 200$ GeV/c while the ratio is smaller than unity over the entire range calculated here ($p_T < 50$ GeV/c).

5. Quarkonium (R. Vogt)

The predictions for the J/ψ suppression factor, considering only shadowing effects on the parton densities are described in this section. There are a number of possible cold matter effects on J/ψ production, including modifications of the parton

densities in nuclei (shadowing); breakup of the quarkonium state due to inelastic interactions with nucleons (absorption); and energy loss in cold matter. Since the quarkonium absorption cross section decreases with center-of-mass energy, we can expect that shadowing is the most important cold matter effect at midrapidity, see Refs.[122,123] Here we show results for the rapidity and p_T dependence of shadowing at $\sqrt{s_{NN}} = 200$ GeV for d+Au collisions at RHIC and the rapidity dependence at $\sqrt{s_{NN}} = 5$ TeV p+Pb collisions, neglecting absorption.

The results are obtained in the color evaporation model (CEM) at next-to-leading order in the total cross section. In the CEM, the quarkonium production cross section is some fraction, F_C, of all $Q\overline{Q}$ pairs below the $H\overline{H}$ threshold where H is the lowest mass heavy-flavor hadron,

$$\sigma_C^{\rm CEM}(s) = F_C \sum_{i,j} \int_{4m^2}^{4m_H^2} ds \int dx_1\, dx_2\; f_i^p(x_1,\mu_F^2)\; f_j^p(x_2,\mu_F^2)\; \hat{\sigma}_{ij}(\hat{s},\mu_F^2,\mu_R^2) \;, \quad (45)$$

where $ij = q\overline{q}$ or gg and $\hat{\sigma}_{ij}(\hat{s})$ is the $ij \to Q\overline{Q}$ subprocess cross section. The normalization factor F_C is fit to the forward (integrated over $x_F > 0$) J/ψ cross section data on only p, Be, Li, C, and Si targets. In this way, uncertainties due to ignoring any cold nuclear matter effects which are on the order of a few percent in light targets are avoided. The fits are restricted to the forward cross sections only.

The same values of the central charm quark mass and scale parameters are employed as those found for open charm, $m = 1.27 \pm 0.09$ GeV/c^2, $\mu_F/m = 2.10^{+2.55}_{-0.85}$, and $\mu_R/m = 1.60^{+0.11}_{-0.12}$.[124] The normalization F_C is obtained for the central set, $(m, \mu_F/m, \mu_R/m) = (1.27\,\text{GeV}, 2.1, 1.6)$. The calculations for the extent of the mass and scale uncertainties are multiplied by the same value of F_C to obtain the extent of the J/ψ uncertainty band.[124] The results shown here are not the same as those calculated at leading order[125] because the LO and NLO gluon shadowing parameterizations differ significantly at low x.[48]

Figure 22 shows the uncertainty in the shadowing effect due to uncertainties in the EPS09 shadowing parameterization[48] (red) as well as those due to the mass and scale uncertainties obtained in the fit to the total charm cross section (blue) calculated with the EPS09 central set. All the calculations are NLO in the total cross section and assume that the intrinsic k_T broadening is the same in $p+p$ as in p+Pb. Note that the rapidity-dependent ratios are adjusted so that the lead nucleus moves toward negative rapidity and the small x region of the nucleus is at large negative rapidity, as is the case for pseudorapidity distributions and the rapidity-dependent ratios shown previously.

The mass and scale uncertainties are calculated based on results using the one standard deviation uncertainties on the quark mass and scale parameters. If the central, upper and lower limits of $\mu_{R,F}/m$ are denoted as C, H, and L respectively, then the seven sets corresponding to the scale uncertainty are $\{(\mu_F/m, \mu_F/m)\} = \{(C,C), (H,H), (L,L), (C,L), (L,C), (C,H), (H,C)\}$. The uncertainty band can be obtained for the best fit sets by adding the uncertainties from the mass and scale

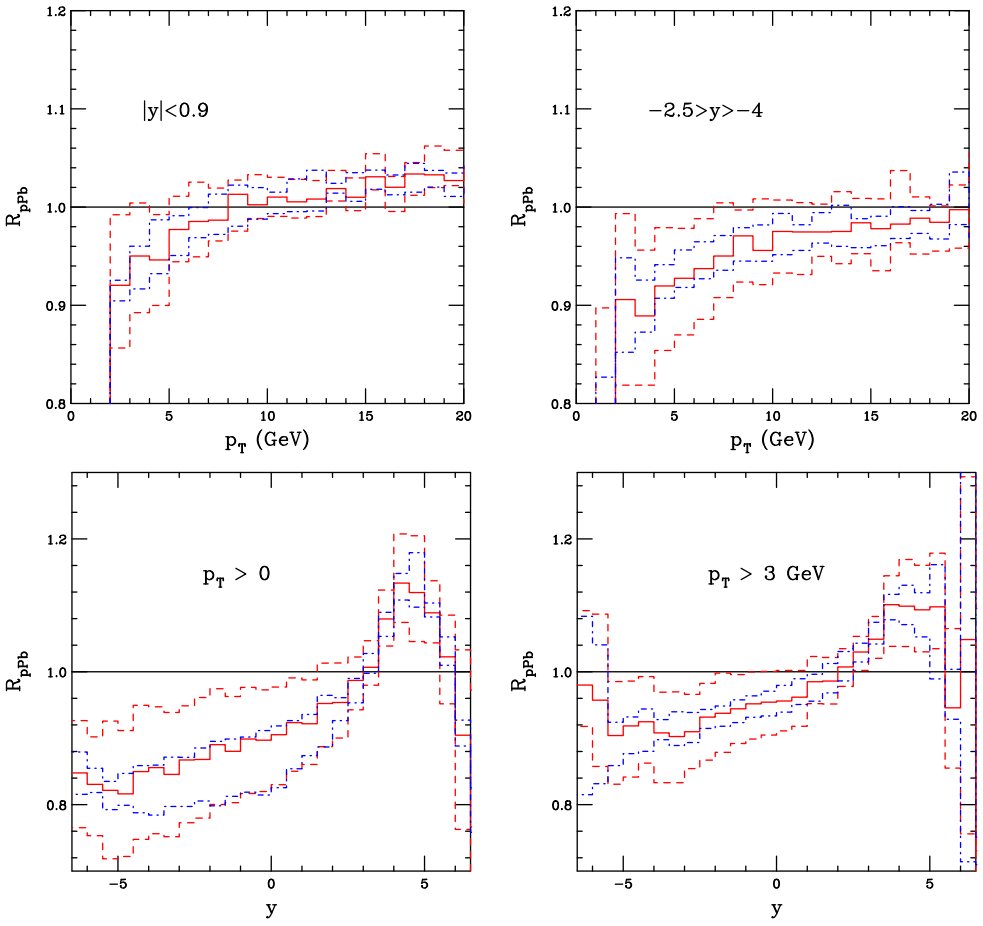

Fig. 22. The ratio $R_{\rm dAu}$ (left) and $R_{\rm AuAu}$ (right) at $\sqrt{s} = 5$ TeV. The dashed red histogram shows the EPS09 uncertainties while the dot-dashed blue histogram shows the dependence on mass and scale. The $p + p$ denominator is also calculated at 5 TeV and does not include any rapidity shift in p+Pb collisions. For a discussion about normalizing the results to $p + p$ collisions at different energies, see Ref.[125]

variations in quadrature. The envelope containing the resulting curves,

$$\sigma_{\rm max} = \sigma_{\rm cent} + \sqrt{(\sigma_{\mu,\rm max} - \sigma_{\rm cent})^2 + (\sigma_{m,\rm max} - \sigma_{\rm cent})^2}\ , \tag{46}$$

$$\sigma_{\rm min} = \sigma_{\rm cent} - \sqrt{(\sigma_{\mu,\rm min} - \sigma_{\rm cent})^2 + (\sigma_{m,\rm min} - \sigma_{\rm cent})^2}\ , \tag{47}$$

defines the uncertainty. The EPS09 band is obtained by calculating the deviations from the central value for the 15 parameter variations on either side of the central set and adding them in quadrature. With the new uncertainties on the charm cross section, the band obtained with the mass and scale variation is narrower than that

with the EPS09 variations.

6. Photons

Photons are ideal probes in heavy ion collisions due to their lack of final-state interactions with either a quark-gluon plasma or a hot hadron gas. Baseline measurements in $p + p$ and p+Pb collisions are very important to subtract photons from hard initial parton scatterings which are unrelated to QGP and, in particular, to determine cold nuclear matter effects on photon production. Measured nuclear modification factors for photons at high transverse momenta ($p_T > 5$ GeV/c) measured in Pb+Pb collisions at the LHC and Au+Au collisions at RHIC, $R_{AA} \approx 1$, have demonstrated that hard processes scale with the number of binary nucleon-nucleon collisions in nucleus-nucleus collisions. An especially important question for heavy-ion physics at the LHC is the magnitude of low-x effects on the parton densities, particularly for gluons. The presence of shadowing, *i.e.* suppression of the number of low-x partons, has a significant effect on benchmarking hard processes at intermediate p_T. Direct photons and other electromagnetic probes are in particular needed for a quantitatively precise determination of the nuclear parton distributions.

This section includes an NLO calculation of direct photon production in $p + p$ and p+Pb collisions; LO calculations of cold matter effects on photon production at several rapidities; saturation effects on direct and inclusive prompt photon production and photon-hadron correlations; and a discussion on gluon saturation and shadowing in dilepton and photon production.

6.1. *Direct photon cross sections (R. J. Fries and S. De)*

Predictions of the p_T and y dependence of direct photon production are given here. The impact-parameter averaged EPS09 shadowing parameterizations[48] are used with the CTEQ6.6 parton densities[126] to calculate results in minimum bias p+Pb collisions. These calculations can thus be employed to check the validity of the EPS09 modifications. The per nucleon cross sections given here can be directly compared to the minimum bias p+Pb data by converting the cross sections to differential yields scaling the results by $\sigma_{\rm in} = 67$ mb and the average number of NN collisions in a given centrality bin.

These NLO in α_s calculations are performed with `JETPHOX1.3.1`.[127,128] Hard prompt photons and fragmentation photons (obtained with the BFG-II fragmentation functions[129]) are both included. An isolation cut of $E_{T,\rm hadron} < 5$ GeV on hadronic energy is imposed within a $R = 0.4$ isolation cone around the photon, similar to the CMS analysis method for $p + p$ collisions at 7 TeV.

Figure 23 shows the rapidity dependence, $d\sigma/dy$, of direct photon production in $p + p$ and p+Pb collisions, normalized per nucleon. A p_T cut, $p_T > 4$ GeV/c is imposed. The results are presented in the lab frame. Recall that there is a difference, $\Delta y = 0.465$, between the center-of-mass and lab frames at the current energy.

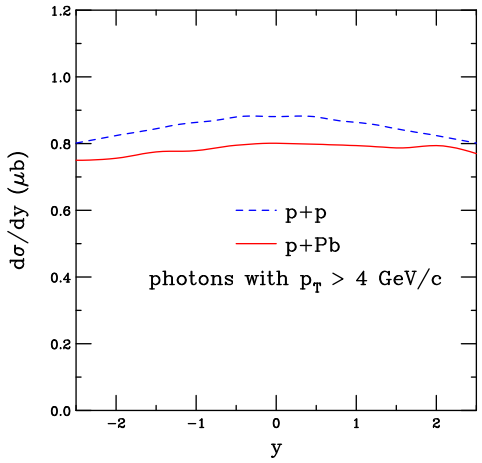

Fig. 23. The direct photon cross section, $d\sigma/dy$, as a function of rapidity in the laboratory frame for photons with $p_T > 4$ GeV/c and an isolation cut $E_{T,\mathrm{hadron}} < 5$ GeV. Both $p+p$ and p+Pb results are shown. The p+Pb results are normalized to the per nucleon cross section.

On the left-hand side of Fig. 24, the p_T spectrum at $y = 0$, $d\sigma/d^2p_T dy$, is shown for $p+p$ and p+Pb collisions. The $p+p$ result is scaled down by a factor of 100 to separate the two curves. The corresponding nuclear modification factor is shown on the right-hand side. Note that a logarithmic scale is used on the x-axis here to highlight the modification of the low p_T part of the photon spectrum.

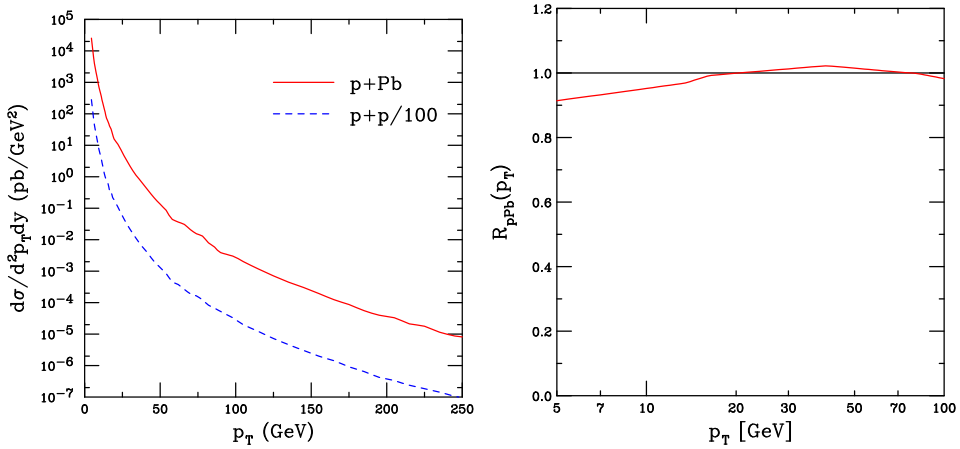

Fig. 24. (Left) The direct photon p_T distribution at $y = 0$ in the lab frame. The p+p distribution is scaled down by two orders of magnitude. (Right) The corresponding modification factor $R_{p\mathrm{Pb}}(p_T)$. Note the logarithmic p_T scale.

6.2. *Cold matter effects on photon production (Z.-B. Kang, I. Vitev and H. Xing)*

Prompt photon production in $p + p$ collisions has two components, the direct and fragmentation contributions:[68]

$$\frac{d\sigma}{dyd^2p_T} = \frac{d\sigma_{\rm dir}}{dyd^2p_T} + \frac{d\sigma_{\rm frag}}{dyd^2p_T}. \tag{48}$$

The fragmentation contribution is given by:

$$\frac{d\sigma_{\rm frag}}{dyd^2p_T} = K\frac{\alpha_s^2}{s}\sum_{a,b,c}\int\frac{dx_1}{x_1}d^2k_{T_1}\, f_{a/N}(x_1,k_{T_1}^2)\int\frac{dx_2}{x_2}d^2k_{T_2}\, f_{b/N}(x_2,k_{T_2}^2) \times\int\frac{dz_c}{z_c^2}\, D_{\gamma/c}(z_c)H_{ab\to c}(\hat{s},\hat{t},\hat{u})\delta(\hat{s}+\hat{t}+\hat{u}). \tag{49}$$

The expression is exactly the same as Eq. (23) if the parton-to-hadron fragmentation function, $D_{h/c}(z_c)$, is replaced by the parton-to-photon fragmentation function, $D_{\gamma/c}(z_c)$. The direct contribution can be written as:

$$\frac{d\sigma_{\rm dir}}{dyd^2p_T} = K\frac{\alpha_{\rm em}\alpha_s}{s}\sum_{a,b}\int\frac{dx_1}{x_1}d^2k_{T_1}f_{a/N}(x_1,k_{T_1}^2)\int\frac{dx_2}{x_2}d^2k_{T_2}f_{b/N}(x_2,k_{T_2}^2) \times H_{ab\to\gamma}(\hat{s},\hat{t},\hat{u})\delta\left(\hat{s}+\hat{t}+\hat{u}\right), \tag{50}$$

where $H_{ab\to\gamma}$ are the partonic hard-scattering functions for direct photon production.[68,130]

In $p+p$ collisions, $\langle k_T^2\rangle_{pp} = 1.8$ GeV$^2/c^2$, along with a K factor of $\mathcal{O}(1)$, which gives a good description of production at RHIC and LHC energies. The CTEQ6L1 PDFs[69] are employed with the GRV parametrization for parton-to-photon fragmentation functions.[131] The factorization and renormalization scales are fixed to the transverse momentum of the produced photon, $\mu_F = \mu_R = p_T$.

The results shown here are calculated employing the same cold matter effects described in Sec. 2.6. Figure 25 presents predictions for the nuclear modification factor in prompt photon production as a function of p_T for $y = 0$ (top), $y = 2$ (middle), and $y = 4$ (bottom). The upper edge of the bands corresponds to the RHIC scattering parameters The lower edge represents a high-energy enhancement of the parameters. The behavior of R_{pPb} for direct photons is qualitatively the same as the π^0s and charged hadron results shown earlier.

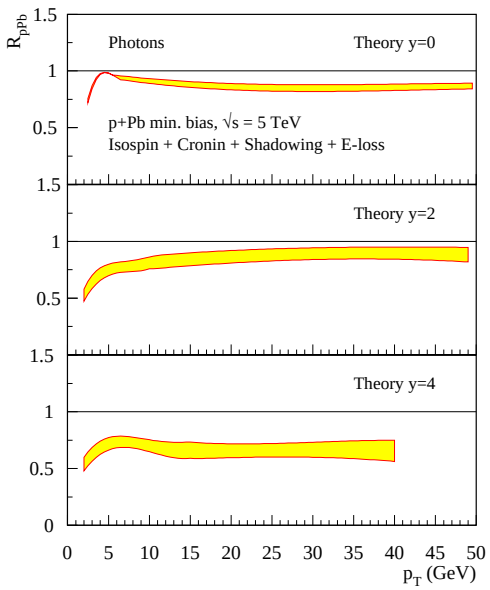

Fig. 25. Predictions of the nuclear modification factor $R_{p\mathrm{Pb}}$ as a function of p_T for prompt photon production in minimum bias p+Pb collisions for $y = 0$ (top), $y = 2$ (middle), and $y = 4$ (bottom), see Ref.[67]

6.3. *rcBK calculation of photon production (A. Rezaeian)*

The cross section for semi-inclusive prompt photon-quark production in $p + A$ collisions at leading twist in the CGC formalism is,[132,133]

$$\frac{d\sigma^{q\,A\to q(l)\,\gamma(p^\gamma)\,X}}{d^2\vec{b}_T\,d^2\vec{p_T}^{\,\gamma}\,d^2\vec{l_T}\,d\eta_\gamma\,d\eta_h} = \frac{K e_q^2\,\alpha_{\mathrm{em}}}{\sqrt{2}(4\pi^4)}\,\frac{p^-}{(p_T^\gamma)^2\sqrt{s}}\,\frac{1+(l^-/k^-)^2}{[p^-\,\vec{l_T}-l^-\vec{p_T}^{\,\gamma}]^2}$$
$$\times\delta\left[x_q-\frac{l_T}{\sqrt{s}}e^{\eta_h}-\frac{p_T^\gamma}{\sqrt{s}}e^{\eta_\gamma}\right]\,[2l^-p^-\,\vec{l_T}\cdot\vec{p_T}^{\,\gamma}+p^-(k^--p^-)\,l_T^2+l^-(k^--l^-)\,(p_T^\gamma)^2]$$
$$\times N_F(|\vec{l_T}+\vec{p_T}^{\,\gamma}|,x_g)\,, \qquad (51)$$

where p^γ, l, and k are the 4-momenta of the produced prompt photon, the outgoing q ($\overline{q}$) and the incident q ($\overline{q}$), respectively. A K factor was introduced to absorb higher-order corrections. The light-cone fraction x_q is the ratio of the incoming quark and proton energies, $x_q = k^-/\sqrt{s/2}$. The pseudorapidities of the outgoing prompt photon, η_γ, and quark, η_h, are defined as $p^- = (p_T^\gamma/\sqrt{2})e^{\eta_\gamma}$ and $l^- = (l_T/\sqrt{2})e^{\eta_h}$. The angle between the final-state quark and the prompt photon, $\Delta\phi$, is defined as $\cos(\Delta\phi) \equiv (\vec{l_T}\cdot\vec{p_T^\gamma})/(l_T p_T^\gamma)$. Only high p_T light hadron production is considered here. Therefore rapidity and pseudorapidity are equivalent. The semi-inclusive photon-hadron production cross section in proton-nucleus collisions can be obtained by convoluting the partonic cross section, Eq. (51), with the quark

distribution functions of the proton and the quark-hadron fragmentation function,

$$\frac{d\sigma^{p\,A\to h(p^h)\,\gamma(p^\gamma)\,X}}{d^2\vec{b}_T\,d^2\vec{p}_T^{\,\gamma}\,d^2\vec{p}_T^{\,h}\,d\eta_\gamma\,d\eta_h} = \int_{z_f^{\min}}^1 \frac{dz_f}{z_f^2}\int dx_q\, f_q(x_q,Q^2)\frac{d\sigma^{q\,A\to q(l)\,\gamma(p^\gamma)\,X}}{d^2\vec{b}_T\,d^2\vec{p}_T^{\,\gamma}\,d^2\vec{l}_T\,d\eta_\gamma\,d\eta_h} D_{h/q}(z_f,Q^2)\,,$$

where p_T^h is the transverse momentum of the produced hadron. The sum over quark and antiquark flavors in Eq. (52) is implied. The light-cone momentum fractions x_q, $x_{\bar{q}}$, and x_g in Eqs. (51) and (52) are related to the transverse momenta and rapidities of the produced hadron and prompt photon,[134]

$$x_q = x_{\bar{q}} = \tfrac{1}{\sqrt{s}}\left(p_T^\gamma\, e^{\eta_\gamma} + \tfrac{p_T^h}{z_f}\, e^{\eta_h}\right)\,,\ x_g = \tfrac{1}{\sqrt{s}}\left(p_T^\gamma\, e^{-\eta_\gamma} + \tfrac{p_T^h}{z_f}\, e^{-\eta_h}\right)\,,$$
$$z_f = \tfrac{p_T^h}{l_T}\,,\qquad z_f^{\min} = \tfrac{p_T^h}{\sqrt{s}}\left(\tfrac{e^{\eta_h}}{1-(p_T^\gamma/\sqrt{s})\,e^{\eta_\gamma}}\right)\,.$$

The single inclusive prompt photon cross section in the CGC framework can be obtained from Eq. (51) by integrating over the momenta of the final state quark or antiquark. The corresponding cross section can be then divided into two contributions: fragmentation (first term) and direct (second term) photons,[134]

$$\frac{d\sigma^{p\,A\to\gamma(p^\gamma)\,X}}{d^2\vec{b}_T d^2\vec{p}_T^{\,\gamma} d\eta_\gamma} = \frac{K}{(2\pi)^2}\Big[\int_{x_q^{\min}}^1 dx_q f_q(x_q,Q^2)\frac{1}{z}\,N_F(x_g,p_T^\gamma/z)D_{\gamma/q}(z,Q^2)$$
$$+\frac{e_q^2\alpha_{\rm em}}{2\pi^2(p_T^\gamma)^4}\int_{x_q^{\min}}^1 dx_q f_q(x_q,Q^2)z^2[1+(1-z)^2]\int_{l_T^2<Q^2} d^2\vec{l}_T\, l_T^2\, N_F(\bar{x}_g,l_T)\Big],$$

where $D_{\gamma/q}(z,Q^2)$ is the leading order quark-photon fragmentation function.[68,129,131] Similar to the hybrid formalism for inclusive hadron production, Eq. (4), Q is a hard scale. Although the cross sections given in Eq. (4) and Eq. (53) describe different final-state particle production, they are strikingly similar. The light-cone momentum fractions x_g, $\bar{x}_g$, and z above are related to the transverse momentum and rapidity of the prompt photon,[134]

$$x_g = x_q\, e^{-2\,\eta_\gamma}\,,\ \bar{x}_g = \tfrac{1}{x_q\,s}\left[\tfrac{(p_T^\gamma)^2}{z} + \tfrac{(l_T-p_T^\gamma)^2}{1-z}\right]\,,$$
$$x_q^{\min} = \tfrac{p_T^\gamma}{\sqrt{s}}e^{\eta_\gamma}\,,\ z = \tfrac{p_T^\gamma}{x_q\sqrt{s}}e^{\eta_\gamma}\,.$$

The expression in Eq. (53) was obtained using a hard cutoff to subtract the collinear singularity.[134] The use of a cutoff may result in a mismatch between the finite corrections to Eq. (53) and those included in parameterizations of the photon fragmentation function. However, this mismatch is higher-order in the coupling constant and its proper treatment requires a full NLO calculation.

In Eqs. (52) and (53), the factorization scale μ_F is assumed to be the same in the fragmentation functions and the parton densities. In order to investigate the uncertainties associated with choice of μ_F, several values of μ_F are considered: $\mu_F = 2p_T^\gamma$; p_T^γ; and $p_T^\gamma/2$. The amplitude N_F in Eqs. (51) and (53) is defined in Eq. (6).

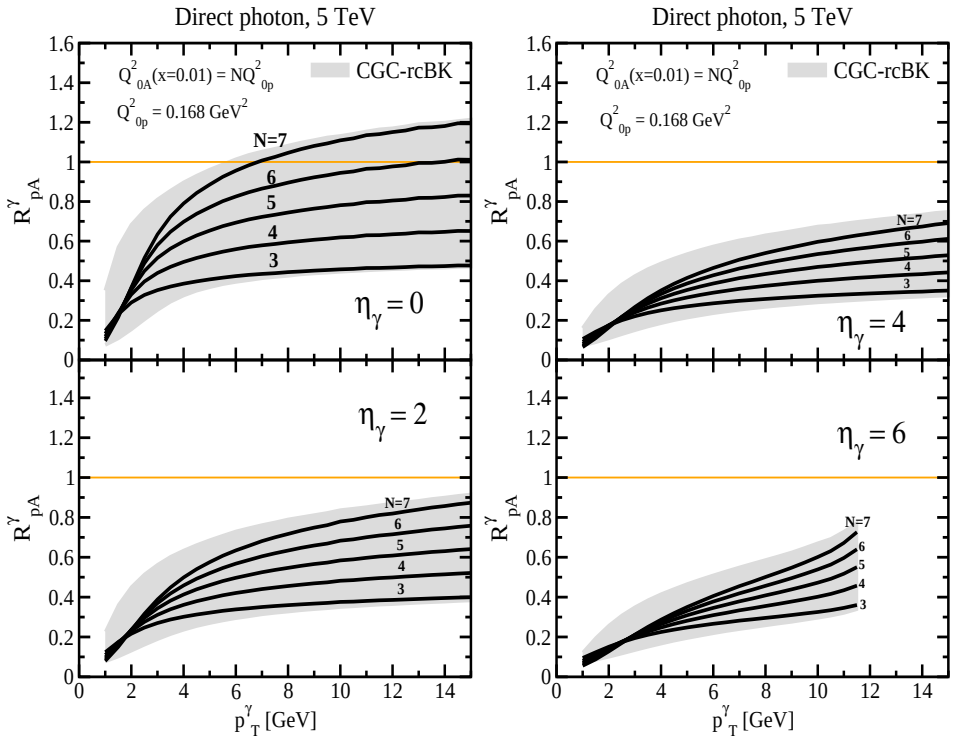

Fig. 26. The nuclear modification factor R^γ_{pA} for direct photon production in minimum bias p+Pb collisions at rapidities $\eta_\gamma = 0$, 2, 4, and 6 (with the convention that the proton beam moves toward forward rapidity) obtained from Eq. (53) with solutions of the rcBK equation with different initial nuclear saturation scales. The band labeled CGC-rcBK includes uncertainties due to the variation of the nuclear saturation scale and the factorization scale μ_F. Similar to Fig. 10, the lines labeled N are results with a fixed factorization scale, $\mu_F = p^\gamma_T$, and a fixed saturation scale $Q^2_{0A} = NQ^2_{0p}$ with $Q^2_{0p} = 0.168\,\mathrm{GeV}^2/c^2$. The range $3 < N < 7$ is constrained in Eq. (39). See Ref.[20]

In Figs. 26 and 27, predictions of the direct photon and single inclusive prompt photon production nuclear modification factors $R^\gamma_{pA}(p_T)$ in minimum bias p+Pb collisions at several rapidities. The solutions of the rcBK equation were obtained using Eq. (53) with different initial nuclear saturation scales. The band labeled CGC-rcBK includes uncertainties due to the variation of Q^2_{0A} within the range given in Eq. (39) with factorization scales $\mu_F = 2p^\gamma_T$, p^γ_T, and $p^\gamma_T/2$. In Fig. 27, the $\eta_\gamma = 0$ results include inclusive prompt photon production calculated in Ref.[135] employing the Iancu-Itakura-Munier (IIM) saturation model which also provides a good description of the HERA data.[136] In the IIM method, saturation is approached from the BFKL region. Therefore the IIM small-x evolution is different from that obtained with the rcBK equation.

As discussed in Sec. 3.3.3, the results in Figs. 26 and 27 on R^γ_{pA}, together with those on R^{ch}_{pA} in Fig. 10, can be used to fix the nuclear saturation scale. Once Q^2_{0A}

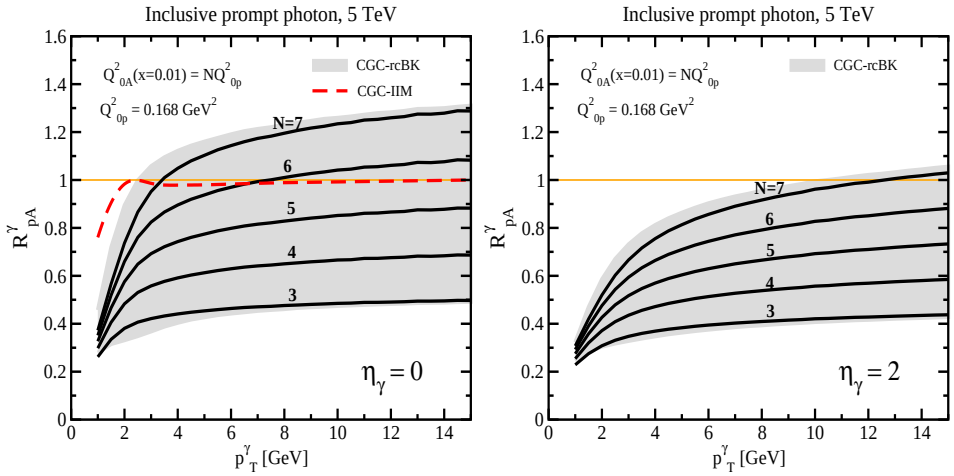

Fig. 27. The nuclear modification factor R^γ_{pA} for single inclusive prompt photon production in minimum bias p+Pb collisions at $\eta_\gamma = 0$ and 2 (with the convention that the proton beam moves toward forward rapidity). The curves are described in Fig. 26. The dashed red line labeled CGC-IIM was calculated according to the IIM dipole saturation model.[135] See Ref.[20]

has been established at one rapidity, the predictions at other rapidities are fixed and the CGC/saturation dynamics can be tested.

6.3.1. *Photon-hadron correlations*

Photon-hadron azimuthal correlations in $p + A$ and $p + p$ collisions could be an excellent probe of small-x dynamics.[134, 137] This correlation can be defined as,[134, 137]

$$P(\Delta\phi) = \left[\frac{d\sigma^{p\,A\to h(p_T^h)\,\gamma(p_T^\gamma)\,X}[\Delta\phi]}{d^2\vec{b_T}\,p_T^h dp_T^h\,p_T^\gamma dp_T^\gamma\,d\eta_\gamma\,d\eta_h\,d\phi}\right]\left[\frac{d\sigma^{p\,A\to h(p_T^h)\,\gamma(p_T^\gamma)\,X}[\Delta\phi=\Delta\phi_c]}{d^2\vec{b_T}\,p_T^h dp_T^h\,p_T^\gamma dp_T^\gamma\,d\eta_\gamma\,d\eta_h\,d\phi}\right]^{-1} \quad (54)$$

The correlation function $P(\Delta\phi)$ is the probability of semi-inclusive photon-hadron pair production in a certain kinematic region at angle $\Delta\phi$ relative to production in the same kinematics at fixed reference angle, $\Delta\phi_c = \pi/2$.[134, 137]

Fig. 28 shows the predicted $P(\Delta\phi)$ in minimum bias $p + p$ and p+Pb collisions at 5 TeV for $p_T^h < p_T^\gamma$ (left) and $p_T^h > p_T^\gamma$ (right). Given the p_T of the produced photon and hadron, the corresponding correlation can have either a double or single peak structure. In Ref.[137] it was shown that this feature is related to saturation physics and is governed by the ratio p_T^h/p_T^γ. The change from a double to a single peak correlation, depending on the relative p_T, is unique to semi-inclusive photon-hadron production: since the trigger particle in dihadron correlations is always a hadron, it consistently exhibits a single-peak structure.

Photon-hadron correlations can also be quantified by the coincidence probability. In contrast to production of a more symmetric final state such as dihadron

production, in photon-hadron production the trigger particle can be either the prompt photon or the hadron.[137] When the photon is used as the trigger, the coincidence probability is defined as $CP_h(\Delta\phi) = N_h^{\rm pair}(\Delta\phi)/N_\gamma$ where $N_h^{\rm pair}(\Delta\phi)$ is the photon-hadron yield. The momentum of the photon trigger, the leading (L) particle, is denoted $p_{T,L}^\gamma$ while the momentum of the associated (S) hadron (typically a π^0) is denoted $p_{T,S}^h$. The azimuthal angle between the photon and the π^0 is $\Delta\phi$,[137]

$$CP_h(\Delta\phi; p_{T,S}^h, p_{T,L}^\gamma; \eta_\gamma, \eta_h) = \frac{2\pi \int_{p_{T,L}^\gamma} dp_T^\gamma p_T^\gamma \int_{p_{T,S}^h} dp_T^h p_T^h \frac{dN^{p\,A\to h(p_T^h)\,\gamma(p_T^\gamma)\,X}}{d^2\vec{p_T}^{\,\gamma}\, d^2\vec{p_T}^{\,h}\, d\eta^\gamma\, d\eta^h}}{\int_{p_{T,L}^\gamma} d^2\vec{p_T}^{\,\gamma}\, \frac{dN^{p\,A\to\gamma(p_T^\gamma)\,X}}{d^2\vec{p_T}^{\,\gamma}\, d\eta_\gamma}} \quad (55)$$

The integrals are carried out within momentum intervals defined by $p_{T,L}^\gamma$ and $p_{T,S}^h$. The yields in the above expression are defined in Eqs. (51) and (53). The correlation defined in Eq. (54) can be considered as a snapshot of the integrand in the coincidence probability defined in Eq. (55). In the same fashion, one can define a hadron-triggered coincidence probability.[137] If the π^0 is the trigger particle, the momenta are instead denoted by $p_{T,S}^\gamma$ and $p_{T,L}^h$ which then become the lower limits on the integrals in Eq. (55). The away-side coincidence probability for the azimuthal correlation of photon-hadron pairs can also have a double-peak or single-peak structure, depending on the trigger particle selection and kinematics.[137]

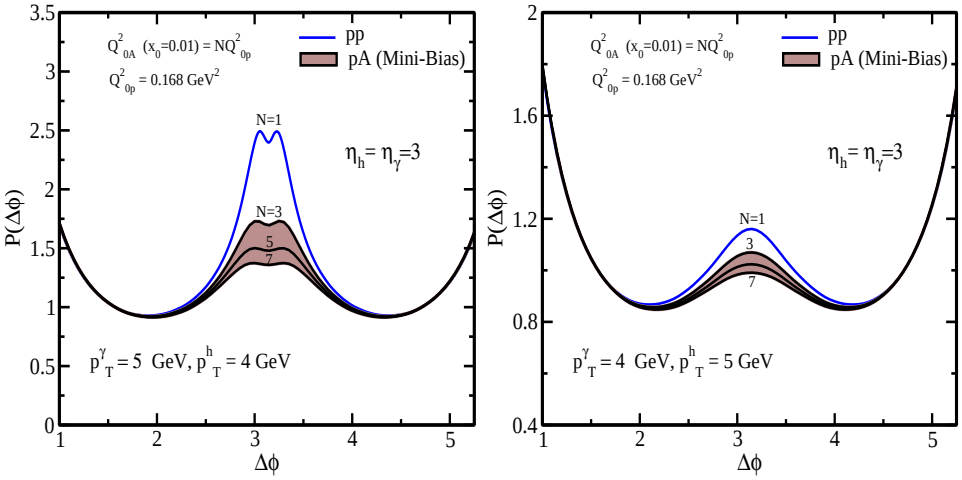

Fig. 28. The $\gamma - \pi^0$ correlation $P(\Delta\phi)$ defined in Eq. (54) in minimum bias $p+p$ and p+Pb collisions at $\sqrt{S} = 5$ TeV and $\eta_h = \eta_\gamma = 3$ (with the convention that the proton beam moves toward forward rapidity) obtained via the rcBK evolution equation with several initial saturation scales, $Q_{0A}^2 = NQ_{0p}^2$ with $N = 3$, 5, and 7, in two different transverse momentum regions: $p_T^h < p_T^\gamma$ (left) and $p_T^h > p_T^\gamma$ (right). Taken from Ref.[20, 137]

In Fig. 29, predictions of the azimuthal correlations between the produced prompt photon and hadron, calculated employing the coincidence probability CP_h

in p+Pb collisions are shown for $\sqrt{s} = 0.2$, 5, and 8.8 TeV. Equation (53) is used in the denominator of Eq. (55). The collinear divergence was removed from Eq. (55) by introducing the photon fragmentation function. The numerator is calculated using Eq. (51). An overall normalization problem may result given that the away-side correlation at $\Delta\phi = \pi/2$ is not sensitive to the collinear singularity. Proper treatment of this problem requires a full NLO calculation which is currently unavailable. However, choosing a different photon fragmentation function[68, 129, 131] will only slightly change the results given the freedom to choose the fragmentation scale and the rather large uncertainties due to Q_{0A}^2. This possible normalization problem is not present in the correlation defined via Eq. (54).

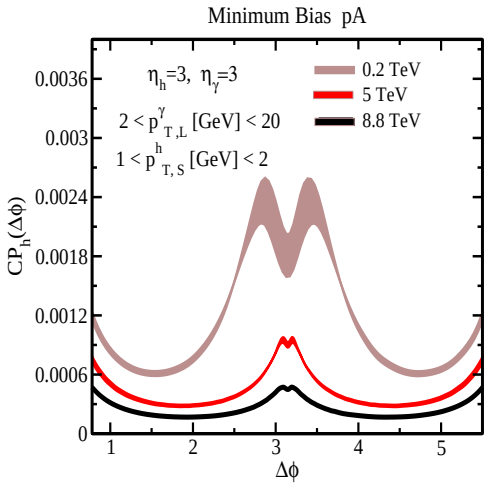

Fig. 29. The $\gamma - \pi^0$ coincident probability, $CP_h(\Delta\phi)$, defined in Eq. (55) in minimum-bias $p + A$ collisions at $\eta_h = \eta_\gamma = 3$ (with the convention that the proton beam moves toward forward rapidity) for $\sqrt{s} = 0.2$, 5 and 8.8 TeV. Taken from Ref.[20, 137]

Although there are theoretical uncertainties associated with the strength of the photon-hadron correlations, due to both higher-order corrections and the less constrained saturation scale Q_{0A}^2. Nevertheless, the decorrelation of away-side photon-hadron production increases with energy, rapidity and density. This decorrelation, together with the appearance of a double or single-peak structure, are robust predictions of CGC/saturation effects in the leading-log approximation.

6.4. *Proton-nucleus dilepton and photon production at the LHC: gluon saturation and shadowing (R. Baier, F. Gelis, A. H. Mueller and D. Schiff)*

Here, a qualitative discussion on saturation and shadowing effects on photon and dilepton production at very large rapidity in high-energy proton-nucleus collisions

is given. The aim is to describe the various steps of assumptions leading to the present understanding.

In $\sqrt{s_{NN}} = 200$ GeV d+Au data on high-p_T hadron production at large rapidity (on the deuteron side) there is a significant suppression of hadron production compared to the expectation from $p + p$ collisions. This result suggests that there may be a significant amount of leading-twist gluon shadowing in the nuclear wavefunction in the region probed by forward hard scattering at RHIC, with even more expected at the LHC.

In many ways hard photons (or dileptons arising from virtual photons) are a better probe than high-p_T hadrons. Photons are less sensitive to fragmentation effects while final-state effects are almost absent. Thus, at $p_T \sim 2 - 3$ GeV/c, leading-twist factorization is expected to be accurate. Hence the nuclear gluon distribution probes x values somewhat smaller than 10^{-4} in p+Pb collisions at the LHC.

Increasing the photon rapidity into the forward (proton rapidity) region, $y > 0$, the gluon x probed decreases rapidly, *e.g.* for virtual photons of mass M and rapidity y produced in the process $q+g \to \gamma^*$, $x \simeq (M/\sqrt{s}) \exp(-y)$. With $\sqrt{s} = 5500$ GeV, $M = 5.0$ GeV/c^2, and $y = 3.5$, $x = 2.7 \times 10^{-5}$, so that indeed a fast quark in the direction of proton rapidity produces virtual photons that probe the small x gluon distribution in the nucleus.

It is extremely interesting to explore, at least qualitatively, the size of the suppression one might expect in such reactions. The treatment here follows Ref.[133] which can be examined for further details. This discussion is based on a picture derived from the Color Glass Condensate (CGC) effective theory for the gluon distribution[iii] together with BFKL evolution (see e.g. Ref.[140]) to reach higher values of y.

6.4.1. *Factorized formula for the inclusive γ^* cross section*

A dimensionless observable, $\sigma(\vec{Q}, Y)$, can be written in the $k_\perp$-factorized form

$$\sigma(\vec{\mu}, Y) = \int \frac{d^2 q_T}{\pi q_T^2} H(\vec{q}_T, \vec{\mu})\, \phi_G(\vec{q}_T, Y)\,, \tag{56}$$

where μ is the hard scale of the reaction, equal to the transverse momentum, k_T, of the (massive) photon, i.e.

$$\sigma(\vec{k}_T, Y) \equiv \sigma(\vec{b}_T, \vec{k}_T, Y) = \frac{k_T^2 d\sigma}{d^2 b_T d^2 k_T d\ln z}\,. \tag{57}$$

For simplicity incident quarks are considered instead of protons, $q + A \to \gamma^* X$, see Fig. 30. Here k_T is the transverse momentum of the γ^*, and z is the longitudinal momentum fraction of the γ^* with respect to the incident quark momentum, $z = k_+/p_+$, where $p_+ \to \infty$. The impact parameter of the $q + A$ collisions is denoted $\vec{b}$ and $Y = \ln 1/x$.

[iii] For recent reviews, see Refs.[138, 139] and references therein.

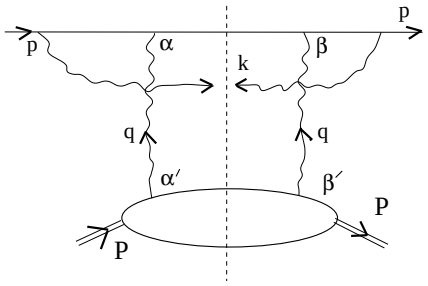

Fig. 30. Two gluon exchange graph for quark (p) + nucleus (P) production of a real or virtual photon, $\rightarrow\ \gamma^{(*)}(k)\ X$.

The leading-twist contribution involves only two exchanged gluons, as shown in Fig. 30. H is the hard part of the interaction in the k_T-factorized form while $\phi_G(\vec{q}_T, Y)/q_T^2$ is considered to be proportional to the differential high energy $q+A \rightarrow q + A$ cross section.

6.4.2. *Anomalous scaling and shadowing - specific predictions*

While there are theoretical uncertainties, there are also robust characteristic qualitative results. The function $\phi_G(k_T, Y)$ can be approximated by the scaling function,

$$\phi_G(k_T, Y) = \phi_G(k_T/Q_s(\vec{b}, Y)) \approx \left(k_T^2/Q_s^2(\vec{b}, Y)\right)^{\lambda_0 - 1}, \tag{58}$$

with anomalous dimension $\lambda_0 \simeq 0.37$ and saturation scale Q_s. In $\vec{b} = 0$ collisions at fixed k_T and Y, an anomalous A dependence is predicted, together with shadowing/suppression of the ratio R_{pA},

$$R_{pA} \approx A^{-\lambda_0/3}\ . \tag{59}$$

In order to obtain results at large photon rapidities based on the BFKL evolution in the presence of saturation, the rapidity dependence of the saturation scale is chosen to be compatible with phenomenology,

$$Q_s^2(\vec{b} = 0, Y = y) = Q_s^2(Y = 0)\exp(\lambda\, y), \quad \lambda \simeq 0.3\ . \tag{60}$$

There is significant suppression expected, $R_{pA} \simeq 0.5$, especially when the $\gamma^{(*)}$ is produced at forward (in the proton direction) rapidities, e.g. $y > 3$ and $k_T > 2$ GeV/c. More detailed predictions of forward inclusive prompt photon production and semi-inclusive photon-hadron correlations in high energy proton-nucleus collisions at the LHC using the CGC formalism are presented in Refs.[134, 137]

Measurements of photons and dileptons, in addition to hadrons with moderate transverse momenta but at large rapidities in p+Pb collisions at the LHC will provide important information supporting the saturation picture of high density gluon dynamics at high energies and small values of x.

7. Jets

In this section, several results for jet production and modification in media are presented. Multi-jet production is discussed and predictions for the jet yields are shown in Sec. 7.1. Cold nuclear matter effects on jet and dijet production are presented in Sec. 7.2. The angular decorrelation of dijets due to saturation effects is discussed in Sec. 7.3. Predictions of long-range near-side azimuthal collimation event with high multiplicity are given in Sec. 7.4. Finally, enhanced transverse momentum broadening in medium is described in Sec. 7.5.

7.1. *Multi-jet Production (N. Armesto)*

The study of jet production in Pb+Pb collisions at the LHC[141–146] and their medium modifications, are important for probing the properties of the hot and dense matter formed in heavy-ion collisions and is thus a very hot topic in heavy-ion physics. Therefore, studies of (multi-)jet production in $p + A$ collisions are of great importance as a cold QCD matter benchmark. Here the jet rates in minimum bias p+Pb collisions at the LHC (4+1.58 TeV per nucleon) are computed using the Monte Carlo code in Refs.[147–149] that implements fixed-order perturbative QCD up to next-lo-leading order. This code produces at most three jets and contains neither parton cascades nor hadronization corrections.

In the computation, the renormalization and factorization scales have been set equal and fixed to $\mu = \mu_F = \mu_R = E_T$, where E_T is the total transverse energy in the event. The central set of the NLO MSTW2008 parton densities (MSTW2008nlo68cl)[114] have been used for the unmodified nucleons. The nuclear modification of parton densities was examined using the EKS98[92,150] and EPS09NLO[48] sets. The standard Hessian method was employed to estimate the uncertainties coming from nuclear parton densities. The precision of the computation, limited by CPU time, gives statistical uncertainties smaller than 10% for the bin with the highest E_T in the results shown here. The anti-k_T jet finding algorithm with $R = 0.5$[151] was used. Only jets with $E_T > 20$ GeV are considered. The uncertainties due to the choice of nucleon parton densities, isospin corrections, and scale fixing, together with the influence of the jet-finding algorithm and the choice of nuclear targets and collision energies, were discussed elsewhere[152,153] and are not considered here.

Figure 31 shows the sum of the 1-, 2- and 3-jet yields, as well as the individual 2- and 3-jet yields within four pseudorapidity windows (two central, one backward and one forward) in the lab frame as a function of the E_T of the hardest jet within the acceptance, $E_{T\,\mathrm{hardest}}$. The yields, computed for luminosity $\mathcal{L} = 0.25 \times 10^{29}$ $\mathrm{cm}^{-2}\mathrm{s}^{-1}$ integrated over a one month (10^6 s) run (corresponding to an integrated luminosity of 25 nb^{-1}),[154] are quite large. The yields are given on the right-hand vertical axes in Fig. 31. High yields are required to study cold matter effects in high p_T multi-jet production. Figure 31 demonstrates that such studies are feasible. For example, in the backward region, $-4.75 < \eta < -3$, sufficiently high rates for the

sum per GeV of 1+2+3-jet events can be achieved for $E_{T_{\rm hardest}} < 50$ GeV. The only regions where the yields from certain channels are too low for statistically significant results are those for 3-jet events in the forward region and 2- and 3-jets in the backward region (only the yields for 2-jet events are shown). Note that the turnover in the 2-jet yields when $E_{T_{\rm hardest}} \to 20$ GeV comes from singularities that appear in the NLO calculation due to large logarithms because $E_{T_1} \sim E_{T_2} (\sim E_{T_3})$. Resummation techniques are required to obtain reliable results in this kinematic region.

Nuclear modifications of the PDFs are very small, maximum $\mathcal{O}(20\%)$, hardly visible in the yields in Fig. 31. Note that the wide uncertainty bands in the largest $E_{T_{\rm hardest}}$ bins in the forward and backward regions are due to statistical fluctuations in the Monte Carlo and do not have a physical origin. The corresponding hot nuclear matter effects in Pb+Pb collisions are expected to be much larger.

Further work to compare these yields with experimental data would require consideration of hadronization corrections and the effects of background subtraction such as in the well-established jet area method.[155] These should be the subject of future studies.

7.2. *Cold matter effects on jet and dijet production (Y. He, B.-W. Zhang and E. Wang)*

Inclusive NLO[156–161] jet and dijet production are studied in p+Pb collisions. Cold nuclear matter effects are included by employing the EPS09,[48] DS11[162,163] and HKN07[164] parametrizations of nuclear parton densities. The numerical results for the inclusive jet spectrum, the dijet transverse energy and mass spectra, and the dijet triply-differential cross sections, all using a jet cone size $R = 0.4$ in minimum bias p+Pb collisions are shown.

The left-hand side of Fig. 32 illustrates the inclusive jet spectra scaled by $N_{\rm coll}$ including the nuclear modifications in the central rapidity region, $|y| < 1$. Results for $R_{p\rm Pb}$ are also shown. The spectra with EPS09 and HKN07 show an enhancement in the transverse energy range $30 < E_T < 200$ GeV. However, the CNM effects are negligible over the entire region of jet E_T with DS11.

The right-hand side of Fig. 32 displays the rescaled dijet E_T spectra as a function of E_{T2} with jet 1 at a fixed transverse energy of $E_{T1} = 100$ GeV employing the same modifications of the parton densities as before. Both jets are within the central rapidity region, $|y_1| < 1$ and $|y_2| < 1$. The cross sections in the range $10 < E_T < 200$ GeV exhibit a peak near $E_T = 100$ GeV. Again the spectra with EPS09 and HKN07 are enhanced. On the other hand, the DS11 set shows very small suppression and enhancement as shown in Fig 32.

Figure 33 gives the rescaled dijet invariant mass M_{JJ} spectra and the corresponding nuclear modification factors. Here M_{JJ} is defined as $[(\sum p_n^\mu)^2]^{1/2}$ where the sum is over all particles in the two jets.[165] The maximum rapidity of the two leading jets, $|y|_{\rm max} = \max(|y_1|, |y_2|)$ is defined so that $|y|_{\rm max} < 1$. Jets with energies

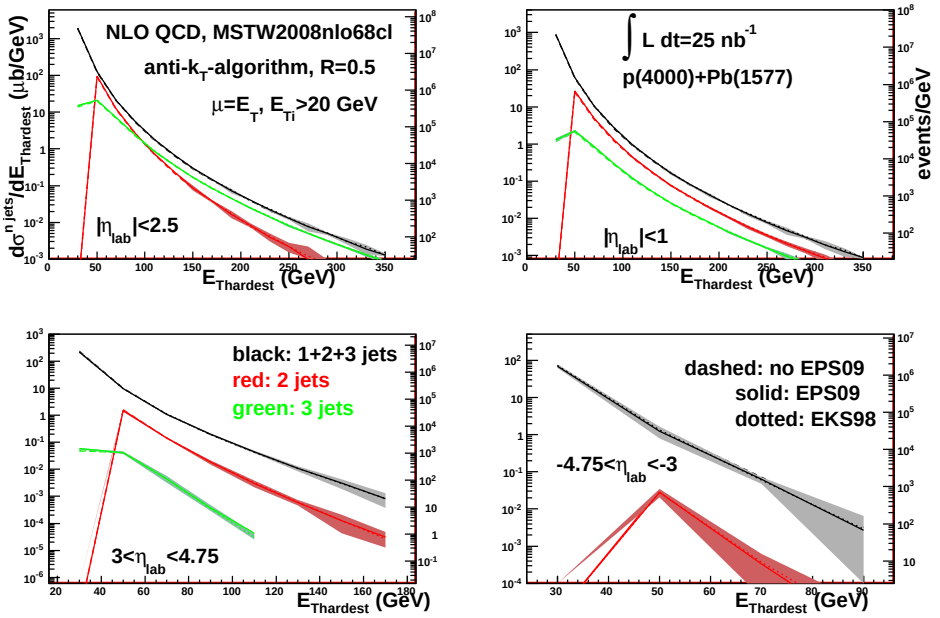

Fig. 31. The 1+2+3- (black), 2- (red) and 3-jet (green) cross sections as a function of the E_T of the hardest jet within the acceptance. Results in different pseudorapidity windows in the laboratory frame computed for minimum bias p+Pb collisions are shown. The dashed lines are the results without nuclear modifications of the PDFs. Results with EPS09NLO[48] (solid) and EKS98 (dotted)[92,150] are also shown. The bands correspond to uncertainties computed using the Hessian method for EPS09.[48] The right vertical axes gives the scale for the corresponding yields with an integrated luminosity of 25 nb^{-1}. See the text for further details.

greater than 40 GeV in the rapidity range $|y| < 2.8$ are selected. The CNM effects with EPS09 and HKN07 also enhance the M_{JJ} spectra over a wide M_{JJ} region while the effect with DS11 is modest.

Figure 33 also shows the rescaled dijet triply differential cross sections[166] and their nuclear modifications. The momentum fractions x_1 and x_2 are defined as

$$x_1 = \sum_{i\in\text{jet}} \frac{E_{Ti}}{\sqrt{s}} e^{y_i} \ , \quad x_2 = \sum_{i\in\text{jet}} \frac{E_{Ti}}{\sqrt{s}} e^{-y_i} \ . \tag{61}$$

where the sums run over all particles in the jets. The results in Fig. 33 are shown for the rapidity difference between the jets, $y_* = 0.5(|y_1 - y_2|)$ where y_1 and y_2 are the rapidities of the two leading jets. The results as a function of x show obvious deviations between nuclear modification factors which implies that the dijet triply-differential cross sections could be a good observable to distinguish between different shadowing parameterizations.[167]

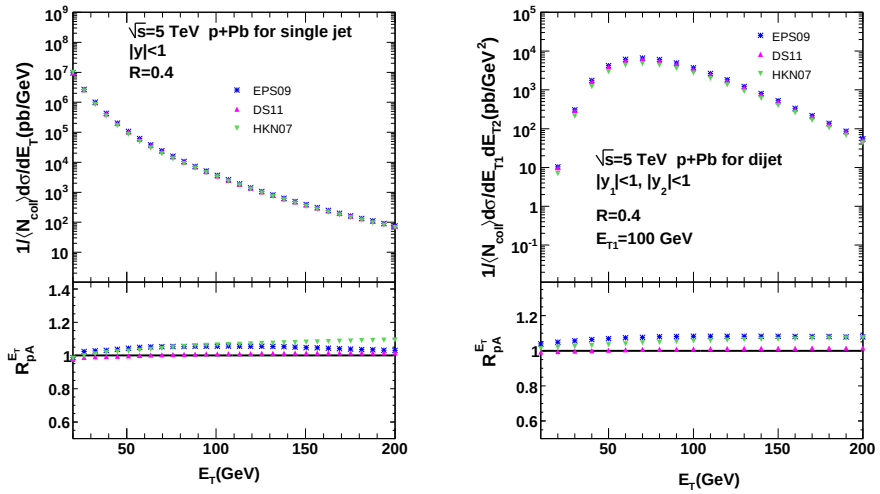

Fig. 32. The inclusive jet (left) and dijet (right) results in p+Pb collisions at $\sqrt{s} = 5$ TeV. The dijet results, presented as a function of E_{T2} are given for fixed energy $E_{T1} = 100$ GeV for jet 1. The rapidity acceptance for all jets is $|y| < 1$. The E_T spectra are shown in the upper part of the plots while the nuclear modification factors are shown in the lower panels of the figures.

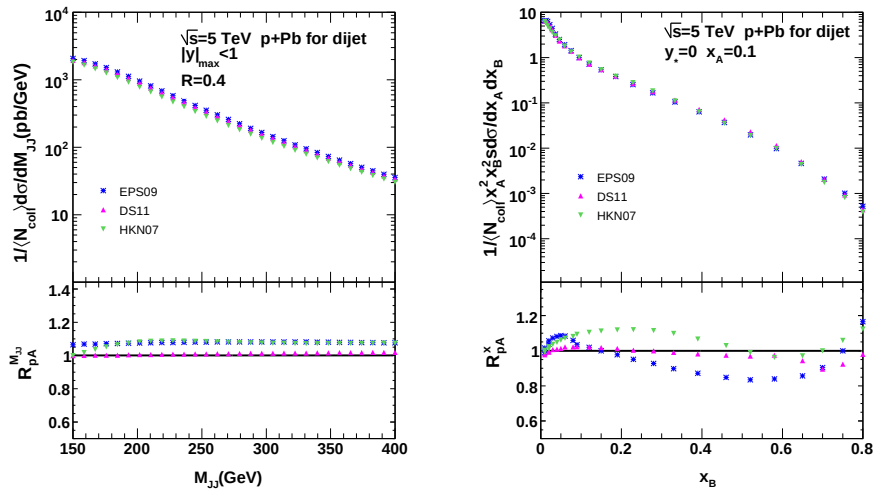

Fig. 33. (Left) The dijet invariant mass spectra in p+Pb collisions. (Right) The dijet triply differential cross sections in p+Pb collisions. The nuclear modification factors, $R_{p\mathrm{Pb}}$, are also shown.

7.3. *Angular decorrelation of dijets as a signature of gluon saturation (K. Kutak and S. Sapeta)*

Here predictions for the emergence of saturation[168] effects on dijet production in p+Pb scattering at the LHC. The results are based on a study performed in Refs.[169,170] The saturation scale characterizes formation of a dense system of partons. There is growing evidence that the phenomenon of gluon saturation indeed occurs.[171,172] This calculation employs a high-energy factorization formalism which accounts for both the high energy scale of the scattering and the hard momentum scale p_T provided by produced hard system.[173] Dijets separated by large rapidity gaps[174] are considered here. More specifically, the focus is on a case where one jet is measured in the central rapidity region of the detectors while the other is at large rapidity, see Fig. 34. Such final states probe the parton density in one of the hadrons at low momentum fraction x while the other is at relatively large x. Predictions of azimuthal decorrelations of dijets production in p+Pb relative to $p+p$ collisions are presented.

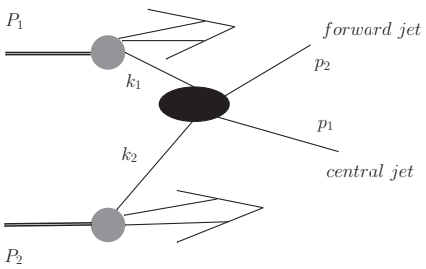

Fig. 34. Jet production in the forward (assuming the proton moves toward positive rapidity) region in hadron-hadron collisions.

Assuming, without loss of generality, that $x_1 \simeq 1$ and $x_2 \ll 1$ (if the proton moves in the direction of forward rapidity), the cross section takes the form

$$\frac{d\sigma}{dy_1 dy_2 dp_{T1} dp_{T2} d\Delta\phi} = \sum_{a,c,d} \frac{p_{T1} p_{T2}}{8\pi^2 (x_1 x_2 s)^2} \times \mathcal{M}_{ag\to cd} x_1 f_{a/A}(x_1, \mu^2)\, \phi_{g/B}(x_2, k_T^2) \frac{1}{1+\delta_{cd}} \ , \quad (62)$$

where

$$k_T^2 = p_{T1}^2 + p_{T2}^2 + 2 p_{T1} p_{T2} \cos\Delta\phi \ , \quad (63)$$

and $\Delta\phi$ is the azimuthal distance between the outgoing partons. The squared matrix element $\mathcal{M}_{ag\to cd}$ includes $2 \to 2$ process with one off-shell initial-state gluon and three on-shell partons a, c, and d. The following partonic subprocesses contribute to the production of the dijet system: $qg \to qg$; $gg \to q\bar{q}$; and $gg \to gg$.[175] The off-shell gluon in Eq. (62) is described by the unintegrated gluon density $\phi_{g/B}(x_2, k_T^2)$, a

solution of a nonlinear evolution equation[176,177] that depends on the longitudinal momentum fraction x_2, and the transverse momentum of the off-shell gluon, k_T. On the side of the on-shell parton, probed at high proton x_1, the collinear parton density $f_{a/A}(x_1, \mu^2)$ is appropriate.

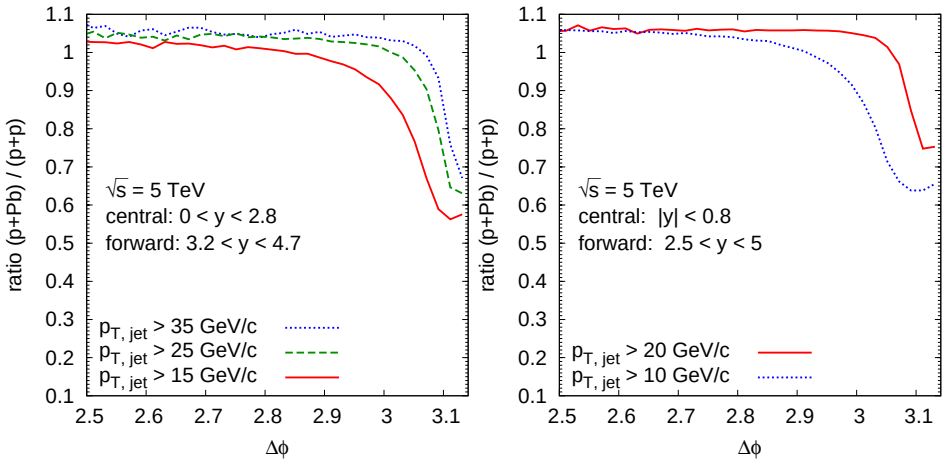

Fig. 35. Ratio of differential cross sections for central-forward dijet production at $\sqrt{s} = 5$ TeV as functions of azimuthal distance between the jets $\Delta\phi$ for three different jet p_T cuts. On the left, the selected rapidities correspond to the CMS detector while, on the right, the rapidity range appropriate for ALICE is shown. The calculations have been made with the convention that the proton beam moves toward forward rapidity.

Figure 35 shows the ratios of the differential cross sections for central-forward dijet production in p+Pb relative to $p + p$ as a function of the azimuthal distance between the jets, $\Delta\phi$. In the region $\Delta\phi \sim \pi$, the gluon density is probed at small k_T, where it is strongly suppressed due to nonlinear effects. The ratio is a signal of saturation that is sensitive to the enhancement of saturation effects afforded by the larger A of the Pb nucleus.

The left-hand side of Fig. 35 shows the results for various jet p_T cuts: $p_{T\,\mathrm{jet}} > 15$, 25, and 35 GeV/c while the jet rapidities are restricted to positive values within the coverage of the central and forward CMS detectors. On the right-hand side of Fig. 35, lower p_T cuts, $p_T > 10$ and 20 GeV/c, are used and the rapidity is restricted to positive values within the central and larger rapidity range of the ALICE detector. The results show that, when the two jets are back-to-back, the cross section ratio is significantly smaller than one. This is a consequence of stronger gluon saturation in the Pb nucleus than in a proton. Thus the unintegrated gluon distribution in the region of small and medium k_T is more suppressed in Pb than in protons, as shown in Fig. 35. In addition to the effects shown here, the region near $\Delta\phi \simeq \pi$ is sensitive to Sudakov effects which further suppress the cross section. Therefore, refinement along those lines could be envisaged in the future. However,

the ratio shown here is less sensitive to these corrections. It is worth emphasizing that the suppression due to saturation predicted in Fig. 35 is strong and extends over a large enough $\Delta\phi$ range for experimental observation, even if the region near $\Delta\phi = \pi$ could be further refined.

7.4. *Predictions for long-range near-side azimuthal collimation in high multiplicity p+Pb collisions (K. Dusling and R. Venugopalan)*

Rapidity-separated dihadron correlation measurements can provide valuable insight into the gluon dynamics of the nuclear wavefunction. For example, it was recently realized[172] that a novel "near-side" azimuthal collimation in high multiplicity $p+p$ events[178] is a consequence of nonlinear gluon interactions and was found to be in excellent agreement with computations in the Color Glass Condensate (CGC) effective field theory.[179,180]

The situation in p+Pb collisions is more attractive. The degree of near-side collimation is highly sensitive to the fine structure of the unintegrated gluon distribution. It can be shown that the collimated yield is enhanced by $\left(Q_s^{\rm Pb}/Q_s^p\right)^2$ in asymmetric collisions. Here $Q_s^{\rm Pb}$ is the saturation scale probed in the lead nucleus and can be estimated to scale with the number of participants, $Q_s^{2,{\rm Pb}} \approx N_{\rm part} Q_s^{2,p}$, where Q_s^p is the saturation scale for the proton. Therefore, for high multiplicity events where many nucleons in the lead nucleus participate, a significant near-side collimation is observed.[181] Similar to the $p+p$ data, calculations within the CGC effective theory are able to explain the data.[182]

This last study combined the physics of saturation and BFKL dynamics in order to understand the near-side collimation and the recoiling away-side jet. Both are required for a full understanding of the azimuthal structure of dihadron correlations. The per-trigger yields shown in Fig. 36 are well described by this framework for the symmetric $p_T^{\rm trig} \sim p_T^{\rm assoc}$ windows where data are currently available. Predictions for the asymmetric $p_T^{\rm trig} \neq p_T^{\rm assoc}$ windows are also shown.

7.5. *Enhancement of transverse momentum broadening (H. Xing, Z.-B. Kang, I. Vitev and E. Wang)*

Both initial-state and final-state multiple scattering lead to acoplanarity, or momentum imbalance of the two leading final-state particles. To quantify this effect, the transverse momentum imbalance $\vec{q}_T$ is defined as:

$$\vec{q}_T = \vec{p}_{T1} + \vec{p}_{T2}, \tag{64}$$

with the average squared transverse momentum imbalance

$$\langle q_T^2 \rangle = \left(\int d^2\vec{q}_T q_T^2 \frac{d\sigma}{d\mathcal{PS}\, d^2\vec{q}_T} \right) \left(\frac{d\sigma}{d\mathcal{PS}} \right)^{-1} . \tag{65}$$

Here, $d\sigma/d\mathcal{PS}$ is the differential cross section with the appropriate phase space factor, determined separately for each process. For example, in $p+A$ collisions,

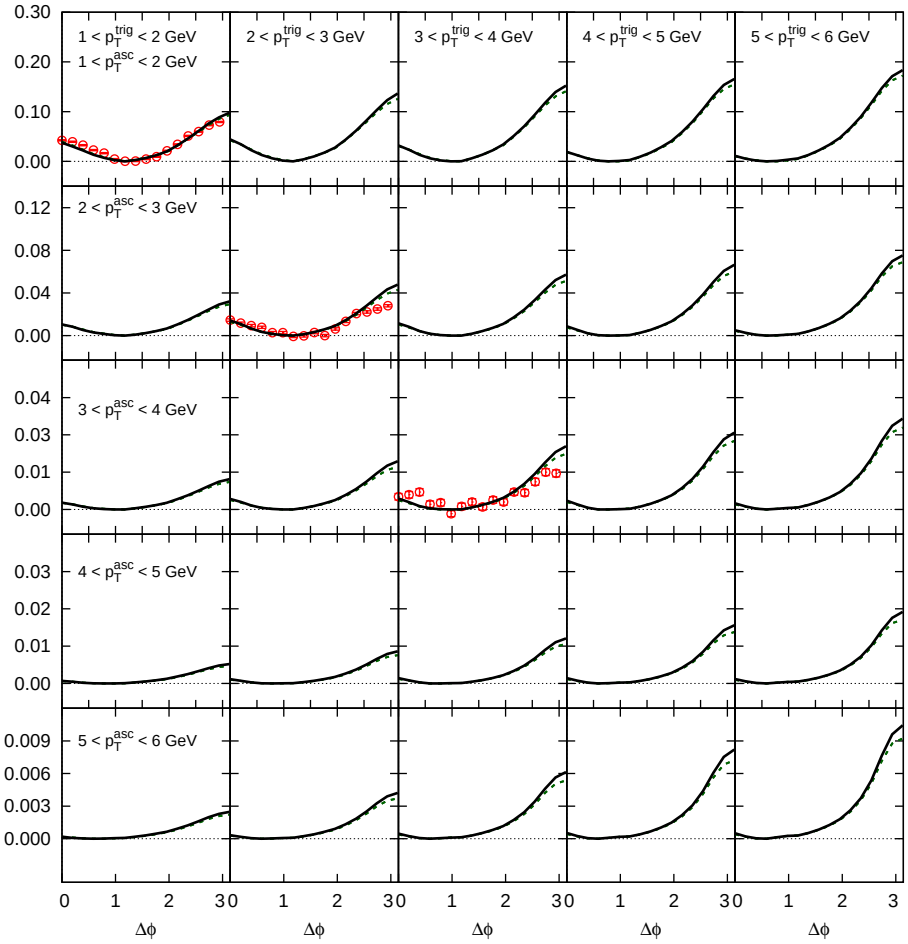

Fig. 36. Correlated yield $1/N_{\rm trig} d^2N/d\Delta\phi$ after ZYAM (zero yield at minimum, used to remove the $\Delta\Phi$-independent pedestal) as a function of $|\Delta\phi|$ integrated over $2 \leq |\Delta\eta| \leq 4$ for the most central multiplicity bin $N_{\rm trk}^{\rm offline} \geq 110$. The CMS data[181] have currently only been provided for the diagonal components, $p_T^{\rm trig} \sim p_T^{\rm assoc}$, of the correlation matrix. The theory curves are the result of adding the BFKL contribution responsible for the away-side jet and the "dipole"-like Glasma contribution. The solid black curve is the result for $Q_{0p}^2 = 0.504$ GeV^2 on $N_{\rm part}^{\rm Pb} = 14$ and the dashed green is for $Q_{0p}^2 = 0.336$ GeV^2 on $N_{\rm part}^{\rm Pb} = 16$.

$d\mathcal{PS} = dy_1 dy_2 dp_T^2$ for photon+jet production and $d\mathcal{PS} = dy_1 dy_2 dp_{T1} dp_{T2}$ for photon+hadron production.

The enhancement of the transverse momentum imbalance (or nuclear broadening) in $h + A$ ($h = p$, γ^*) collisions relative to $h + p$ collisions can be quantified by the difference:

$$\Delta\langle q_T^2\rangle = \langle q_T^2\rangle_{hA} - \langle q_T^2\rangle_{hp} \ . \tag{66}$$

The broadening $\Delta\langle q_T^2\rangle$ is a result of multiple quark and gluon scattering and is a direct probe of the properties of the nuclear medium. Both initial-state and final-state multiple parton interactions are taken into account to calculate the nuclear broadening $\Delta\langle q_T^2\rangle$ for photon+jet (photon+hadron) and heavy quark (heavy meson) pair production in $p + A$ collisions.

The nuclear broadening $\Delta\langle q_T^2\rangle$ can be calculated in perturbative QCD. A specific method based on double parton scattering has been discussed in detail in Refs.[80, 183] The derivation discussed here closely follows Ref.[80] The leading contribution to the nuclear broadening comes from double scattering: either in the initial-state or the final-state. The contributions from these diagrams in the covariant gauge can be calculated to obtain the following expression for the nuclear broadening of photon+jet production in $p + A$ collisions:

$$\Delta\langle q_T^2\rangle = \left(\frac{8\pi^2\alpha_s}{N_c^2-1}\right) \times \frac{\sum_{a,b} f_{a/p}(x') \left[T_{b/A}^{(I)}(x) H_{ab\to\gamma d}^{I}(\hat{s},\hat{t},\hat{u}) + T_{b/A}^{(F)}(x) H_{ab\to\gamma d}^{F}(\hat{s},\hat{t},\hat{u})\right]}{\sum_{a,b} f_{a/p}(x') f_{b/A}(x) H_{ab\to\gamma d}^{U}(\hat{s},\hat{t},\hat{u})} \tag{67}$$

Here $T_{b/A}^{(I)}(x) = T_{q/A}^{(I)}(x)$ (or $T_{g/A}^{(I)}(x)$) are twist-4 quark-gluon (or gluon-gluon) correlation functions associated with initial-state multiple scattering, defined as[80, 183]

$$T_{q/A}^{(I)}(x) = \int \frac{dy^-}{2\pi}\, e^{ixp^+y^-} \int \frac{dy_1^- dy_2^-}{2\pi}\, \theta(y^- - y_1^-)\, \theta(-y_2^-) \times \frac{1}{2}\, \langle p_A | {F_\alpha}^+(y_2^-) \bar{\psi}_q(0) \gamma^+ \psi_q(y^-) F^{+\alpha}(y_1^-) | p_A \rangle \ , \tag{68}$$

$$T_{g/A}^{(I)}(x) = \int \frac{dy^-}{2\pi}\, e^{ixp^+y^-} \int \frac{dy_1^- dy_2^-}{2\pi}\, \theta(y^- - y_1^-)\, \theta(-y_2^-) \times \frac{1}{xp^+}\, \langle p_A | {F_\alpha}^+(y_2^-) F^{\sigma+}(0) F_\sigma^+(y^-) F^{+\alpha}(y_1^-) | p_A \rangle \ . \tag{69}$$

The corresponding twist-4 correlation functions associated with final-state multiple scatter are $T_{q/A}^{(F)}(x)$ and $T_{g/A}^{(F)}(x)$. They are defined as in Eqs. (68) and (69), except the θ-functions are replaced such that,[80, 183]

$$\theta(y^- - y_1^-)\, \theta(-y_2^-) \to \theta(y_1^- - y^-)\, \theta(y_2^-) \ . \tag{70}$$

The broadening in photon + hadron production is calculated similarly.

Nuclear broadening is evaluated in a formalism where multiple scattering contributes to the cross section via higher-twist matrix elements in the nuclear state.

This framework follows a well-established QCD factorization formalism for particle production in $p+A$ collisions and has previously been used to describe cold nuclear matter effects such as energy loss, dynamical shadowing and broadening. This work differs from more generic parton broadening phenomenology in because the color and kinematic structures of the hard part are evaluated exactly. In particular, the nuclear enhancement of the transverse momentum imbalance is studied in dijet and photon+jet production.

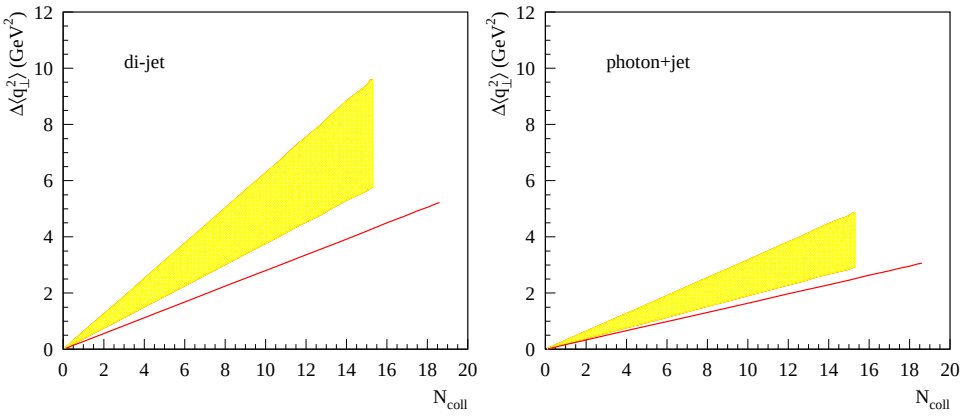

Fig. 37. Nuclear broadening, $\Delta\langle q_T^2\rangle$, is shown for dijet (left) and photon+jet (right) production at specified rapidities in $p+A$ collisions as a function of $N_{\rm coll}$. Results are shown for $y_1 = y_2 = 2$ in $\sqrt{s} = 5$ TeV p+Pb collisions and $y_1 = y_2 = 1$ at $\sqrt{s} = 200$ GeV d+Au collisions. (The calculations have been made with the convention that the proton beam moves toward forward rapidity.) The jet transverse momentum is integrated over $30 < p_T < 40$ GeV/c at $\sqrt{s} = 5$ TeV and $15 < p_T < 25$ GeV/c at $\sqrt{s} = 200$ GeV. The red line shows the result for RHIC kinematics with scattering parameter $\xi^2 = 0.12$ GeV^2 while the yellow band represents the variation of ξ^2 in the LHC kinematics.

The results are shown in Fig. 37. The line gives the baseline $\Delta\langle q_T^2\rangle$ determined from RHIC as a function of $N_{\rm coll}$. The band is the result in the LHC kinematics for a plausible range of the scattering parameter ξ^2, defined in Eq. (29). The band is broader for dijet production and $\Delta\langle q_T^2\rangle$ is also larger. There is also a somewhat larger deviation of the bottom edge of the band from the RHIC result for dijet production.

8. Gauge Bosons

Gauge boson production is discussed in this section. Section 8.1 makes predictions for W and Z^0 p_T and rapidity distributions in $p+p$ and p+Pb collisions. The $W^\pm$ charge asymmetry as a function of the decay lepton rapidity is also shown. Section 8.2 describes a calculation of the resummed Z^0 p_T distribution while transverse broadening of vector boson production is discussed in Sec. 8.3.

8.1. *W and Z production and $W^{\pm}$ charge asymmetry (P. Ru, E. Wang, B.-W. Zhang and W.-N. Zhang)*

Production of the gauge bosons, W^+, W^- and Z^0, is discussed. The transverse momentum and the rapidity distributions in min-bias p+Pb collisions at $\sqrt{s} =$ 5 TeV are calculated at next-to-leading order and next-to-next-to-leading order. The fiducial cross sections $\sigma_{\rm fid}$ are calculated in the fiducial phase space for vector boson production used by ATLAS Collaboration [184,185] in both p+Pb and $p+p$ collisions.

The fiducial Z^0 cross section is the inclusive cross section $p+$ Pb $\to Z^0/\gamma^* + X$ multiplied by the branching ratio for $Z^0/\gamma^* \to l^+l^-$ within the fiducial acceptance. Here X denotes the underlying event and the recoil system. The fiducial acceptance is assumed to be the same as that defined by ATLAS in $p+p$ collisions[184] with the following cuts on the lepton transverse momentum and pseudorapidity, and the dilepton invariant mass: $p_T^l > 20$ GeV/c; $|\eta^l| < 2.4$; and $66 < m_{ll} < 116$ GeV/c^2.

The fiducial $W^{\pm}$ cross sections are the inclusive cross sections $p+$ Pb $\to W^{\pm}+X$ multiplied by the branching ratios for $W^{\pm} \to l\nu$ within the fiducial acceptance. Following the ATLAS definition,[185] the acceptance cuts on lepton and neutrino transverse momentum and pseudorapidity as well as the W transverse mass are: $p_T^l >$ 20 GeV/c; $|\eta_{l,\nu}| < 2.4$; $p_T^\nu > 25$ GeV/c; and $m_T = \sqrt{2p_T^l p_T^\nu(1-\cos(\phi^l - \phi^\nu))} >$ 40 GeV/c^2.

Results are simulated to NLO ($\mathcal{O}(\alpha_s)$) and NNLO ($\mathcal{O}(\alpha_s^2)$) in the total cross section employing `DYNNLO` for Drell-Yan-like production in hadron-hadron collisions.[186] The MSTWNLO and MSTWNNLO proton parton densities are used, along with the EPS09[48] and DSSZ[163] shadowing parameterizations.

Tables 8.1 and 8.1 shows the fiducial cross sections, normalized to their per nucleon values for better comparison. The NLO and NNLO values are shown for comparison, both for p+Pb and $p+p$ collisions at the same energy. The ratio between the NNLO and NLO cross section, giving some indication of the theoretical uncertainty and the convergence of the perturbative expansion for gauge boson production, is ~ 1.02 showing that the higher order corrections are small. When the NLO and NNLO results are compared in p+Pb collisions with the EPS09 shadowing parameterization, a similar correction is found. The difference between the EPS09 and DSSZ parameterizations, both calculated at NLO, is also quite small, on the order of 1%. There is a slight decrease in the total fiducial Z^0 cross section. There is a larger decrease for W^+ and an enhancement in the fiducial cross section in p+Pb collisions. This is less an effect of shadowing than it is of isospin since $u\overline{d} \to W^+$ and $\overline{u}d \to W^-$ and there are more d quarks in the lead nucleus, causing the enhanced cross section.

Figure 38 shows the Z^0 p_T distributions in p+Pb collisions at both NLO and NNLO. The NNLO result is somewhat higher and not as smooth as the NLO calculations which appear independent of the choice of shadowing parameterization. Differences between the results with EPS09 and DSSZ, which can be attributed to

Table 5. The total vector boson production cross sections in the fiducial phase space, $\sigma_{\rm fid}$, in units of nb in $p+p$ collisions. The results at NLO and NNLO are compared.

	$p+p$ $\sigma_{\rm fid}$ (nb)	
Decay channel	MSTWNNLO	MSTWNLO
$Z \to e^+e^-$	0.339	0.332
$W^+ \to e^+\nu$	2.35	2.30
$W^- \to e^-\nu$	1.47	1.44

Table 6. The total vector boson production cross sections per nucleon in the fiducial phase space, $\sigma_{\rm fid}/\langle N_{\rm bin}\rangle$ in p+Pb collisions. Columns 2 and 3 compare the results at NLO and NNLO calculated with EPS09 while columns 3 and 4 compare the EPS09 and DSSZ shadowing parameterizations at NLO.

	p+Pb $\sigma_{\rm fid}/\langle N_{\rm coll}\rangle$ (nb)		
	MSTWNNLO	MSTWNLO	MSTWNLO
Decay channel	EPS09	EPS09	DSSZ
$Z \to e^+e^-$	0.338	0.328	0.329
$W^+ \to e^+\nu$	2.06	2.02	2.05
$W^- \to e^-\nu$	1.54	1.52	1.53

shadowing effects rather than isospin, are only apparent when the ratio $R_{p\,\rm Pb}(p_T)$ is formed. The slight decrease in per nucleon yield in p+Pb relative to $p+p$ seen in the total cross sections in Tables 8.1 and 8.1 are due to the lowest p_T bin, $p_T < 20$ GeV/c. At higher p_T, the ratio increases above unity. However, the effect is not significantly larger than 5% over the entire p_T range.

The individual W^+ and W^- p_T distributions are shown at NLO and NNLO on the left-hand side of Fig. 39. Again, the NLO results are smoother than the NNLO calculations. The difference in the overall cross sections are clearly observable: in the fiducial range of the calculations, the W^+ cross section is $\approx 35\%$ greater than the W^- cross section. The ratio of p+Pb to $p+p$ is shown on the right-hand side of Fig. 39. The W^- ratio is larger than unity and increasing strongly with p_T. The effect is due to the greater abundance of d quarks in the Pb nucleus (126 neutrons vs. 82 protons). The valence d quark distributions in the neutrons, equivalent to the valuence u quark distributions in the protons, have a larger density at relatively high x, causing the observed increase. Conversely, the lower density of valence u quarks in the Pb nucleus causes $R_{p\rm Pb} < 1$ over the entire p_T range. The sum of the two charged gauge bosons shows a trend very similar to that of the Z^0 in Fig. 38, revealing a result closer to the true shadowing effect. Even though the W^+ cross section is greater than that of the W^-, the isospin effect on the W^- is large enough to make the ratio larger than unity at high p_T.

Figures 40 and 41 show the Z^0, W^+ and W^- rapidity distributions, normalized per nucleon. For comparison the $p+p$ and p+Pb distributions are shown both

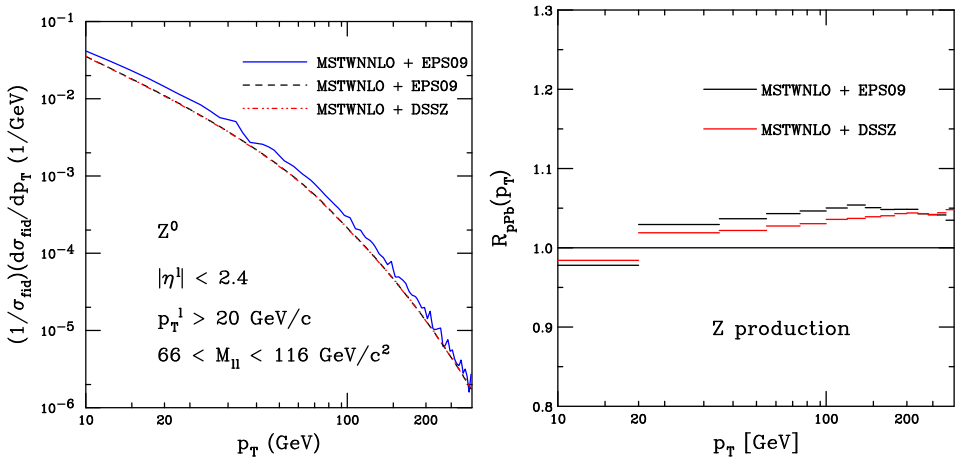

Fig. 38. (Left) Normalized Z^0 differential cross section $(1/\sigma_{\rm fid})(d\sigma_{\rm fid}/dp_T)$. (Right) The suppression factor $R_{pA}(p_T)$ in 20 GeV/c p_T bins.

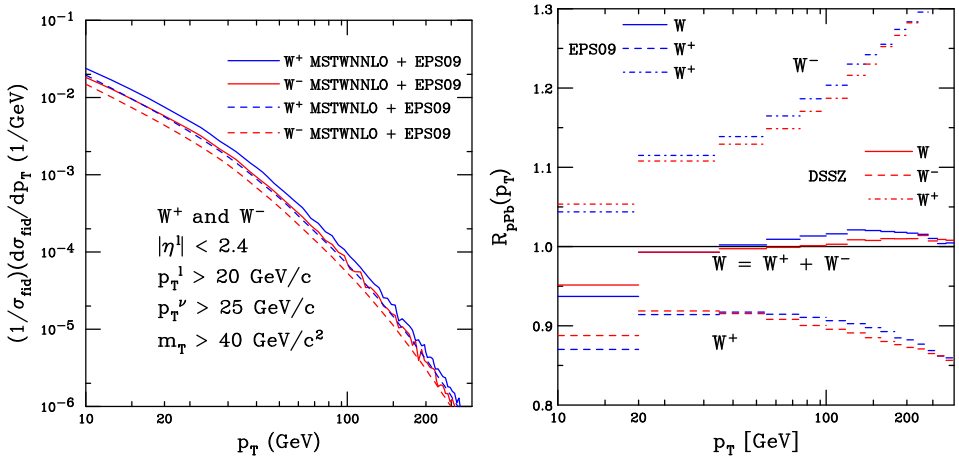

Fig. 39. (Left) The normalized $W = W^+ + W^-$ differential cross section $(1/\sigma_{\rm fid})(d\sigma_{\rm fid}/dp_T)$. (Right) The suppression factor $R_{pA}(p_T)$ for W production given in 20 GeV/c p_T bins.

at NLO and NNLO. Aside from numerical fluctuations at NNLO, the order of the calculation makes little difference in either the shape or the magnitude of the rapidity distributions. The $p+p$ distributions are all symmetric around $y = 0$ while the p+Pb distributions are peaked in the direction of the Pb nucleus.

There are significant differences between the W^+ and W^- distributions even for $p+p$ collisions. The W^+ distribution is considerably broader with peaks away from $y = 0$, at $|y| \sim 1.7$ due to the larger average momentum fraction x of the valence u

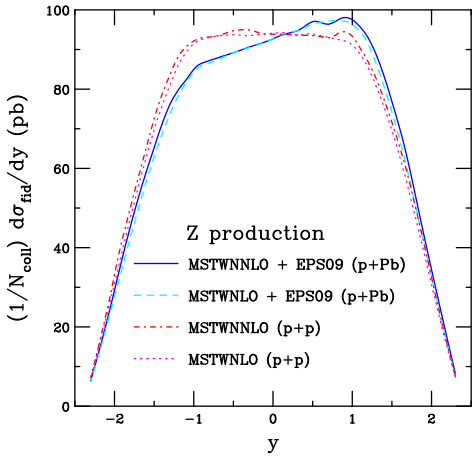

Fig. 40. The Z^0 rapidity distribution $(1/\langle N_{\rm coll}\rangle)(d\sigma_{\rm fid}/dy)$. Results are shown for both p+Pb and $p+p$ collisions in the center-of-mass frame for both systems.

quarks in the proton. The greater density of valence u quarks in the proton leads to the larger overall cross section. The isospin effect tends to make the W^+ rapidity distribution more symmetric since the valence u quark distribution in the neutron, equivalent to the valence d distribution in the proton, has a smaller average x and lower density which reduces the cross section while removing the peaks away from midrapidity. The W^- distribution in $p+p$ collisions is both smaller and narrower than the W^+. This distribution shows the strongest isospin effect with rapidity.

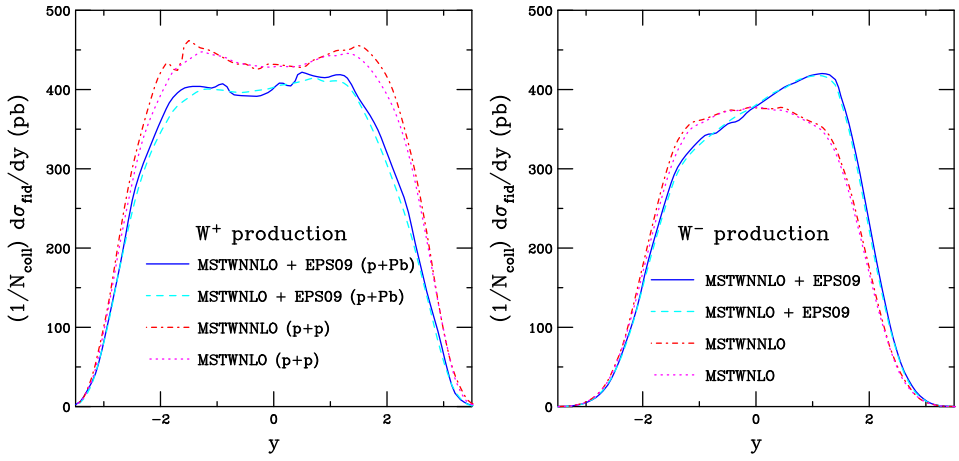

Fig. 41. The W^+ (left) and W^- (right) rapidity distributions $(1/\langle N_{\rm coll}\rangle)(d\sigma_{\rm fid}/dy)$. Results are shown for both p+Pb and $p+p$ collisions in the center-of-mass frame for both systems.

These differences are reflected in the $W^{\pm}$ charge asymmetry, defined as $(N_{W^+} - N_{W^-})/(N_{W^+} + N_{W^-})$ and shown as a function of the decay lepton pseudorapidity. The results are given in Fig. 42. The $p+p$ asymmetry is symmetric around $y = 0$ with a strong dip at midrapidity. The origin is clear from the individual W^+ and W^- rapidity distributions. There is, however, a strong forward/backward asymmetry in p+Pb collisions. In the direction of the proton beam, the asymmetry follows that of the $p + p$ result. It falls off and becomes negative in the direction of the lead beam. This trend is independent of the order of the calculation and the shadowing parameterization used.

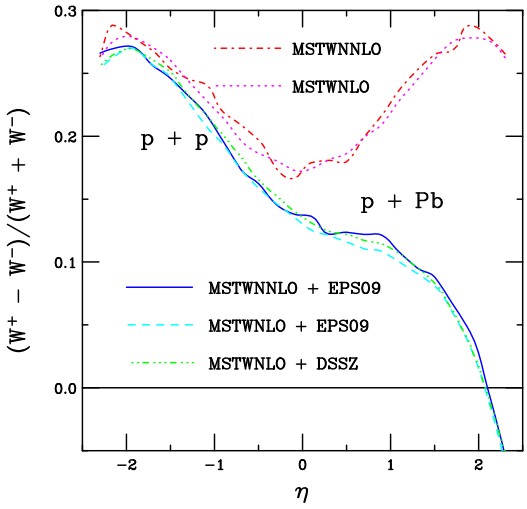

Fig. 42. The $W^{\pm}$ charge asymmetry, $(N_{W^+} - N_{W^-})/(N_{W^+} + N_{W^-})$, as a function of the charged lepton pseudorapidity in both $p + p$ and p+Pb collisions in the center-of-mass frame for both systems.

8.2. *Nuclear modification of the transverse momentum spectrum of Z^0 production (Z.-B. Kang and J.-W. Qiu)*

The Collins-Soper-Sterman formalism[187] is used to calculate Z^0 production over the full p_T range at the LHC,

$$\frac{d\sigma_{A+B\to Z^0+X}}{dy\, dp_T^2} = \frac{1}{(2\pi)^2}\int d^2b\, e^{i\vec{p}_T\cdot\vec{b}}\,\tilde{W}(b, M_Z, x_1, x_2) + Y(p_T, M_Z, x_1, x_2)\,. \quad (71)$$

The $\tilde{W}$ term gives the dominant contribution when $p_T \ll M_Z$ while the Y term is perturbatively calculable, see Ref.,[188] allowing a smooth transition from the resummed low p_T region to $p_T \sim M_Z$ where the fixed-order perturbative QCD calculations work well. In Eq. (71), $x_1 = e^y\, M_Z/\sqrt{s}$ and $x_2 = e^{-y}\, M_Z/\sqrt{s}$ while $\tilde{W}$ is

given by[188]

$$\tilde{W}(b, M_Z, x_1, x_2) = \begin{cases} \tilde{W}^{\rm P}(b, M_Z, x_1, x_2) & b \le b_{\rm max} \\ \tilde{W}^{\rm P}(b_{\rm max}, M_Z, x_1, x_2)\, \tilde{F}^{\rm NP}(b, M_Z, x_1, x_2; b_{\rm max}) & b > b_{\rm max} \end{cases} \quad (72)$$

where $b_{\rm max} \sim 1/(\text{few GeV})$ is a parameter that specifies the region in which $\tilde{W}^{\rm P}$ is perturbatively valid, and $\tilde{F}^{\rm NP}$ is a nonperturbative function determining the large b behavior of $\tilde{W}$ and is defined below. In Eq. (72), $\tilde{W}^{\rm P}(b, M_Z, x_1, x_2)$ includes all powers of large perturbative logarithms resummed from $\ln(1/b^2)$ to $\ln(M_Z^2)$[187]

$$\tilde{W}^{\rm P}(b, M_Z, x_1, x_2) = {\rm e}^{-S(b, M_Z)}\, \tilde{W}^{\rm P}(b, c/b, x_1, x_2)\,, \quad (73)$$

where c is a constant of order one,[187,188] and

$$S(b, M_Z) = \int_{c^2/b^2}^{M_Z^2} \frac{d\mu^2}{\mu^2} \left[\ln\left(\frac{M_Z^2}{\mu^2}\right) A(\alpha_s(\mu)) + B(\alpha_s(\mu)) \right], \quad (74)$$

with perturbatively-calculated coefficients $A(\alpha_s)$ and $B(\alpha_s)$ given in Ref.[188] and references therein. The perturbative factor in Eq. (73), $\tilde{W}^{\rm P}(b, c/b, x_1, x_2)$, has no large logarithms. It is expressed as

$$\tilde{W}^{\rm P}(b, c/b, x_1, x_2) = \sigma_0 \sum_{i=q,\bar{q}} f_{i/A}(x_1, \mu = c/b)\, f_{\bar{i}/B}(x_2, \mu = c/b) \quad (75)$$

where σ_0 is the leading order $q\overline{q} \to Z^0$ partonic cross section.[188] The functions $f_{i/A}$ and $f_{\bar{i}/B}$ are the modified parton distributions given by[187]

$$f_{i/A}(x_1, \mu) = \sum_a \int_{x_1}^1 \frac{d\xi}{\xi}\, C_{i/a}(x_1/\xi, \mu)\, \phi_{a/A}(\xi, \mu) \quad (76)$$

where $\sum_a$ is over $a = q, \bar{q}, g$, $\phi_{a/A}(\xi, \mu)$ are the normal proton or effective nuclear parton distribution functions (PDFs) and $C_{i/a} = \sum_{n=0} C_{i/a}^{(n)} (\alpha_s/\pi)^n$ are perturbatively calculable coefficient functions for finding a parton i from a parton a, given in Ref.[188]

The non-perturbative function $\tilde{F}^{\rm NP}$ in Eq. (72) has the form,

$$F^{\rm NP}(b, M_Z, x_1, x_2; b_{\rm max}) = \exp\left\{ -\ln\left(\frac{M_Z^2 b_{\rm max}^2}{c^2}\right) \left[g_1 \left((b^2)^\alpha - (b_{\rm max}^2)^\alpha \right) \right.\right.$$
$$\left.\left. +\ g_2 \left(b^2 - b_{\rm max}^2 \right) \right] - \bar{g}_2 \left(b^2 - b_{\rm max}^2 \right) \right\}. \quad (77)$$

where the explicit logarithmic dependence, $\ln(M_Z^2\, b_{\rm max}^2/c^2)$, was derived by solving the Collins-Soper equation.[187] The g_2 term is a result of adding a general power correction to the renormalization group equation while the $\bar{g}_2$ term represents the size of the intrinsic transverse momentum of active partons.[188]

The coefficients of the two terms proportional to b^2 in Eq. (77) can be combined,[189]

$$G_2 = \ln\left(\frac{M^2 b_{\rm max}^2}{c^2}\right) g_2 + \bar{g}_2\,, \quad (78)$$

to sum the dynamical and intrinsic power corrections. By requiring the first and second derivatives of $\tilde{W}$ to be continuous at $b = b_{\max}$, the parameters α and g_1 in Eq. (77) can be uniquely fixed, leaving only one parameter, G_2, sensitive to the power corrections and other nonperturbative effects. Taking $\bar{g}_2 = 0.25 \pm 0.05$ GeV^2 and $g_2 = 0.01 \pm 0.005$ GeV^2, $G_2^{pp} = 0.324$ GeV^2. Predictions employing Eq. (71) are consistent with all $p + \overline{p}$ and $p + p$ data from the Tevatron and the LHC.[188]

The EPS09 NLO parameterization[48] is used to account for the leading-twist nuclear effects on the parton densities in $p+A$ collisions. Following the method proposed in Ref.,[189] the nuclear-size-enhanced multiple scattering effects are accounted for by choosing $g_2 \to g_2 A^{1/3}$. Then for Z^0 production, $G_2^{p\mathrm{Pb}} = 0.689$ GeV^2.

In Fig. 43, the predictions for Z^0 production are shown. The cross section including resummation in Eq. (71) is evaluated employing the CTEQ6M parton densities at factorization scale $\mu = M_T/2 = 0.5\sqrt{M_Z^2 + p_T^2}$. The Y term is calculated at NLO in α_s.[188] The upper panel shows the Z^0 production cross section as a func-

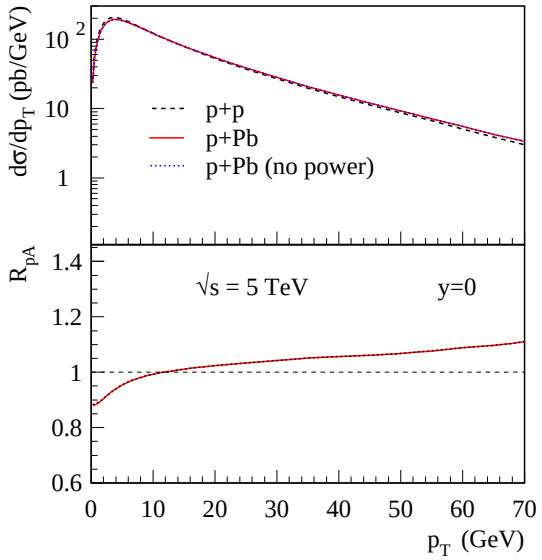

Fig. 43. Z^0 boson production in $p + p$ and p+Pb collisions at $\sqrt{s} = 5$ TeV and $y = 0$.[190]

tion of p_T. The black dashed curve is the $p + p$ baseline while the red solid curve shows the minimum bias p+Pb result. The blue dotted curve is the minimum bias p+Pb result without the $A^{1/3}$ enhancement of g_2 so that the nuclear-size-enhanced dynamical power corrections from multiple scattering are absent. The lower panel presents the nuclear modification factor R_{pA}.

In Fig. 43, the red solid curves are almost indistinguishable from the dotted curves. Thus, power corrections are not important for Z^0 production at LHC energies. Therefore, Z^0 production in $p+A$ collisions is an ideal probe of the modification

of the parton densities in nuclei as well as of the high energy "isospin" effect.

The Z^0 cross section at $y = 0$ is dominated by gluon-initiated subprocesses for $p_T > 20$ GeV/c. That is, R_{pA} is an excellent observable to study nuclear modifications of the gluon distribution, heretofore effectively unknown, especially at the values of x and μ probed by Z^0 production. At factorization scale $\mu = M_Z$, the EPS09 gluon shadowing factor[48] is less than unity (shadowing) for $x < 0.005$ and greater than unity (antishadowing) over a sufficiently large range, $0.005 < x < 0.2$, as shown in Fig. 44.

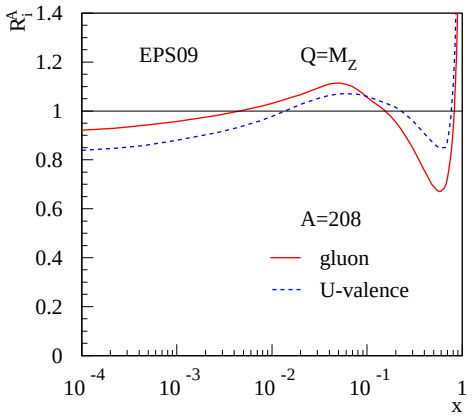

Fig. 44. The EPS09 shadowing ratio at scale $Q = M_Z$: $R_i^A = f_{i/A}(x, Q^2)/f_{i/p}(x, Q^2)$. The red solid curve shows the gluon ratio while the blue dashed curve shows the valence u-quark ratio.

As indicated in the lower half of Fig. 43, the nuclear modification factor R_{pA} for Z^0 production is suppressed at $p_T < 10$ GeV/c and enhanced at high p_T, up to $p_T \sim 70$ GeV/c. The low p_T suppression is a result of low x shadowing in EPS09. However, the strong enhancement over such a large p_T range was unexpected. After a careful examination of the kinematics, it was found that, at $y = 0$, $x \sim M_T/\sqrt{s} \sim 0.013$, already in the EPS09 antishadowing region. Thus, the clear enhancement of R_{pA} in the large p_T region in Fig. 43 can be explained by the broad EPS09 antishadowing region at the Z^0 scale. The large p_T enhancement of R_{pA} vanishes for other shadowing parameterizations with smaller gluon antishadowing. Therefore, the measurement of R_{pA} for Z^0 production in p+Pb collisions at the LHC provides a clean and unique test of gluon antishadowing as proposed in the EPS09 parameterization. Furthermore, R_{pA} is a direct measurement of nuclear gluon distribution since the cross section is dominated by gluon-initiated subprocesses for $p_T > 20$ GeV/c.

8.3. *Transverse momentum broadening of vector boson production (Z.-B. Kang and J.-W. Qiu)*

Finally, transverse momentum broadening of inclusive vector boson production, $A(p_1) + B(p_2) \to V[\mathrm{J}/\psi, \Upsilon, Z^0](q) + X$ at the LHC is discussed. The average squared transverse momentum of vector boson production is

$$\langle q_T^2 \rangle(y)_{AB} \equiv \int dq_T^2 \, q_T^2 \, \frac{d\sigma_{AB\to V}}{dy \, dq_T^2} \left[\int dq_T^2 \, \frac{d\sigma_{AB\to V}}{dy \, dq_T^2} \right]^{-1} . \tag{79}$$

The transverse momentum broadening in p+Pb collisions is defined as

$$\Delta\langle q_T^2 \rangle_{p\,\mathrm{Pb}}(y) \equiv \langle q_T^2 \rangle(y)_{p\,\mathrm{Pb}} - \langle q_T^2 \rangle(y)_{pp} \, . \tag{80}$$

Following the derivation in Refs.,[130,183] the first nonvanishing contribution to the transverse momentum broadening of heavy quarkonium production is

$$\Delta\langle q_T^2 \rangle_{\mathrm{HQ}}^{\mathrm{CEM}} = \left(\frac{8\pi^2 \alpha_s}{N_c^2 - 1} \, \lambda^2 \, A^{1/3} \right) \frac{(C_F + C_A) \, \sigma_{q\bar{q}} + 2 \, C_A \, \sigma_{gg} + \Delta\sigma_{gg}}{\sigma_{q\bar{q}} + \sigma_{gg}} \tag{81}$$

where the superscript "CEM" indicates that heavy quarkonium production is evaluated in the Color Evaporation Model (CEM). A similar result was derived in the NRQCD approach.[183] The $\sigma_{q\bar{q}}$ and σ_{gg} partonic cross sections are contributions from quark-antiquark and gluon-gluon subprocesses, respectively.[183] The $\Delta\sigma_{gg}$ term is a small, color-suppressed correction to the gg subprocess derived in Ref.[130] In the region where the gg subprocess dominates heavy quarkonium production, $\sigma_{gg} \gg \sigma_{q\bar{q}}$, $\Delta\sigma_{gg}$, heavy quarkonium broadening is further simplified as[183]

$$\Delta\langle q_T^2 \rangle_{\mathrm{HQ}}^{\mathrm{CEM}} \approx 2 \, C_A \left(\frac{8\pi^2 \alpha_s}{N_c^2 - 1} \, \lambda^2 \, A^{1/3} \right) . \tag{82}$$

In Fig. 45, the predictions of transverse momentum broadening of Drell-Yan type vector boson production in p+Pb collisions at the LHC at $y = 0$ are shown as a function of N_{coll}. To determine the effective dependence on N_{coll}, the $A^{1/3}$ in Eq. (81) is replaced by $A^{1/3} N_{\mathrm{coll}}(b)/N_{\mathrm{coll}}(b_{\mathrm{min\,bias}})$. In p+Pb collisions at the LHC, a Glauber-model calculation with $\sigma_{\mathrm{NN}}^{\mathrm{in}} = 70$ mb at $\sqrt{s} = 5$ TeV gives $N_{\mathrm{coll}}(b_{\mathrm{min\,bias}}) \sim 7$. In addition to heavy quarkonium production, the broadening of W/Z^0 production, calculated using the formalism derived in Ref.,[183] is also shown in Fig. 45. The dramatic difference in the magnitude of the broadening between heavy quarkonium and W/Z^0 production in Fig. 45 should be a signature QCD prediction.

9. Acknowledgments

The research of J. L. Albacete is supported by a fellowship from the Théorie LHC France initiative funded by the IN2P3. The work of N. Armesto was supported by the European Research Council grant HotLHC ERC-2001-StG-279579; by Ministerio de Ciencia e Innovación of Spain grants FPA2008-01177, FPA2009-06867-E and Consolider-Ingenio 2010 CPAN CSD2007-00042; by Xunta de Galicia grant

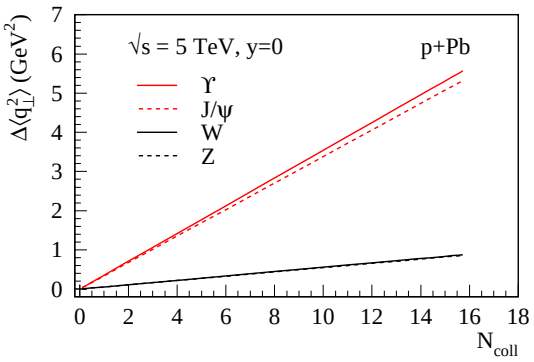

Fig. 45. The transverse momentum broadening of vector boson production in p+Pb collisions at $y = 0$, shown as a function of $N_{\rm coll}$. The Υ (red solid), J/ψ (red dashed), $W^{\pm}$ (black solid), and Z^0 (black dashed) results are given.[190]

PGIDIT10PXIB 206017PR; and by FEDER. G. G. Barnaföldi was partially supported by the János Bolyai Research Scholarship of the Hungarian Academy of Sciences. G. G. Barnaföldi, M. Gyulassy, and P. Levai also acknowledge Hungarian grants OTKA PD73596, NK77816, NK106119, NIH TET_10-1_2011-0061 and ZA-15/2009. J. Barrette and V. Topor Pop are supported by the Natural Sciences and Engineering Research Council of Canada. S. De is grateful to the Department of Atomic Energy of India for financial support. A. Dumitru is supported by the DOE Office of Nuclear Physics through Grant No. DE-FG02-09ER41620 and by The City University of New York through the PSC-CUNY Research Award Program, grant 65041-0043. K. Dusling is supported by the US Department of Energy under DOE Contract No. DE-FG02-03ER41260. K. J. Eskola is supported by the Academy of Finland, Project 133005. R. J. Fries would like to acknowledge support by NSF CAREER Award PHY-0847538 and by the JET Collaboration and DOE grant DE-FG02-10ER41682. H. Fujii and Y. Nara are supported in part by Grant-in-Aid for Scientific Research (B) 22340064. F. Gelis is supported by the Agence Nationale de la Recherche project 11-BS04-015-01. M. Gyulassy is supported by the Division of Nuclear Science, U.S. Department of Energy, under Contract No. DE-AC03-76SF00098 and DE-FG02-93ER-40764 (associated with the JET Topical Collaboration Project). I. Helenius is supported by the Magnus Ehrnrooth Foundation. The work of B. Z. Kopeliovich was partially supported by Fondecyt (Chile) grant No. 1090291. The work of K. Kutak and S. Sapeta was partially supported by the Foundation for Polish Science with the grant Homing Plus/2010-2/6. The work of A. H. Mueller is supported in part by the US Department of Energy under contract No. DE-FG02-92ER-40699. The work of J. Nemchik was supported by grants VZ MŠMT 6840770039 and LA 08015 (Ministry of Education of the Czech Republic). M. Petrovici is supported by the Romanian Authority for Scientific Research, CNCS-UEFIS-CDI project number PN-II-ID-2011-3-0368. The work

of A. H. Rezaeian was partially supported by Fondecyt (Chile) grant No. 1110781. R. Venugopalan was supported by US Department of Energy under DOE Contract No. DE-AC02-98CH10886. The work of R. Vogt was performed under the auspices of the U.S. Department of Energy by Lawrence Livermore National Laboratory under Contract DE-AC52-07NA27344 and within the framework of the JET Collaboration. The work of X.-N. Wang was performed under the auspices of the U.S. Department of Energy under Contract No. DE-AC02-05CH11231, by the National Natural Science Foundation of China under grant No. 11221504, and within the framework of the JET Collaboration. I. Vitev is supported by the US Department of Energy, Office of Science, under Contract No. DE-AC52-06NA25396 and by the LDRD program at LANL.

References

1. http://jet.lbl.gov/
2. B. Abelev *et al.* [ALICE Collaboration], arXiv:1210.3615 [nucl-ex].
3. B. Abelev *et al.* [ALICE Collaboration], arXiv:1210.4520 [nucl-ex].
4. Y. V. Kovchegov and K. Tuchin, *Phys. Rev. D* **65** (2002) 074026.
5. J. Jalilian-Marian, A. Kovner, A. Leonidov and H. Weigert, *Nucl. Phys.* B **504** (1997) 415.
6. J. Jalilian-Marian, A. Kovner, A. Leonidov and H. Weigert, *Phys. Rev. D* **59** (1999) 014014.
7. E. Iancu, A. Leonidov and L. D. McLerran, *Nucl. Phys. A* **692** (2001) 583.
8. E. Ferreiro, E. Iancu, A. Leonidov and L. D. McLerran, *Nucl. Phys.* A **703** (2002) 489.
9. A. Dumitru, A. Hayashigaki and J. Jalilian-Marian, *Nucl. Phys.* A **765** (2006) 464.
10. T. Altinoluk and A. Kovner, *Phys. Rev.* D **83** (2011) 105004.
11. I. Balitsky, *Nucl. Phys.* B **463** (1996) 99.
12. Y. V. Kovchegov, *Phys. Rev. D* **60** (1999) 034008.
13. Y. V. Kovchegov, *Phys. Rev. D* **61** (2000) 074018.
14. I. Balitsky, *Phys. Rev. D* **75** (2007) 014001.
15. J. L. Albacete, N. Armesto, J.G. Milhano, P. Quiroga Arias and C. A. Salgado, *Eur. Phys. J. C* **71** (2011) 1705.
16. J. L. Albacete and Y. V. Kovchegov, *Phys. Rev.* D **75** (2007) 125021.
17. L. D. McLerran and R. Venugopalan, *Phys. Rev. D* **49** (1994) 2233.
18. L. D. McLerran and R. Venugopalan, *Phys. Rev. D* **49** (1994) 3352.
19. L. D. McLerran and R. Venugopalan, *Phys. Rev. D* **50** (1994) 2225.
20. A. H. Rezaeian, *Phys. Lett.* B **718** (2013) 1058.
21. H. Kowalski and D. Teaney, *Phys. Rev. D* **68** (2003) 114005.
22. K. J. Golec-Biernat and M. Wusthoff, *Phys. Rev. D* **59** (1998) 014017.
23. K. J. Golec-Biernat and M. Wusthoff, *Phys. Rev. D* **60** (1999) 114023.
24. J. Bartels, K. J. Golec-Biernat and H. Kowalski, *Phys. Rev. D* **66** (2002) 014001.
25. L. D. McLerran and R. Venugopalan, *Phys. Rev. D* **59** (1999) 094002.
26. R. Venugopalan, *Acta Phys. Polon. B* **30** (1999) 3731.
27. G. Watt and H. Kowalski, *Phys. Rev. D* **78** (2008) 014016.
28. S. Chekanov *et al.* [ZEUS Collaboration], *Eur. Phys. J. C* **21** (2001) 443.
29. C. Adloff *et al.* [H1 Collaboration], *Eur. Phys. J. C* **21** (2001) 33.
30. S. Chekanov *et al.* [ZEUS Collaboration], *Eur. Phys. J. C* **24** (2002) 345.
31. A. Aktas *et al.* [H1 Collaboration], *Eur. Phys. J. C* **46** (2006) 585.

32. H. Kowalski, L. Motyka and G. Watt, *Phys. Rev. D* **74** (2006) 074016.
33. A. H. Rezaeian, M. Siddikov, M. Van de Klundert and R. Venugopalan, arXiv:1212.2974 [hep-ph].
34. P. Tribedy and R. Venugopalan, *Nucl. Phys. A* **850** (2011) 136; [Erratum-ibid. A **859** (2011) 185].
35. P. Tribedy and R. Venugopalan, *Phys. Lett. B* **710** (2012) 125; [Erratum-ibid. B **718** (2013) 1154].
36. B. Schenke, P. Tribedy and R. Venugopalan, *Phys. Rev. Lett.* **108** (2012) 252301.
37. B. Schenke, P. Tribedy and R. Venugopalan, *Phys. Rev. C* **86** (2012) 034908.
38. H. Kowalski, T. Lappi and R. Venugopalan, *Phys. Rev. Lett.* **100** (2008) 022303.
39. J. P. Blaizot, F. Gelis and R. Venugopalan, *Nucl. Phys. A* **743** (2004) 57.
40. M. A. Braun, *Phys. Lett. B* **483** (2000) 105.
41. F. Gelis, A. M. Stasto and R. Venugopalan, *Eur. Phys. J. C* **48** (2006) 489.
42. B. A. Kniehl, G. Kramer and B. Potter, *Nucl. Phys.* B **582** (2000) 514.
43. X. -N. Wang and M. Gyulassy, *Phys. Rev. D* **44** (1991) 3501.
44. M. Gyulassy and X. -N. Wang, *Comput. Phys. Commun.* **83** (1994) 307 [arXiv:nucl-th/9502021].
45. W. -T. Deng, X. -N. Wang and R. Xu, *Phys. Rev. C* **83** (2011) 014915.
46. W. -T. Deng, X. -N. Wang and R. Xu, *Phys. Lett.* B **701** (2011) 133.
47. S. -y. Li and X. -N. Wang, *Phys. Lett.* B **527** (2002) 85.
48. K. J. Eskola, H. Paukkunen and C. A. Salgado, *JHEP* **0904** (2009) 065.
49. J. W. Cronin, H. J. Frisch, M. J. Shochet, J. P. Boymond, R. Mermod, P. A. Piroue and R. L. Sumner, *Phys. Rev. D* **11** (1975) 3105.
50. R. Xu, W. -T. Deng and X. -N. Wang, arXiv:1204.1998 [nucl-th].
51. B. Andersson, G. Gustafson, G. Ingelman and T. Sjostrand, *Phys. Rept.* **97** (1983) 31.
52. X. -N. Wang and M. Gyulassy, *Phys. Rev. Lett.* **68** (1992) 1480.
53. V. Topor Pop, M. Gyulassy, J. Barrette, and C. Gale, *Phys. Rev. C* **84** (2011) 022002.
54. V. Topor Pop, M. Gyulassy, J. Barrette, C. Gale, and A. Warburton, *Phys. Rev. C* **83** (2011) 024902.
55. G. G. Barnafoldi, J. Barrette, M. Gyulassy, P. Levai and V. Topor Pop, *Phys. Rev. C* **85** (2012) 024903.
56. V. Topor Pop, M. Gyulassy, J. Barrette, C. Gale and A. Warburton, arXiv:1203.6679 v2 [hep-ph].
57. B. Andersson, G. Gustafson, and B. Nilsson-Almqvist, *Nucl. Phys. B* **281** (1987) 289.
58. B. Nilsson-Almqvist and E. Stenlund, *Comput. Phys. Commun.* **43** (1987) 387.
59. H. -U. Bengtsson and T. Sjostrand, *Comput. Phys. Commun.* **46** (1987) 43.
60. P. Levai, D. Berenyi, A. Pasztor, and V. V. Skokov, *J. Phys. G* **38** (2011) 124155.
61. D. W. Duke and J. F. Owens, *Phys. Rev. D* **30** (1984) 49.
62. M. Gluck, E. Reya, and A. Vogt, *Z. Phys. C* **67** (1995) 433.
63. G. Altarelli and G. Parisi, *Nucl. Phys. B* **126** (1977) 298.
64. Recent and test versions of the AMPT codes are available at http://personal.ecu.edu/linz/ampt
65. Z. -W. Lin, C. M. Ko, B. -A. Li, B. Zhang and S. Pal, *Phys. Rev. C* **72** (2005) 064901.
66. J. Xu and C. M. Ko, *Phys. Rev. C* **83** (2011) 034904.
67. Z. -B. Kang, I. Vitev and H. Xing, *Phys. Lett. B* **718** (2012) 482.
68. J. F. Owens, *Rev. Mod. Phys.* **59** (1987) 465.
69. J. Pumplin, D. R. Stump, J. Huston, H. L. Lai, P. M. Nadolsky and W. K. Tung,

JHEP **0207** (2002) 012.
70. D. de Florian, R. Sassot and M. Stratmann, *Phys. Rev. D* **75** (2007) 114010.
71. I. Vitev, J. T. Goldman, M. B. Johnson and J. W. Qiu, *Phys. Rev. D* **74** (2006) 054010.
72. Z. -B. Kang, J. -W. Qiu and W. Vogelsang, *Phys. Rev. D* **79** (2009) 054007.
73. A. Accardi, arXiv:hep-ph/0212148.
74. J. -w. Qiu and I. Vitev, *Phys. Lett.* B **570** (2003) 161.
75. G. Ovanesyan and I. Vitev, *JHEP* **1106** (2011) 080.
76. R. B. Neufeld, I. Vitev and B. -W. Zhang, *Phys. Lett.* B **704** (2011) 590.
77. I. Vitev, *Phys. Rev. C* **75** (2007) 064906.
78. J. -w. Qiu and I. Vitev, *Phys. Lett. B* **632** (2006) 507.
79. J. -W. Qiu and I. Vitev, *Phys. Lett.* B **587** (2004) 52.
80. Z. -B. Kang, I. Vitev and H. Xing, *Phys. Rev. D* **85** (2012) 054024.
81. Y. Zhang, G. I. Fai, G. Papp, G. G. Barnafoldi and P. Levai, *Phys. Rev. C* **65** (2002) 034903.
82. G. Papp, G. G. Barnafoldi, P. Levai, and G. Fai, arXiv:hep-ph/0212249.
83. D. Antreasyan *et al.* [Chicago-Princeton Collaboration], *Phys. Rev. D* **19** (1979) 764.
84. F. Aversa, P. Chiappetta, M. Greco, and J. Ph. Guillet, *Nucl. Phys.* B **327** (1989) 105.
85. P. Aurenche, M. Fontannaz, J. Ph. Guillet, B. Kniehl, E. Pilon, and M. Werlen, *Eur. Phys. J.* C **9** (1999) 107.
86. P. Aurenche, M. Fontannaz, J. Ph. Guillet, B. Kniehl, and M. Werlen, *Eur. Phys. J. C* **13** (2001) 347.
87. X. N. Wang, *Phys. Rev. C* **61** (2000) 064910.
88. C. Y. Wong and H. Wang, *Phys. Rev. C* **58** (1998) 376.
89. G. G. Barnafoldi, P. Levai, G. Papp, G. I. Fai and Y. Zhang, *Heavy Ion Phys.* **18** (2003) 79 [arXiv:nucl-th/0206006].
90. G. G. Barnafoldi, P. Levai, G. Papp, G. I. Fai and Y. Zhang, arXiv:nucl-th/0212111.
91. A. D. Martin, R. G. Roberts, W. J. Stirling, and R. S. Thorne, *Eur. Phys. J. C* **23** (2002) 73.
92. K. J. Eskola, V. J. Kolhinen and C. A. Salgado, *Eur. Phys. J. C* **9**, 61 (1999).
93. K. J. Eskola, H. Paukkunen, and C. A. Salgado, *JHEP* **0807** (2008) 102.
94. M. Hirai, S. Kumano and M. Miyama, *Phys. Rev. D* **64** (2001) 034003.
95. J. L. Albacete, A. Dumitru, H. Fujii and Y. Nara, arXiv:1209.2001 [hep-ph] (submitted to *Nucl. Phys. A*).
96. A. H. Rezaeian, *Phys. Rev. D* **85** (2012) 014028.
97. J. Jalilian-Marian and A. H. Rezaeian, *Phys. Rev. D* **85** (2012) 014017.
98. E. Levin and A. H. Rezaeian, *Phys. Rev. D* **82** (2010) 014022.
99. E. Levin and A. H. Rezaeian, *Phys. Rev. D* **83** (2011) 114001.
100. E. Levin and A. H. Rezaeian, *AIP Conf. Proc.* **1350** (2011) 243 [arXiv:1011.3591 [hep-ph]].
101. A. H. Rezaeian, arXiv:1110.6642 [hep-ph].
102. E. Levin and A. H. Rezaeian, *Phys. Rev. D* **82** (2010) 054003.
103. A. H. Rezaeian, arXiv:1208.0026 [hep-ph].
104. J. W. Harris [ALICE Collaboration], *AIP Conf. Proc.* **1422** (2012) 15 [arXiv:1111.4651 [nucl-ex]].
105. B. Z. Kopeliovich, J. Nemchik, A. Schäfer and A. V. Tarasov, *Phys. Rev. Lett.* **88** (2002) 232303.
106. B. Z. Kopeliovich, A. Schäfer and A. V. Tarasov, *Phys. Rev. D* **62** (2000) 054022.
107. B. A. Cole, G. G. Barnafoldi, P. Levai, G. Papp and G. Fai, arXiv:hep-ph/0702101.

108. A. Adeluyi, G. G. Barnafoldi, G. Fai and P. Levai, *Phys. Rev. C* **80** (2009) 014903.
109. D. Kharzeev, Y. V. Kovchegov, and K. Tuchin, *Phys. Rev. D* **68** (2003) 094013.
110. P. Levai, *Nucl. Phys. A* **862-863** (2011) 146.
111. G. G. Barnafoldi, G. Fai, P. Levai, B. A. Cole and G. Papp, *Indian J. Phys.* **84** (2010) 1721.
112. D. d'Enterria, arXiv:nucl-ex/0302016.
113. A. D. Martin, W. J. Stirling, R. S. Thorne and G. Watt, *Phys. Lett.* B **652** (2007) 292.
114. A. D. Martin, W. J. Stirling, R. S. Thorne and G. Watt, *Eur. Phys. J.* C **63** (2009) 189.
115. J. L. Albacete and A. Dumitru, arXiv:1011.5161.
116. P. Quiroga-Arias, J. G. Milhano and U. A. Wiedemann, *Phys. Rev. C* **82** (2010) 034903.
117. F. Arleo, K. J. Eskola, H. Paukkunen and C. A. Salgado, *JHEP* **1104** (2011) 055.
118. S. J. Brodsky, J. F. Gunion, and J. H. Kuhn, *Phys. Rev. Lett.* **39** (1977) 1120.
119. A. Adil and M. Gyulassy, *Phys. Rev.* C **72** (2005) 034907.
120. I. Helenius, K. J. Eskola, H. Honkanen and C. A. Salgado, *JHEP* **1207** (2012) 073.
121. S. Albino, B. A. Kniehl and G. Kramer, *Nucl. Phys.* B **803** (2008) 42.
122. C. Lourenço, R. Vogt and H. Wöhri, *JHEP* **0902** (2009) 014.
123. D. C. McGlinchey, A. D. Frawley and R. Vogt, arXiv:1208.2667 [nucl-th].
124. R. E. Nelson, R. Vogt and A. D. Frawley, *Phys. Rev. C*, in press [arXiv:1210:4610 [hep-ph]].
125. R. Vogt, *Phys. Rev. C* **81** (2010) 044903.
126. P. M. Nadolsky, H. -L. Lai, Q. -H. Cao, J. Huston, J. Pumplin, D. Stump, W. K. Tung and C. -P. Yuan, *Phys. Rev. D* **78** (2008) 013004.
127. S. Catani, M. Fontannaz, J. P. Guillet and E. Pilon, *JHEP* **0205** (2002) 028.
128. P. Aurenche, M. Fontannaz, J. -P. Guillet, E. Pilon and M. Werlen, *Phys. Rev. D* **73** (2006) 094007.
129. L. Bourhis, M. Fontannaz and J. P. Guillet, *Eur. Phys. J. C* **2** (1998) 529.
130. H. Xing, Z. -B. Kang, I. Vitev and E. Wang, *Phys. Rev. D* **86** (2012) 094010.
131. M. Gluck, E. Reya and A. Vogt, *Phys. Rev. D* **48** (1993) 116, [Erratum-ibid D **51** (1995) 1427].
132. F. Gelis and J. Jalilian-Marian, *Phys. Rev. D* **66** (2002) 014021.
133. R. Baier, A. H. Mueller and D. Schiff, *Nucl. Phys. A* **741** (2004) 358.
134. J. Jalilian-Marian and A. H. Rezaeian, *Phys. Rev. D* **86** (2012) 034016.
135. A. H. Rezaeian and A. Schaefer, *Phys. Rev. D* **81** (2010) 114032.
136. E. Iancu, K. Itakura and S. Munier, *Phys. Lett.* B **590** (2004) 199.
137. A. H. Rezaeian, *Phys. Rev. D* **86** (2012) 094016.
138. F. Gelis, E. Iancu, J. Jalilian-Marian and R. Venugopalan, *Ann. Rev. Part. Nucl Sci.* **60** (2010) 463.
139. D. N. Triantafyllopoulos, arXiv:1209.3183 [hep-ph].
140. A. H. Mueller and D. N. Triantafyllopoulos, *Nucl. Phys. B* **640** (2002) 331.
141. G. Aad *et al.* [ATLAS Collaboration], *Phys. Rev. Lett.* **105** (2010) 252303.
142. G. Aad *et al.* [ATLAS Collaboration], arXiv:1208.1967 [hep-ex].
143. S. Chatrchyan *et al.* [CMS Collaboration], *Phys. Rev. C* **84** (2011) 024906.
144. S. Chatrchyan *et al.* [CMS Collaboration], *Phys. Lett. B* **712** (2012) 176.
145. S. Chatrchyan *et al.* [CMS Collaboration], arXiv:1205.0206 [nucl-ex].
146. S. Chatrchyan *et al.* [CMS Collaboration], arXiv:1205.5872 [nucl-ex].
147. S. Frixione, Z. Kunszt and A. Signer, *Nucl. Phys. B* **467** (1996) 399.
148. S. Frixione, *Nucl. Phys. B* **507** (1997) 295.

149. S. Frixione and G. Ridolfi, *Nucl. Phys. B* **507** (1997) 315.
150. K. J. Eskola, V. J. Kolhinen and P. V. Ruuskanen, *Nucl. Phys. B* **535** (1998) 351.
151. M. Cacciari, G. P. Salam and G. Soyez, *JHEP* **0804** (2008) 063.
152. A. Accardi *et al.*, arXiv:hep-ph/0308248.
153. A. Accardi *et al.*, arXiv:hep-ph/0310274.
154. M. Lamont at the *111th LHCC Meeting* (CERN, September 26-27 2012) [`http://indico.cern.ch/conferenceDisplay.py?confId=207964`].
155. M. Cacciari and G. P. Salam, *Phys. Lett. B* **659** (2008) 119.
156. Z. Kunszt and D. E. Soper, *Phys. Rev. D* **46** (1992) 192.
157. S. D. Ellis, Z. Kunszt and D. E. Soper, *Phys. Rev. Lett.* **64** (1990) 2121.
158. S. D. Ellis, Z. Kunszt and D. E. Soper, *Phys. Rev. Lett.* **69** (1992) 1496.
159. I. Vitev and B.-W. Zhang, *Phys. Rev. Lett.* **104** (2010) 132001.
160. Y. He, I. Vitev and B.-W. Zhang, *Phys. Lett. B* **713** (2012) 224.
161. Y. He, B.-W. Zhang and E. Wang, *Eur. Phys. J. C* **72** (2012) 1904.
162. D. de Florian, R. Sassot, M. Stratmann and P. Zurita, arXiv:1204.3797 [hep-ph].
163. D. de Florian, R. Sassot, P. Zurita and M. Stratmann, *Phys. Rev. D* **85** (2012) 074028.
164. M. Hirai, S. Kumano and T. -H. Nagai, *Phys. Rev. C* **76** (2007) 065207.
165. G. Aad *et al.* [ATLAS Collaboration], *Eur. Phys. J. C* **71** (2011) 1512.
166. S. D. Ellis and D. E. Soper, *Phys. Rev. Lett.* **74** (1995) 5182.
167. Y. He, B.-W. Zhang and E. Wang, in preparation.
168. L. V. Gribov, E. M. Levin and M. G. Ryskin, *Phys. Rept.* **100** (1983) 1.
169. K. Kutak and S. Sapeta, arXiv:1205.5035 [hep-ph].
170. M. Deak, F. Hautmann, H. Jung and K. Kutak, arXiv:1012.6037 [hep-ph].
171. J. L. Albacete and C. Marquet, *Phys. Rev. Lett.* **105** (2010) 162301.
172. A. Dumitru, K. Dusling, F. Gelis, J. Jalilian-Marian, T. Lappi and R. Venugopalan, *Phys. Lett. B* **697** (2011) 21.
173. S. Catani, M. Ciafaloni, F. Hautmann, *Nucl. Phys. B* **366** (1991) 1.
174. C. Marquet and R. B. Peschanski, *Phys. Lett. B* **587** (2004) 201.
175. M. Deak, F. Hautmann, H. Jung and K. Kutak, *JHEP* **0909** (2009) 121.
176. K. Kutak and J. Kwiecinski, *Eur. Phys. J. C* **29** (2003) 521.
177. K. Kutak and A. M. Stasto, *Eur. Phys. J. C* **41** (2005) 343.
178. V. Khachatryan *et al.* [CMS Collaboration], *JHEP* **1009** (2010) 091.
179. K. Dusling and R. Venugopalan, *Phys. Rev. Lett.* **108** (2012) 262001.
180. K. Dusling and R. Venugopalan, arXiv:1210.3890 [hep-ph].
181. S. Chatrchyan *et al.* [CMS Collaboration], *Phys. Lett. B* **718** (2013) 795.
182. K. Dusling and R. Venugopalan, arXiv:1211.3701 [hep-ph].
183. Z. -B. Kang and J. -W. Qiu, *Phys. Rev. D* **77** (2008) 114027 (2008).
184. G. Aad *et al.* [ATLAS Collaboration], *Phys. Lett. B* **705** (2011) 415.
185. G. Aad *et al*, [ATLAS Collaboration], *Phys. Rev. D* **85** (2012) 012005.
186. S. Catani, L. Cieri, G. Ferrera, D. de Florian, and M. Grazzini, *Phys. Rev. Lett.* **103** (2009) 082001.
187. J. C. Collins, D. E. Soper and G. Sterman, *Nucl. Phys. B* **250** (1985) 199.
188. J. -W. Qiu and X. -f. Zhang, *Phys. Rev. D* **63** (2001) 114011.
189. X. -f. Zhang and G. I. Fai, *Phys. Lett. B* **545** (2002) 91.
190. Z.-B. Kang and J.-W. Qiu, arXiv:1212.6541 [hep-ph].